



# **NAVAL POSTGRADUATE SCHOOL**

**MONTEREY, CALIFORNIA**

## **THESIS**

**A FURTHER EXAMINATION OF POTENTIAL  
OBSERVATION NETWORK DESIGN WITH MESOSCALE  
ENSEMBLE SENSITIVITIES IN COMPLEX TERRAIN**

by

Sean M. Wile

March 2013

Thesis Advisor:  
Second Reader:

Joshua P. Hacker  
James D. Doyle

**Approved for public release; distribution is unlimited**

THIS PAGE INTENTIONALLY LEFT BLANK

| REPORT DOCUMENTATION PAGE   |  |   | Form Approved OMB No. 0704-0188                |   |
|---|--|---|--|---|
| Public reporting burden for this collection of information is estimated to average 1 hour per response, including the time for reviewing instruction, searching existing data sources, gathering and maintaining the data needed, and completing and reviewing the collection of information. Send comments regarding this burden estimate or any other aspect of this collection of information, including suggestions for reducing this burden, to Washington headquarters Services, Directorate for Information Operations and Reports, 1215 Jefferson Davis Highway, Suite 1204, Arlington, VA 22202-4302, and to the Office of Management and Budget, Paperwork Reduction Project (0704-0188) Washington DC 20503.   |  |   |  |   |
| 1. AGENCY USE ONLY (Leave blank)  |  | 2. REPORT DATE<br>March 2013                            |  | 3. REPORT TYPE AND DATES COVERED<br>Master's Thesis |
| 4. TITLE AND SUBTITLE<br>A FURTHER EXAMINATION OF POTENTIAL OBSERVATION NETWORK DESIGN WITH MESOSCALE ENSEMBLE SENSITIVITIES IN COMPLEX TERRAIN   |  |   | 5. FUNDING NUMBERS                             |   |
| 6. AUTHOR(S) Sean M. Wile   |  |   |  |   |
| 7. PERFORMING ORGANIZATION NAME(S) AND ADDRESS(ES)<br>Naval Postgraduate School<br>Monterey, CA 93943-5000  |  |   | 8. PERFORMING ORGANIZATION REPORT NUMBER       |   |
| 9. SPONSORING /MONITORING AGENCY NAME(S) AND ADDRESS(ES)<br>N/A   |  |   | 10. SPONSORING/MONITORING AGENCY REPORT NUMBER |   |
| 11. SUPPLEMENTARY NOTES The views expressed in this thesis are those of the author and do not reflect the official policy or position of the United States Air Force, Department of Defense or the U.S. Government. IRB Protocol number N/A.  |  |   |  |   |
| 12a. DISTRIBUTION / AVAILABILITY STATEMENT<br>Approved for public release; distribution is unlimited  |  |   | 12b. DISTRIBUTION CODE                         |   |
| 13. ABSTRACT (maximum 200 words)<br>Recent expansion in availability of stand-alone atmospheric observing sensors introduces the question of where placement maximizes gain in forecast accuracy. This study examined how sensitivity analysis and observation targeting can be used to optimize sensor placement. The primary objective of this project was to determine whether a mesoscale Ensemble Sensitivity Analysis (ESA) can be used to identify the sensitivity profile of fog formation in a complex terrain environment. Building on work by Chilcoat (2012), this study utilized several alternate methodologies to conduct ESA, including a more realistic observing network and implementation of a Gaussian filter. The second objective was to determine whether the calculated sensitivities could be used to reduce forecast uncertainty for a forecast metric related to dense fog formation. This was done by introducing a real-world "truth" observation at the location of greatest sensitivity. The results of this study indicate that ESA provides a cogent mesoscale sensitivity profile which can be used to accurately predict forecast changes in fog using initial condition potential temperature values. This type of information may prove valuable in planning the layout of future observational networks, as well as introduce the potential for performing data-thinning during data assimilation and real-time updates to forecast metrics. |  |   |  |   |
| 14. SUBJECT TERMS Mesoscale Ensemble Sensitivity Analysis, Ensemble Sensitivities, Mesoscale Forecast Sensitivities, Observation Network Design, ESA  |  |   | 15. NUMBER OF PAGES<br>123                     |   |
|   |  |   | 16. PRICE CODE                                 |   |
| 17. SECURITY CLASSIFICATION OF REPORT<br>Unclassified   | 18. SECURITY CLASSIFICATION OF THIS PAGE<br>Unclassified | 19. SECURITY CLASSIFICATION OF ABSTRACT<br>Unclassified | 20. LIMITATION OF ABSTRACT<br>UU               |   |

THIS PAGE INTENTIONALLY LEFT BLANK

Approved for public release; distribution is unlimited

**A FURTHER EXAMINATION OF POTENTIAL OBSERVATION NETWORK  
DESIGN WITH MESOSCALE ENSEMBLE SENSITIVITIES IN COMPLEX  
TERRAIN**

Sean M. Wile  
Captain, United States Air Force  
B.S., Florida State University, 2003

Submitted in partial fulfillment of the  
requirements for the degree of

**MASTER OF SCIENCE IN METEOROLOGY**

from the

**NAVAL POSTGRADUATE SCHOOL  
March 2013**

Author: Sean M. Wile

Approved by: Joshua P. Hacker  
Thesis Advisor

James D. Doyle  
Second Reader

Wendell Nuss  
Chair, Department of Meteorology

THIS PAGE INTENTIONALLY LEFT BLANK

## **ABSTRACT**

Recent expansion in availability of stand-alone atmospheric observing sensors introduces the question of where placement maximizes gain in forecast accuracy. This study examined how sensitivity analysis and observation targeting can be used to optimize sensor placement. The primary objective of this project was to determine whether a mesoscale Ensemble Sensitivity Analysis (ESA) can be used to identify the sensitivity profile of fog formation in a complex terrain environment. Building on work by Chilcoat (2012), this study utilized several alternate methodologies to conduct ESA, including a more realistic observing network and implementation of a Gaussian filter. The second objective was to determine whether the calculated sensitivities could be used to reduce forecast uncertainty for a forecast metric related to dense fog formation. This was done by introducing a real-world “truth” observation at the location of greatest sensitivity. The results of this study indicate that ESA provides a cogent mesoscale sensitivity profile which can be used to accurately predict forecast changes in fog using initial condition potential temperature values. This type of information may prove valuable in planning the layout of future observational networks, as well as introduce the potential for performing data-thinning during data assimilation and real-time updates to forecast metrics.

THIS PAGE INTENTIONALLY LEFT BLANK



# TABLE OF CONTENTS

|      |  |    |
|------|--|----|
| I.   | INTRODUCTION.....  | 1  |
| A.   | MOTIVATION.....  | 1  |
| B.   | PROBLEM STATEMENT.....   | 1  |
| C.   | RESEARCH OBJECTIVES.....   | 4  |
| II.  | BACKGROUND.....  | 7  |
| A.   | DATA ASSIMILATION AND THE DEVELOPMENT OF THE<br>ENSEMBLE KALMAN FILTER ..... | 7  |
| B.   | SENSITIVITY ANALYSIS .....   | 8  |
| C.   | ENSEMBLE SENSITIVITY ANALYSIS.....   | 10 |
| III. | DATA AND METHODOLOGY .....   | 13 |
| A.   | LINEARITY TESTING .....  | 13 |
| B.   | ESA CALCULATION .....  | 15 |
| C.   | STATISTICAL SAMPLING ERROR .....   | 16 |
| D.   | MODEL CONFIGURATION .....  | 17 |
| 1.   | Nesting Configuration .....  | 17 |
| 2.   | Vertical Coordinate System .....   | 18 |
| 3.   | Physics .....  | 20 |
| 4.   | Data Assimilation Process.....   | 21 |
| a.   | <i>Truth Run</i> .....   | 21 |
| b.   | <i>Ensemble System</i> .....   | 21 |
| c.   | <i>Covariance Localization and Covariance Inflation</i> ...                  | 23 |
| E.   | REGIONAL OVERVIEW .....  | 24 |
| 1.   | Geography of Great Salt Lake Basin.....                                      | 24 |
| 2.   | Fog at Salt Lake City International Airport .....                            | 26 |
| F.   | ATMOSPHERIC CHARACTERIZATION .....   | 29 |
| 1.   | Synoptic Analysis.....   | 29 |
| 2.   | Precursor Rain Event .....   | 32 |
| 3.   | Dense Fog Event.....   | 38 |
| 4.   | Relation of Physical Interpretation to ESA.....                              | 39 |
| G.   | PARAMETERS .....   | 39 |
| 1.   | Type Selected For Study .....  | 39 |
| 2.   | Configuration of Parameters .....  | 40 |
| IV.  | RESULTS .....  | 43 |
| A.   | WRF ENSEMBLE PREDICTIONS.....  | 43 |
| 1.   | Moisture in GSL Basin .....  | 43 |
| 2.   | Moisture at KSLC.....  | 44 |
| B.   | QUANTITATIVE RESULTS .....   | 47 |
| 1.   | ESA (6 hour) .....   | 48 |
| 2.   | ESA (12 hour) .....  | 51 |
| 3.   | Linear Correlation.....  | 54 |
| 4.   | Support for Conceptual Model .....   | 58 |

|    |   |     |
|----|---|-----|
| C. | SENSITIVITY TESTING .....                             | 61  |
| 1. | Perturbation Tests .....                              | 62  |
| a. | $+1\sigma_T$ Perturbation Test .....                  | 63  |
| b. | “Truth” Perturbation Test.....                        | 66  |
| 2. | ESA Predicted Sensitivity Test.....                   | 71  |
| a. | $+1\sigma_T$ Perturbation Test .....                  | 72  |
| b. | “Truth” Observation Test .....                        | 72  |
| 3. | Actual Versus Expected Forecast Change .....          | 73  |
| D. | ENSEMBLE SIZE TESTING .....                           | 74  |
| 1. | 6-hour ESA .....                                      | 75  |
| 2. | 12-hour ESA .....                                     | 77  |
| 3. | Linearity of the 6-hour Positive Sensitivities .....  | 79  |
| 4. | Linearity of the 12-hour Positive Sensitivities ..... | 82  |
| 5. | Ensemble Size Conclusions .....                       | 86  |
| V. | CONCLUSIONS AND FUTURE WORK .....                     | 88  |
| A. | COMPARISON TO CHILCOAT (2012) RESULTS .....           | 91  |
| B. | POTENTIAL NETWORK DESIGN .....                        | 92  |
| C. | APPLICABILITY TO U.S. MILITARY.....                   | 95  |
| D. | FUTURE WORK.....                                      | 96  |
|    | LIST OF REFERENCES.....                               | 99  |
|    | INITIAL DISTRIBUTION LIST .....                       | 103 |

## LIST OF FIGURES

|            |  |    |
|------------|--|----|
| Figure 1.  | A special operations weather team operator out of Hurlburt Field enables a remote cloud pod during a training operation for Red Flag-Alaska 10-2 April 15, 2010, Eielson Air Force Base, Alaska. ....  | 2  |
| Figure 2.  | Plot showing the effective equivalence of adjoint and ensemble sensitivity methodologies.....  | 11 |
| Figure 3.  | Telescoping nested configuration used in this study. ....  | 18 |
| Figure 4.  | ARW $\eta$ coordinate (From Skamarock et al. 2008) .....   | 19 |
| Figure 5.  | Data Assimilation Cycle used for this project.....   | 23 |
| Figure 6.  | Map of Great Salt Lake with primary terrain features annotated. ....   | 25 |
| Figure 7.  | Dense fog occurrences at Salt Lake City International Airport by wind direction. (From Slemmer 2004).....  | 28 |
| Figure 8.  | 500 hPa Geopotential Height (m) Composite Mean change from 20 January 2009 to 23 January 2009. ....  | 30 |
| Figure 9.  | Hydrometeorological Prediction Center Surface Analysis from 2100 UTC on 23 January, 2009. (From <a href="http://www.hpc.ncep.noaa.gov/">http://www.hpc.ncep.noaa.gov/</a> ) ...  | 31 |
| Figure 10. | Hydrometeorological Prediction Center 500 hPa upper-air analysis containing observations, heights, and temperatures for 1200 UTC 23 January 2009. The black box indicates the positioning of the weak disturbance moving through northern Utah on 23 January 2009. ....  | 33 |
| Figure 11. | Radar imagery over Salt Lake Basin from 1800 UTC 23 January 2009 .....   | 34 |
| Figure 12. | 1200 UTC 23 January 2009 sounding from KSLC indicating presence of strong low-level inversion.....   | 35 |
| Figure 13. | 0000 UTC 24 January 2009 sounding from KSLC indicating that the low-level inversion has been ameliorated.....  | 36 |
| Figure 14. | 1200 UTC 24 January 2009 sounding from KSLC indicating the reformation of the low-level inversion. ....  | 37 |
| Figure 15. | Histograms of ensemble analysis potential temperature ( $\theta$ ) for the lowest model level at 1200 UTC 23 January 2009 for (a.) the most sensitive grid point in the innermost domain, (Y=52, X=121) and (b.) an adjacent grid point (Y=51, X=121). The red line indicates the normal distribution while the blue bars indicate the probability density function of $\theta$ at each grid point. .... | 42 |
| Figure 16. | Ensemble mean $q_v$ (in $\text{kg kg}^{-1}$ ) at $\eta_{-1}$ in 3-hour intervals, clockwise from top left, from 1800 UTC 23 January to 0600 UTC 24 January. UTC annotated as Z. 96-member ensemble initialized at 1800 UTC 23 January. Approximate position of KSLC is represented by black star. Warm colors represent stronger concentration of water vapor. .   | 44 |
| Figure 17. | Ensemble mean forecast 20-meter and 2-meter $q_v$ at KSLC versus observed $q_v$ at KSLC. The red solid line represents 20-meter $q_v$ for the forecast initialized at 1800 UTC 23 January while blue solid line  |    |

|            |  |    |
|------------|--|----|
|            | represents 2-meter $q_v$ from the same initialization. The $q_v$ recorded at the airport is represented by the blue dashed line. Both forecasts end at 0600 UTC 24 January. ....   | 46 |
| Figure 18. | Sensitivities ( $dJ/dx_i$ ) using 1800 UTC 23 January analysis potential temperature (in K) as $x_i$ , and forecasted $q_v$ (in $\text{kg kg}^{-1}$ ) as $J$ , valid at 0000 UTC 24 January. ....  | 49 |
| Figure 19. | WRF terrain map indicating elevations between 1000m and 2000m. The black circle (#1) identifies the elevated terrain near the grid point where the strongest 6-hour ESA sensitivity response is located. Other numbers (#2-7) indicate other regions important to the sensitivity response. .... | 50 |
| Figure 20. | Ensemble mean $\theta$ (K) at $\eta_{-1}$ at 1800 UTC 23 January. The most sensitive 6-hour ESA grid point is marked in the black circle (#1), near the strongest concentration of warm air, south of the GSL. Other numbers (#2-7) indicate other regions of sensitivity importance. ....       | 50 |
| Figure 21. | Sensitivities ( $dJ/dx_i$ ) using 1200 UTC 23 January analysis potential temperature (in K) as $x_i$ , and forecasted $q_v$ (in $\text{kg kg}^{-1}$ ) as $J$ , valid at 0000 UTC 24 January. ....  | 52 |
| Figure 22. | Scatterplot of 1800 UTC 23 January analysis $\theta$ at the most sensitive grid point and forecasted $q_v$ at KSLC at 0000 UTC 24 January. ....  | 55 |
| Figure 23. | Scatterplot of 1200 UTC 23 January analysis potential temperature at the 6-hour ESA most sensitive grid point and forecasted $q_v$ at KSLC at 0000 UTC 24 January. ....  | 56 |
| Figure 24. | Scatterplot of 1200 UTC 23 January analysis potential temperature at (a.) the most sensitive grid point from the 12-hour ESA and (b.) the second most sensitive grid point from the 12-hour ESA. Both are plotted against forecast $q_v$ at KSLC at 0000 UTC 24 January. ....                    | 58 |
| Figure 25. | Schematic interpretation of effects of 23 January 2009 mid-level disturbance and synoptically forced warm-air advection that led to a dense fog event at Salt Lake City International Airport on 24 January 2009. (After Google Maps). ....  | 59 |
| Figure 26. | Conceptual sensitivity field using 1200 UTC 23 January 2009 analysis temperature as the analysis state variable ( $x_i$ ) and $q_v$ at 0000 UTC 24 January 2009 as the forecast metric ( $J$ ) for the box centered over KSLC. (After Google Maps) ....  | 60 |
| Figure 27. | Conceptual sensitivity field using 1800 UTC 23 January 2009 analysis temperature as the analysis state variable ( $x_i$ ) and $q_v$ at 0000 UTC 24 January 2009 as the forecast metric ( $J$ ) for the box centered over the SLC airport. ....   | 61 |
| Figure 28. | Analysis change (in K) after the addition of $+1\sigma$ $\theta$ perturbation applied at $39.51^\circ\text{N}$ , $112.97^\circ\text{W}$ at the first $\eta$ -level. ....   | 64 |
| Figure 29. | Forecast difference in $q_v$ (in $\text{kg kg}^{-1}$ ) at 0000 UTC 24 January at the lowest model level ( $\eta_{-1}$ ) following the introduction of a $+1\sigma$ $\theta$  |    |

|            |  |    |
|------------|--|----|
|            | perturbation to the 1800 UTC 23 January ensemble analysis at the most sensitive grid point (black dot). ....   | 65 |
| Figure 30. | 1800 UTC 23 January analysis change (in K) after the addition of “truth” observation applied at 39.51°N, 112.97°W at $\eta_{-1}$ . The observation point is indicated by the black dot. Positive values indicate an increase in $\eta_{-1}$ temperatures, while negative values indicate a decrease. Note the very strong negative response in $\theta$ in the Salt Lake Valley, directly over the KSLC J-box.....   | 68 |
| Figure 31. | Forecast difference in $q_v$ (in kg kg <sup>-1</sup> ) at 0000 UTC 24 January at the lowest model level ( $\eta_{-1}$ ) following the introduction of a “truth” perturbation to the 1800 UTC 23 January ensemble analysis at the most sensitive grid point (black dot) .....   | 70 |
| Figure 32. | Schematic representing how expected change in $J$ ( $\delta J$ ) is calculated for (1) $+1\sigma$ perturbation and (2) “truth” perturbation. The x-axis shows temperature (in K) at the most sensitive grid point in the domain. The y-axis shows the corresponding forecast $q_v$ at KSLC at a later time. The correlation shown is idealized as perfectly linear. ....   | 72 |
| Figure 33. | Plot of 6-hour sensitivity ( $dJ/dx_i$ ) for 96, 80, 64, and 48-member ensemble systems using initial condition $T$ (K) from 1800 UTC 23 January 2009 and forecast $q_v$ (kg kg <sup>-1</sup> ) at KSLC at 0000 UTC 24 January 2009. Units are kg kg <sup>-1</sup> K <sup>-1</sup> . Number boxes identify grid points of the strongest three sensitivities in each plot. Markers indicating (+) or (-) represents a positive or negative sensitivity that exists outside the graphic. Top left number represents number of ensemble members used to perform ESA. Note: scales are not normalized..... | 76 |
| Figure 34. | Plot of 12-hour sensitivity ( $dJ/dx_i$ ) for 96, 80, 64, and 48-member ensemble systems using initial condition $T$ (K) from 1800 UTC 23 January 2009 and forecast $q_v$ (kg kg <sup>-1</sup> ) at KSLC at 0000 UTC 24 January 2009. Units are kg kg <sup>-1</sup> K <sup>-1</sup> . Number boxes identify grid points of the strongest three sensitivities in each plot. Markers indicating (+) or (-) represent a positive or negative sensitivity that exists outside the graphic. Top left number represents number of ensemble members used to perform ESA. Note: scales are not normalized..... | 78 |
| Figure 35. | Scatterplots of analysis $\eta_{-1}$ temperature and forecasted $q_v$ used in the ESA as ensemble size is reduced from 96 to 48 members. The x-axis represents the 1800 UTC 23 January analysis temperature (in K) at the most sensitive grid point (39.5°N, 112.9°W). The y-axis represents the forecasted $q_v$ value (in kg kg <sup>-1</sup> ) six hours later, valid 0000 UTC 24 January. Also plotted are correlation coefficient ( $r$ ) and sensitivity ( $dJ/dx$ ). ....   | 80 |
| Figure 36. | 6-hour ESA chart of correlation in red and sensitivity in blue versus the number of ensemble members for a single point of positive  |    |

|            |  |    |
|------------|--|----|
|            | sensitivities at 39.5°N, 112.9°W. Green bars indicate the high and low boundaries of the 95% confidence interval and represent the associated sampling error. ....   | 81 |
| Figure 37. | Scatterplots of analysis $\eta_{-1}$ temperature and forecasted $q_v$ used in the ESA as ensemble size is reduced from 96 to 48 members. The x-axis represents the 1800 UTC 23 January analysis temperature (in K) at the 12-hour ESA indicated most sensitive grid point (39.5°N, 112.9°W). The y-axis represents the forecasted $q_v$ value (in kg kg <sup>-1</sup> ) 12 hours later, valid 0000 UTC 24 January. Also plotted are correlation coefficient (r) and sensitivity ( $dJ/dx$ ).....                         | 83 |
| Figure 38. | Scatterplots of analysis $\eta_{-1}$ temperature and forecasted $q_v$ used in the ESA as ensemble size is reduced from 96 to 48 members. The x-axis represents the 1200 UTC 23 January analysis temperature (in K) at the 12-hour ESA indicated most sensitive grid point (8km N and 4 km E of 39.5°N, 112.9°W). The y-axis represents the forecasted $q_v$ value (in kg kg <sup>-1</sup> ) twelve hours later, valid 0000 UTC 24 January. Also plotted are correlation coefficient (r) and sensitivity ( $dJ/dx$ )..... | 84 |
| Figure 39. | 12-hour ESA chart of correlation in red and sensitivity in blue versus the number of ensemble members for a single point of positive sensitivities at the most sensitive grid point for the 12-hour ESA, 8km N and 4km E of 39.5°N, 112.9°W. Green bars indicate the high and low boundaries of the 95% confidence interval and represent the associated sampling error. ....  | 85 |
| Figure 40. | Same as Figure 38, with 12-hour ESA indicated second most sensitive grid point (28km N and 12 km E of 39.5°N, 112.9°W) .....   | 85 |
| Figure 41. | Same as Figure 39, for a grid point 28 km N and 12 km E of 39.5°N, 112.9°W. This grid point is the second most sensitive grid point in the 12-hour ESA. ....   | 86 |
| Figure 42. | Locations of strong and/or reliable temperature sensitivity regions that are considered important in forecasting $q_v$ at Salt Lake City International Airport .....   | 93 |
| Figure 43. | Chilcoat's map of locations of the strong sensitivities that are considered important in forecasting the amount of moisture received at the SLC International Airport. (From Chilcoat 2012) .....  | 94 |

## LIST OF TABLES

|          |  |    |
|----------|--|----|
| Table 1. | Approximate above-ground level (AGL) height for $\eta$ -levels in the lowest 500 meters of the atmosphere.....   | 20 |
| Table 2. | WRF-ARW physics options selected for this study.....   | 21 |
| Table 3. | Comparison of Actual versus Expected $q_v$ changes in $\text{kg kg}^{-1}$ at KSLC at 0000 UTC 24 January with (1) $+1\sigma$ Perturbation (K) and with (2) “Truth” Observation (K) at 6-hour ESA most sensitive grid point at 1800 UTC 23 January..... | 74 |

THIS PAGE INTENTIONALLY LEFT BLANK



## LIST OF ACRONYMS AND ABBREVIATIONS

|         |   |
|---------|---|
| 3DVAR   | Three-Dimensional Variational Data Assimilation |
| ARW     | Advanced Research WRF                           |
| AFWA    | Air Force Weather Agency                        |
| AOR     | Area of Responsibility                          |
| CDF     | Cumulative Distribution Function                |
| CI      | Confidence Interval                             |
| CWSU    | Center Weather Service Unit                     |
| DA      | Data Assimilation                               |
| DART    | Data Assimilation Research Test Bed             |
| DSL     | Deep Stable Layer                               |
| EAKF    | Ensemble Adjustment Kalman Filter               |
| EM      | Ensemble Mean                                   |
| EnKF    | Ensemble Kalman Filter                          |
| ESA     | Ensemble Sensitivity Analysis                   |
| GSL     | Great Salt Lake                                 |
| hPa     | Hectopascal                                     |
| ICAO    | International Civil Aviation Organization       |
| MATLAB  | Matrix Laboratory                               |
| NARR    | North America Regional Reanalysis               |
| NCAR    | National Center for Atmospheric Research        |
| NWP     | Numerical Weather Prediction                    |
| NWS     | National Weather Service                        |
| OI      | Optimal Interpolation                           |
| OLS     | Ordinary Least Squares Regression               |
| PBL     | Planetary Boundary Layer                        |
| P-Value | Probability Value                               |
| PWAT    | Precipitable Water                              |
| RH      | Relative Humidity                               |
| RPA     | Remotely Piloted Aircraft                       |
| RRTM    | Rapid Radiative Transfer Model                  |

|      |  |
|------|--|
| SLC  | Salt Lake City                           |
| SLP  | Sea Level Pressure                       |
| SM   | Statute Mile                             |
| SCM  | Successive Correction Method             |
| TWR  | Tactical Weather Radar                   |
| TMOS | Tactical Meteorological Observing System |
| USAF | United States Air Force                  |
| WRF  | Weather Research and Forecasting         |
| WS   | Wind Speed                               |
| WSM5 | WRF Single-Moment Five-Class             |

## **ACKNOWLEDGMENTS**

Thank you to my advisor, Professor Josh Hacker. Your guidance, instruction and patience throughout this project allowed me to explore the subject in meaningful and hopefully, relevant ways. Thanks to my second reader, Dr. James Doyle. Your well-crafted feedback helped clarify and shape my understanding of ensembles, numerical weather prediction, and sensitivity analysis. Thanks also to Major Paul Homan. Your guidance on ESA and the WRF model were crucial to my understanding of these complex subjects. Your assistance allowed me to move forward with ideas and tests necessary to complete my thesis, and I am very grateful.

Thank you to my wife and family, whose love and support provides a source of continual inspiration and happiness.

Thanks to my classmates for their assistance and camaraderie over the past 18 months.

Finally, thanks to the Air Force, and Air Force Weather leadership, for providing this extremely rewarding opportunity to further educate myself in the field of meteorology. The potential pursuit of a master's degree in meteorology provided a significant motivation to me as a junior officer, and I hope this unique opportunity remains open for all that follow and seek the same.

THIS PAGE INTENTIONALLY LEFT BLANK

# **I. INTRODUCTION**

## **A. MOTIVATION**

The ability of a weather forecaster to accurately predict beyond the near term is predicated on the ability to draw upon accurate and timely numerical weather prediction (NWP) information to make an informed meteorological outlook. While notable improvements in short-term (less than 48 hours), medium-term (usually 48-96 hours), and long-term (greater than 96 hours) forecasts were made from the late 1970s to the early 1990s, recent improvement in short-term forecasting has been more limited (Kalnay 2003). It is believed that advancement in NWP will likely come from a variety of improvements, including the creation of more sophisticated data assimilation, improved ensemble forecasting, employment of fully coupled atmospheric-hydrological systems, and more detailed atmosphere-ocean-land coupled models (Kalnay 2003). One additional field of improvement that is the focus of this study is the development of adaptive observing strategies, by which “additional observations are placed where ensembles indicate there is rapid error growth (low predictability)” (Kalnay 2003).

## **B. PROBLEM STATEMENT**

United States Air Force commanders, much like their counterparts in the private sector, are commonly constrained by fiscal limitations when tasked to execute operational objectives. For Air Force weather commanders, these objectives include the requirement to observe and characterize current and future weather conditions for military operations. The accuracy of these operational products is contingent upon the deployment of accurate, reliable weather sensors as well as access to accurate and reliable NWP products. These elements are not unrelated, as an accurate meteorological observation can provide vital knowledge to a weather forecaster in the field while also informing a NWP system as to the true atmospheric conditions from which to create a more

accurate analysis. However, in a fiscally constrained environment the ability to field and maintain the necessary number of weather sensors can be impacted, thus limiting the flow of information to both human and computational forecast systems.

Recent years have seen the development of a variety of less expensive self-sustaining weather sensors. In the U.S. Air Force, a commonly used system is the “Weather Pod”, which measures standard surface data (temperature, dew point, surface pressure, wind speed and direction) and comes with optional visibility and cloud sensors. These systems can be deployed to the field at a fraction of the price of traditional tactical observing systems, which can exceed \$100,000.



Figure 1. A special operations weather team operator out of Hurlburt Field enables a remote cloud pod during a training operation for Red Flag-Alaska 10-2 April 15, 2010, Eielson Air Force Base, Alaska. The cloud pod is one of several sensors that make up the weather pod.  
(U.S. Air Force photo/Airman 1st Class Willard E. Grande II).  
(From <http://www.afweather.af.mil>)

These self-sustaining systems provide commanders additional capability to observe weather conditions at locations previously considered unobservable, either due to enemy activity or lack of field support (i.e., power or communications) for observation systems. The positioning of these sensors immediately becomes a concern for Air Force weather commanders who must

decide where to place them to maximize their usefulness in supporting military operations. In today's battlespace environment, these sensors likely accompany traditional atmospheric sensors, such as the TMQ-53 Tactical Meteorological Observing System (TMOS) that may or may not already be deployed through the rest of the area of responsibility (AOR). Other platforms may also be providing atmospheric data, including tactical weather radar (TWR), remotely piloted aircraft (RPA) such as the Predator vehicle, and the Aerostat, a tethered intelligence and surveillance airborne platform now common in skies over forward operating locations. Placement of the traditional TMOS systems has in the past been determined by the practical concerns noted above. However, if sensors, traditional or a more modern variety could be placed in the field that would provide both forecasters and forecast systems critical data that would improve their accuracy, this could greatly enhance meteorological support of military operations.

This study examines the potential for ensemble sensitivity analysis (ESA) to provide the capability to identify those geographic locations where a more accurate observation could most effectively improve a forecast. The Great Salt Lake (GSL) Basin provides an ideal environment to test ESA. With its highly varied terrain, partially limited upstream observing network—due to the sparse population density of the Intermountain West—and significant intra-annual seasonal variation, the GSL basin mimics a number of operating environments that the U.S. military operates in, including Afghanistan. By proving the efficacy of ESA to identify locations that provide the greatest impact on model accuracy, this system may serve as a model from which future sensor networks may be based upon to ensure observations are taken at locations that provide the most useful atmospheric information.

While ESA has shown itself to be effective at the synoptic scale, at long time scales, and in low model resolution, its usefulness in areas of complex terrain, in shorter time scales, and at high model resolution is less proven. One of the most important parameters to consider when supporting military aviation is

visibility, which can significantly degrade flying operations when restricted. The most common way for this to occur is in the presence of dense fog, which can reduce visibility below mandatory minimum operating thresholds, typically 1/2 statute mile (SM) or less, depending on the airfield, the aircraft type and the experience of the pilot in command. In mountainous terrain in wintertime, visibility is routinely reduced below operating threshold due to dense fog. The formation and advection of dense fog in the GSL Basin has been the focus of several studies (Hill 1987; Slemmer 2004) that identified the significant role that stable environment conditions and moisture from the GSL play in its formation.

This study seeks to identify those locations that most thoroughly capture the regional sensitivities to stability and moisture exhibited during a dense fog event in January 2009. This sensitivity analysis may yield a more thorough understanding of the predictability of fog forecasting in complex terrain through which atmospheric sensors may be placed more intelligently, potentially allowing more accurate fog forecasts in similar environments throughout the world.

### **C. RESEARCH OBJECTIVES**

The primary objective of this project is to further determine whether a mesoscale ESA can be used to identify the sensitivity profile of fog formation in a complex terrain environment. While this was also the primary objective of Chilcoat (2012), this study utilizes several alternate methodologies to achieve a similar objective, including a more realistic observing network and the implementation of a Gaussian filter, which is a prerequisite to properly utilize the linear statistics of the ESA system of Torn and Hakim (2008). The second objective, also similar to Chilcoat, is to determine whether the calculated sensitivities can be used to reduce forecast uncertainty for a forecast metric related to dense fog formation. This will be done by introducing a real-world “truth” observation at the location(s) in the GSL basin with greatest sensitivity to determine if a forecast improvement can be made. This type of information would prove highly valuable in planning the layout of a future observational



network, as well as introduce the potential for performing data-thinning during data assimilation and real-time updates to forecast metrics (Torn and Hakim 2008).

The establishment of the viability of the ESA within this mesoscale complex environment will be contingent on successful:

1. Evaluation of the linearity of the input variable (initial condition) and forecast variable through Gaussianity testing. The assumption of linearity is a prerequisite to achieving accurate and reliable results.

2. Introduction of a hypothetical synthetic observation at the location of greatest sensitivity and observation of a positive forecasting change through increased forecast accuracy (i.e., reduced forecast error).

3. Determination of the ensemble size needed for ESA to provide accurate sensitivity information for this region.

Based upon the results of this study, and those presented by Chilcoat (2012), a better assessment can be made on the usefulness of ESA as a tool for improving prediction in complex terrain environments.

THIS PAGE INTENTIONALLY LEFT BLANK

## **II. BACKGROUND**

The world meteorological forecasting community has long relied on numerical weather prediction (NWP) to provide the primary means of delivering accurate and reliable near-to-medium term weather outlooks. Improvements in NWP in recent decades can be attributed to the increased power of supercomputers, the improved representation of small-scale physical processes, the use of more accurate methods of data assimilation (DA), and increased availability of data (Kalnay 2003). The improvement in data assimilation methods has enabled a more accurate representation of the real atmosphere, thus providing more realistic initial conditions for model integration, and more accurate forecasts.

### **A. DATA ASSIMILATION AND THE DEVELOPMENT OF THE ENSEMBLE KALMAN FILTER**

The importance of DA for the accuracy of NWP has been established since at least the 1950s. NWP is an initial-value problem that considers a representation of the real atmosphere and integrates it forward to simulate the real atmosphere (Kalnay 2003). Because it is necessary to characterize the atmosphere at significantly more data points than can be realistically observed, a methodology was developed to “spread” the known observational information to the unobserved regions. Later, this process came to further include the correction of the model estimate of the atmosphere when it differed from the observation. This process, also known as performing the analysis, became the foundation for improving DA in the 1950s and 1960s. Early methods to perform this function included the use of climatology, the successive correction method (SCM) and optimal interpolation (OI) (Kalnay 2003).

A significant step forward came with the introduction of the three-dimensional variational data assimilation (3DVAR) system in the early 1990s (Kalnay 2003). This system, based largely on the work of Sasaki from the late

1950s through early 1970s (Lewis and Lakshmivarahan 2008), used understanding of established dynamical relationships to identify covariance relationships which could in turn be used to perform the model analysis. These dynamical relationships were determined through sampling methods over long periods of time and utilizing multiple case studies (Hakim and Torn 2008). The limitation of this system lies in its deterministic method of performing state estimation, which fails to account for known errors in initial conditions that have identifiable limitations on predictability (Lorenz 1963).

An important advancement was made when Evensen (1994) successfully implemented a Kalman filter using ensemble techniques to determine the forecast-error statistics. This technique is notably different from 3DVAR and is known as an ensemble Kalman filter (EnKF). The EnKF provides a systematic, temporally evolving means of determining the error statistics, which are essentially the forecast-error statistical covariances. This data may then be used to adaptively alter the DA process to provide greater emphasis (more weighting) to those model areas with less statistical error, and less emphasis (less weighting) to those model areas with more statistical error. By providing probabilistic, flow-dependent estimates of error statistics, the EnKF provides the basis for the technique used in this study, ensemble sensitivity analysis (ESA).

## **B. SENSITIVITY ANALYSIS**

While success was being made in the implementation of these ensemble methods in the late 1990s, and early 2000s, the area of sensitivity analysis was attracting considerable research. By definition, this involves the study of how uncertainty in model output (numerical or otherwise) can be related to differing sources of uncertainty in the model input (Saltelli et al. 2004). Within a meteorological context, this began by seeking to understand how chosen aspects of a synoptic feature may change due to alterations in physical or dynamical processes, or initial atmospheric conditions (Errico 1997). Analysis of this nature offered the opportunity to provide insight into relationships between model input

and output, possibly identifying model forecast error that may be caused by boundary or initial conditions. A secondary use was to determine what initial synoptic features most strongly related to dependent synoptic features are later times (Langland et al. 1995). Identifying these relationships may help to provide a better understanding of the dynamics of forecast error, as well as identify possible locations to place additional observations to reduce forecast error (Torn and Hakim 2008).

Initial advancement in this field focused on measuring changes in forecast parameters by manipulating single input variables. This method, though simple to implement, failed to accurately identify the impact of all possible input perturbations on predicted forecast metrics, and its utility was determined to be limited (Errico 1997). A more advanced method was then developed to perform sensitivity analysis which relied upon the adjoints of tangent-linear models. The adjoint of a NWP model can be thought of as the transpose of the tangent linear of the NWP model itself. However, the limitations and difficulty of developing and maintaining tangent linear models is well documented (Hakim and Torn 2008; Torn and Hakim 2008; Ancell and Hakim 2007). Recent research has shown promise in computing the sensitivity analysis in a more straightforward manner.

This advancement involves the use of ensembles, rather than adjoints, to compute sensitivity analysis. This technique, ensemble sensitivity analysis (ESA), uses ensembles and probabilistic rather than deterministic analyses to estimate relationships between forecast metrics and initial conditions. This area of study has its roots in *targeting*, or *adaptive observational* experiments, which seek to understand where analysis and forecast improvement could be achieved through placement of additional observations (Hamill and Snyder 2002). In the late 1990s and early 2000s a multitude of studies were conducted and ideas proposed that sought the most efficient and valid means of solving this problem. These methods included the singular vector technique, ensemble spread technique, ensemble transform technique, and the ensemble transform Kalman filter, among several others (Hamill and Snyder 2002). Building on the concepts

put forth by Berliner et al. (1999) regarding forecast and analysis error statistics, and by Burgers et al. (1998) regarding background error covariance techniques, Hamill and Snyder proposed their own theoretical method of targeting observations using an EnKF to minimize analysis errors (Hamill and Snyder 2002).

### **C. ENSEMBLE SENSITIVITY ANALYSIS**

In 2005, a methodology based upon the EnKF and the sensitivity analysis work described above was codified as ESA, and was demonstrated to be a viable means of calculating state estimation (e.g., expected value), state uncertainty (e.g., variance) and the relationship between all variables at all locations in time (Hakim and Torn 2008). In their proposal, Hakim and Torn devised a method to compute the sensitivity of a forecast metric to changes in model initial conditions using Gaussian statistics and linear regression of model statistics determined by the ensemble members. In ESA, the uncertainty identified by Lorenz (1963) that accompanies the propagation of imperfect observations under nonlinear chaotic dynamics is accounted for by the production of instantaneous and independent state estimations that are provided by the ensemble analysis (Gombos and Hansen 2008). The utility of this method is that it provides a means of determining the possible implications of forecast error, and where this error may be reduced through active management of observation locations (Torn and Hakim 2008). In other words, this technique provides an optimal means of performing observation targeting. This technique has shown efficacy as an alternative to adjoint methods (Figure 2, Ancell and Hakim 2007), and also a successful means of determining forecast error in synoptic storms (Hakim and Torn 2008), storms undergoing extratropical transition (Torn and Hakim 2009), and in developing hurricanes (Torn 2010).

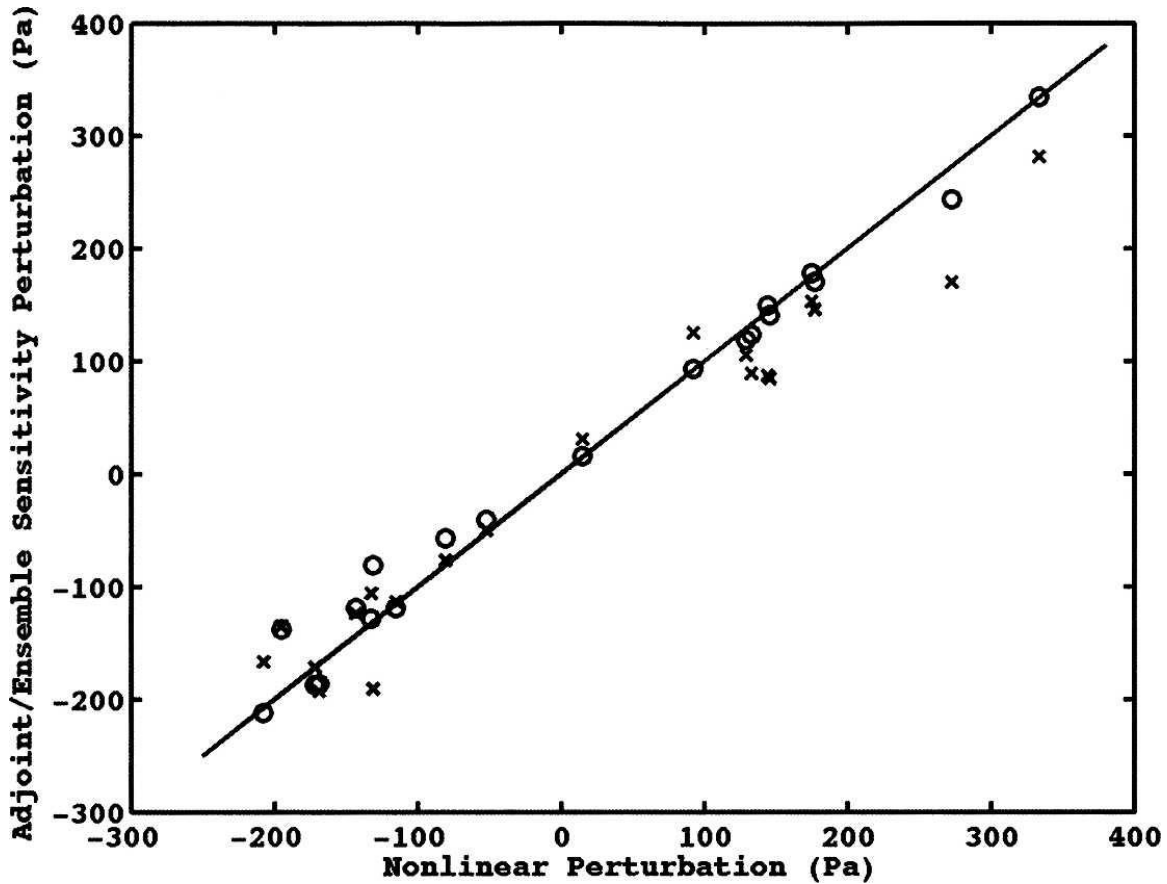


Figure 2. Plot showing the effective equivalence of adjoint and ensemble sensitivity methodologies. Plotted is the change in response function associated with both the statistical projection onto the adjoint sensitivity field (denoted by the symbol  $\circ$ ) and the ensemble sensitivity (denoted by the symbol  $\times$ ) versus the nonlinear change in response function for a statistically spread unit temperature perturbation made at 20 grid points throughout the model domain. (From Ancell and Hakim 2007)

Though successfully demonstrated as a viable alternative to adjoint-based methods, these studies applied ESA only on the synoptic scale and with relatively coarse models. Recent studies have begun to examine the efficacy of ESA for use in finer resolution models and at smaller horizontal scales (mesoscale and below). Chilcoat (2012) applied ESA techniques using an EnKF and high-resolution forecast models (4-km grid spacing) in complex terrain (Great Salt Lake Basin). Chilcoat demonstrated ESA as a useful methodology in accurately identifying geographic locations where sensitivity between an initial state variable ( $u$ -wind) and a forecast parameter (fog, represented as water

vapor mixing ration,  $q_v$ ) was greatest. The next step, and the purpose of this research, is to validate the sensitivities identified by Chilcoat and then to determine if a more accurate forecast can be created by adding an observation at these locations.



### **III. DATA AND METHODOLOGY**

The methodology used in this research is based upon the ensemble sensitivity technique defined in the Background section of this thesis. To fully understand how ESA works and how it was used for this research, it is necessary to first identify the procedure. Gombos and Hansen describe ESA as a method of “statistically inferring synoptic dynamical relationships from the covariability of fields’ ensemble analysis” (Gombos and Hansen 2008). Stated another way, this method seeks to identify statistical relationships between observations (initial conditions) and forecast fields and then to draw conclusions from the results that can be equated to the dynamic relationships that exist between the fields. This technique is part of an emerging field of study that uses underlying error statistics such as the variance and covariance of error in observations, model analysis, and model background fields, to identify relationships within complex nonlinear systems. These statistical relationships are based upon linear regression and therefore are subject to the limitations of linear statistics which assume normally distributed data fields, with variation in the distributions attributable to normally distributed random error.

#### **A. LINEARITY TESTING**

To test these assumptions and thus the validity of the linear regressions used in this technique, the Gaussianity of the distributions must be examined. Wilks defined linear regression as an attempt to “summarize the relationship between two variables, shown graphically in their scatterplot, by a single straight line” (Wilks 2006). Simple linear regression defines the linear relationship that exists between two variables, typically  $x$  (independent or predictor variable) and  $y$  (dependent or predictand variable). This linear relationship is defined by the equation  $y = mx + b$  where  $m$  is the slope of the line and  $b$  is the  $y$ -intercept. The line that is created during this procedure, the best fit line, will produce the least error in expected value of  $y$ , when given values of  $x$ . This error minimization is

achieved by finding the lowest sum of squared errors between the values of  $y$ , after inputting the values for  $x$ . This is also known as ordinary least squared regression (OLS).

The assumption made with linear regression is that the given  $x$  and  $y$  variables are normally distributed, also known as a Gaussian distribution. To determine whether or not these variables are Gaussian, we applied a Lilliefors test to the variable sets. The Lilliefors test, a variation of the Kolmogorov-Smirnov test, is a two-sided goodness-of-fit test that measures the distribution of each variable set (empirical) to determine how well it compares against the known normal distribution (theoretical). To perform this test, we propose the null hypothesis that the empirical data comes from a normally distributed population. The alternative is that the data does not come from a normal distribution. The test statistic used is defined as:

$$D_n = \max_x |F_n(x) - F(x)|$$

where  $F_n(x)$  is the empirical cumulative distribution function (CDF) estimated from the sample and  $F(x)$  is the normal CDF. The mean and standard deviation of both CDFs must be equal. The test statistic  $D_n$  determines the largest total difference between the empirical and theoretical CDF. The computed test statistic is then related to a critical value using a table. Matrix Laboratory (MATLAB) uses a table of critical values that have been computed using a Monte Carlo simulation for sample sizes less than 1000, and significance levels ( $\alpha$ ) between 0.001 and 0.50. If after performing the test the total difference between the empirical and theoretical CDF's is too great, a test statistic is returned that exceeds the significance level and the null hypothesis will be rejected. When this occurs, the data is rejected for its failure to be reliably drawn from a normally distributed population. The significance level chosen for this study for this test is 0.05.

The Lilliefors test in this study was completed upon both the observed variable ( $x$ ) and the forecast metric ( $J$ ), as the assumption of Gaussianity applies equally to both variables. Non-Gaussian observed and forecast metrics were rejected if they failed to pass the the Lilliefors test. By selecting only data sets that have Gaussian distributions, we hoped to ensure the assumptions of linear statistics are upheld.

## **B. ESA CALCULATION**

The linear regression defined in 3.A. was identified by Torn and Hakim in 2008 as ESA, a calculation of the sensitivity of the forecast metric to the initial conditions (Torn and Hakim 2008). The authors showed that sensitivity of a forecast metric  $J$  to an initial analysis state variable  $x_i$  is defined, in scalar form, by

$$\frac{\partial J}{\partial x_i} = \frac{\text{cov}(J, x_i)}{\text{var}(x)_i}.$$

Covariance, which quantifies the strength of the linear relationship between the two arguments, is denoted by cov while var, which quantifies how far the population is spread from the mean, is the variance. In scalar form,  $x_i$  represents the analysis state variable for a single grid point. Any physical variable can be represented by  $x_i$ , samples of which are provided by an ensemble of size  $M$ . Provided that an EnKF is used for assimilating observations, this ensemble system provides estimates of the ensemble mean values of state variable and forecast metric, from which sensitivities across the entire grid may be computed.

To further identify the linear dependence between the two variables  $J$  and  $x_i$  the Pearson product-moment coefficient of linear correlation, or correlation coefficient (Wilks 2006), is introduced to the ESA equation. This value is defined by the equation

$$r_{J,x_i} = \frac{\text{cov}(J, x_i)}{\sigma_J (\sigma_x)_i}$$

where  $r_{J,x_i}$ , a unit-less measure, is the correlation coefficient between  $J$  and  $x_i$ , while  $\sigma_J$  and  $\sigma_x$  represent the standard deviation of the sample of the respective variables. This equation can be rewritten as

$$\text{cov}(J, x_i) = r_{J,x_i} \sigma_J (\sigma_x)_i.$$

If we then substitute this equation into our original ESA equation, the updated form, with  $\text{var}(x)_i$  rewritten in symbolic form, appears as

$$\frac{\partial J}{\partial x_i} = \frac{r_{J,x_i} \sigma_J (\sigma_x)_i}{(\sigma_x^2)_i}.$$

This after cancellation becomes

$$\frac{\partial J}{\partial x_i} = \frac{r_{J,x_i} \sigma_J}{(\sigma_x)_i}.$$

This new form of Hakim and Torn (2008) can be used to apply a confidence interval test to account for sampling error.

This study seeks to define the sensitivity  $dJ/dx_i$  between the observed variable  $x_i$ , represented as a column state vector  $\mathbf{x}$  containing near surface temperature values and the forecast metric  $J$  as the water vapor mixing ratio,  $q_v$ , at our point of interest, the Salt Lake City International Airport.

### C. STATISTICAL SAMPLING ERROR

Because the ensemble system draws upon a finite sample, sampling error is naturally introduced into the ESA. As identified by Hakim and Torn (2008), it is necessary to ensure that the determined sensitivities are statistically significant in order to limit sampling error.

To account for this sampling error, we will perform a confidence test at the 95% confidence interval, for which the null hypothesis is that changes to input

variable  $x_i$  do not change the forecast metric  $J$ . We will reject this hypothesis if the absolute value of the correlation coefficient identified in 3.B. exceeds the 95% confidence bounds as estimated by the ensemble data (Torn and Hakim 2008).

We seek to define the probability, or p-value, which reflects the measure of evidence against our formulated null hypothesis. A small p-value,  $p[J, x_i]$ , will correspond to strong evidence that we can accept the correlation coefficient,  $r[J, x_i]$ , which accompanies each sensitivity calculation. Working within MATLAB the p-values were determined by utilizing the correlation coefficients to generate a test statistic with  $N-2$  degrees of freedom. These associated values are then used to test the null hypothesis. With a 95% confidence interval (CI), when low p-values (less than 0.05) are calculated, we can conclude that the correlation coefficients are statistically significant, which equates to the rejection of the null hypothesis. This test is performed for each sensitivity calculation and locations with correlation coefficients that fail the statistical significance test are rejected and data provided from these points is masked.

#### **D. MODEL CONFIGURATION**

The ensemble system used in this research is the Advanced Research version of the Weather Research and Forecasting model (WRF-ARW, version 3.2.1). The unique contribution of the ARW subset comes from the addition of a dynamics solver and specific physics schemes, numerical/dynamics options, initialization routines, and a data assimilation package (Skamarock et al. 2008).

##### **1. Nesting Configuration**

The ensemble system configuration will mirror that used by Chilcoat (2012), with a telescoping fixed nested grid with 36-km horizontal grid spacing on the outermost domain, 12-km horizontal grid spacing on the middle domain, and 4-km grid spacing on the innermost domain. All domains in the model contain 60 vertical  $\eta$ -levels, each with upper atmospheric boundary set at 100 hPa. The telescoping grid domains are pictured in Figure 3. The innermost domain lies over the central Intermountain West and is centered slightly to the west of the

Great Salt Lake. The dimensions of this inner domain include 222 x 183 grid points which cover an area 888 km x 732 km.

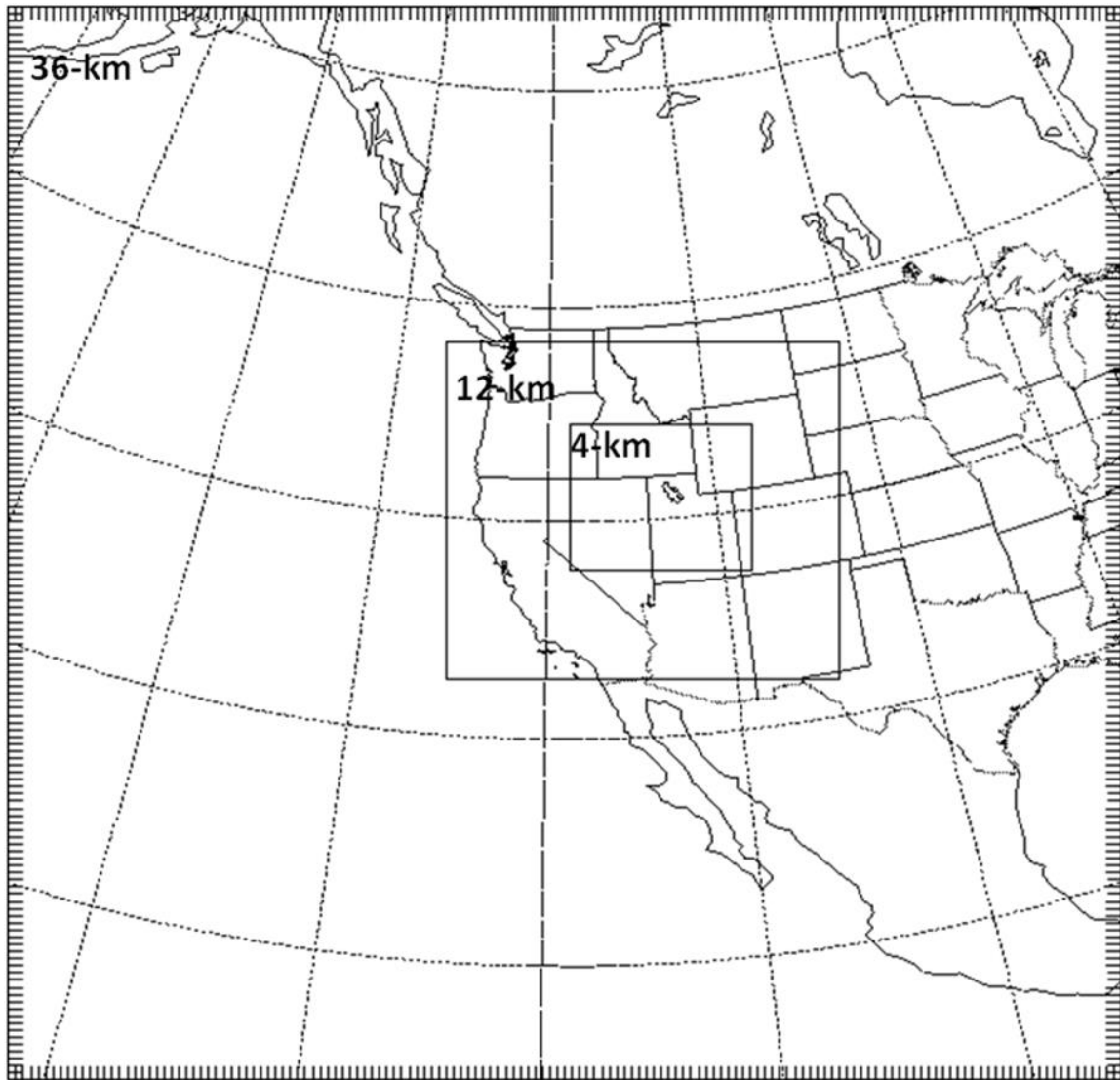


Figure 3. Telescoping nested configuration used in this study. The outermost grid domain uses 36-km horizontal grid spacing, the middle domain uses 12-km horizontal grid spacing and the innermost domain uses 4 km horizontal grid spacing. (From Chilcoat 2012)

## 2. Vertical Coordinate System

The WRF-ARW vertical coordinate system has been established with terrain-following, dry hydrostatic pressure, with vertical grid stretching permitted

(Skamarock et al. 2008). The vertical coordinates are denoted by  $\eta$  and vary from a value of 1 at the surface to 0 at the upper boundary of the model domain. Figure 4 shows a visual representation of the vertical coordinate system. Because the primary focus of this study was dense fog formation and advection at the surface and near-surface level, the two lowest  $\eta$ -levels were of most importance. Table 1 shows the approximate height of the  $\eta$ -levels in the lowest 500 meters of the atmosphere.

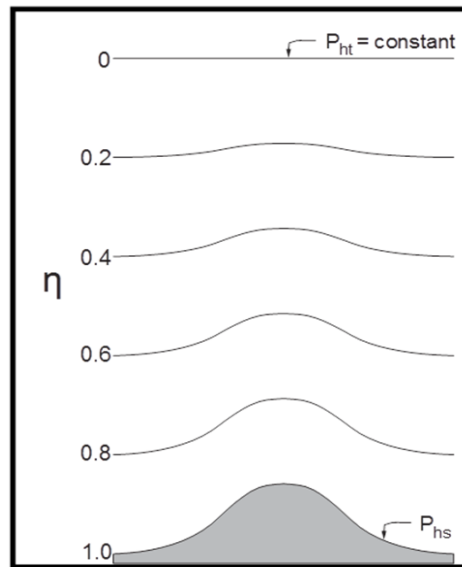


Figure 4. ARW  $\eta$  coordinate (From Skamarock et al. 2008)

| $\eta$ -Level | AGL Height (m) |
|---------------|----------------|
| 1             | 25             |
| 2             | 60             |
| 3             | 107            |
| 4             | 166            |
| 5             | 240            |
| 6             | 334            |
| 7             | 446            |
| 8             | 513            |

Table 1. Approximate above-ground level (AGL) height for  $\eta$ -levels in the lowest 500 meters of the atmosphere.

### 3. Physics

WRF-ARW separates physics options into five categories, each of which contain several options. The primary physics categories include (1) microphysics, (2) cumulus parameterization, (3) planetary boundary layer (PBL), (4) land-surface model, and (5) radiation (Skamarock et al. 2008). For this study, the physics options selected are the same as those used operationally by the Air Force Weather Agency (AFWA) in their deterministic WRF model. The microphysics scheme used for this study is the WRF Single-Moment 5-class (WSM5) scheme. This scheme allows water to be held in five separate hydrometeorological categories and is efficient in intermediate grids between the cloud-resolving grids and the mesoscale grids (Skamarock et al. 2008). Also used is the Kain-Fritsch cumulus parameterization (Kain 2004), though it was enabled on the two outermost grids only, as cumulus parameterizations can be considered theoretically valid only on course grid scales, generally greater than 10 km (Skamarock et al. 2008). The planetary boundary layer (PBL) scheme implemented is the Yonsei University PBL scheme (YSU PBL) (Hong et al. 2006), while the land surface model is the Noah (Ek et al. 2003). Finally, the radiation parameterization scheme implemented was the rapid radiative transfer model (RRTM; Mlawer et al. 1997) for longwave processes and the Dudhia



shortwave scheme (Dudhia 1989) for shortwave processes. Table 2 summarizes the physics parameterizations selected for this study.

| Microphysics | Cumulus      | PBL | LSM  | Longwave | Shortwave |
|--------------|--------------|-----|------|----------|-----------|
| WSM5         | Kain-Fritsch | YSU | Noah | RRTM     | Dudhia    |

Table 2. WRF-ARW physics options selected for this study.

#### 4. Data Assimilation Process

Data Assimilation (DA) was performed with the Data Assimilation Research Testbed (DART). DART is a community software environment created for ensemble DA research, developed and maintained at the National Center for Atmospheric Research (NCAR) (Anderson et al. 2009). For this project DART was run on Cray XE6 supercomputers at the U.S. Army Engineer Research and Development Center (ERDC) in Vicksburg, Mississippi.

##### *a. Truth Run*

To recreate the conditions that supported this dense fog event, an observing system simulation experiment (OSSE) was conducted. The purpose of this experiment was to provide a WRF-based synthetic “truth” representation which resembled the true state of the atmosphere as closely as possible. The WRF “truth” simulation was initialized at 0000 UTC on 19 January 2009 using conditions provided by the North American Regional Reanalysis (NARR). Lateral boundary conditions were drawn from NARR, with perturbations implemented per Torn et al. (2006). From this point, the WRF soil conditions were reset every three hours to NARR-provided values to ensure surface-based boundary layer forcing mimicked reality as closely as possible. This simulation provided a database to test the results of our experiments against.

##### *b. Ensemble System*

Conditioning of the WRF ensemble system began at 0000 UTC on 20 January. DA proceeded every three hours through the introduction of

available “truth” rawinsonde observations that were recorded across the outer grid domain during this time. While Chilcoat (2012) introduced synthetic rawinsonde observations at 100 random locations across the domain to simulate a sparse data environment, the approach in this study provides observations that spatially represent the rawinsonde data network present in western North America. Besides the introduction of lateral boundary conditions and soil reset from NARR, no other observations were added to the system. For two days, the ensemble was integrated forward until 0000 UTC on 22 January 2009, when it was concluded, as shown by Torn et al. (2006), that the perturbations entering through the lateral boundaries were being properly corrected within the limited area domain of the ensemble system.

At initialization time the 96-members of the ensemble system were formed by adding random, yet spatially consistent perturbations to the truth. Perturbations were drawn from the static error covariance field for the WRF-Var. Every three hours available “truth” rawinsonde observations were assimilated again, enabling the creation of an entirely new 96-member ensemble system. Perturbations drawn from the WRF-Var covariance fields were applied to the lateral boundary conditions to ensure that perturbations continued to enter the limited area domain from outside.

Initial conditions from the DA were then used to create forecasts that extended past the assimilation cycling window. Ensemble forecasts were created at 1200 UTC 23 January and 1800 UTC 23 January. Both systems were designed to end at 0000 UTC 24 January, approximately when the dense fog event began.

In order to examine how the size of the ensemble system affected the ESA, reduced-size ensemble systems were created alongside the full 96-member field. At 0000 UTC on 22 January, sub-samples with 80, 64, and 48 ensemble members were created and run separately, yet analogously to the 96-member system. These sub-systems were created by selecting the first 80, 64, and 48 ensemble members of the full 96-member ensemble system. By drawing

all ensemble systems from the same 96-member background field, we can be certain that our sensitivities are drawn from the same ensemble data system. This limits the variation in the initial conditions of the systems and provides a greater likelihood of model systems with similar parcel trajectories and therefore similar sensitivities. All four ensemble systems end at 0000 UTC on 24 January. Figure 5 represents the full DA cycle.

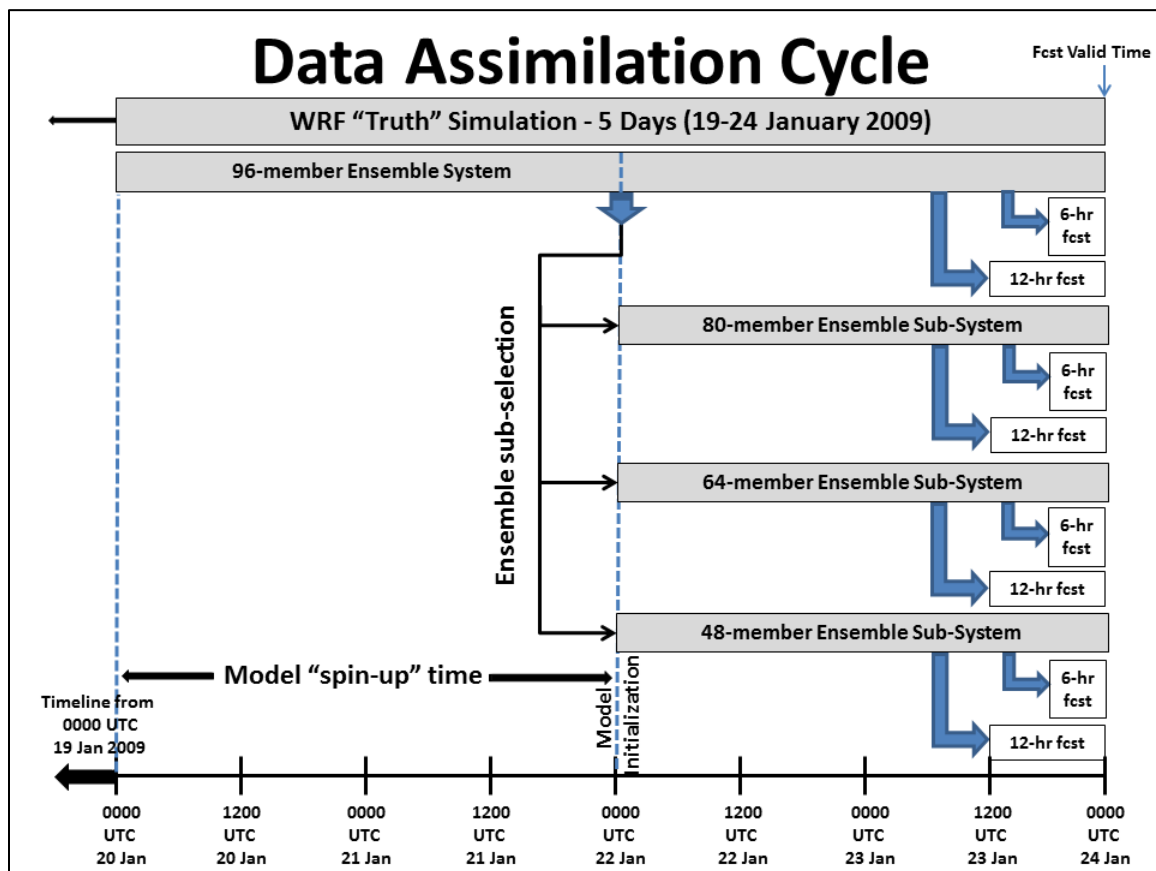


Figure 5. Data Assimilation Cycle used for this project. All forecasts are valid at 0000 UTC 24 January 2009 to coincide with the onset of the dense fog event at Salt Lake City International Airport.

### c. Covariance Localization and Covariance Inflation

Because of sampling error inherent in the ensemble system, it is necessary to implement a tool to limit the horizontal and vertical magnitude of the covariance between  $x_i$  and  $J$ . This technique is covariance localization and helps

prevent the creation of spurious covariances at long distances that come about because of the inherent model error. While this process does introduce some imbalances to the system, it is a “practical necessity for EnKF NWP applications” (Hamill 2013).

Another corrective tool implemented was covariance inflation. This technique increases the spread of the ensemble in order to negate any possible underestimation of forecast error variance that may occur because of limitations in ensemble size. This correction helps to ensure that ensemble variance is not artificially limited because of model error.

## **E. REGIONAL OVERVIEW**

### **1. Geography of Great Salt Lake Basin**

This research focuses on the Great Salt Lake Basin of Utah, with an emphasis on conditions near the Great Salt Lake (GSL) and at Salt Lake City International Airport (ICAO: KSLC). The GSL Basin is a snow-dominated hydrologic system situated in northern Utah that encompasses approximately 55,000 sq km in area. The GSL covers an average area of 4,500 sq km, though it can exhibit significant (+/- 1,300 sq km) interannual variability due to its shallow depth and dependence on hydrologic cycles. Because of its shallow depth and high salinity, water temperatures vary from subfreezing in the winter to greater than 80°F in the summer. The average elevation of the GSL is 4,202 feet above sea level and it is bounded by terrain in nearly all directions (Figure 6). To the east, and most prominently, is the Wasatch Range (Figure 6, Point 1) which runs north to south along the length of the lake and ranges in elevation from 4,200 to nearly 12,000 feet, with most crests above 10,000 feet. Across the south, west, and north edges of the GSL are a series of smaller, primarily north to south oriented mountains which serve to further bound the lake by creating a vertical barrier that inhibits interaction with the rest of the intermountain west. Within or near the southern boundaries of the GSL, these peaks include the Oquirrh Mountains (Figure 6, Point 2), which rises to 10,620 feet, Antelope Island (Figure 6, Point 3) highest elevation 6,596 feet, Stansbury Island (Figure 6, Point 4),

highest elevation 6,647 feet, and the Stansbury Mountains (Figure 6, Point 5) further to the south, which reaches an elevation of 11,035 feet at Deseret Peak. To the southwest of the GSL are the Lakeside Mountains (Figure 6, Point 6), capped by Craner Peak at 6,621 feet, while to the northwest sits the Hogup Mountains (Figure 6, Point 7), which exceeds 7,050 feet at Tangent Peak. Finally, north of the GSL lies a series of north to south ranges which extend north to Idaho, the most prominent of which are the Promontory Mountains (Figure 6, Point 8), rising over 7,300 feet.

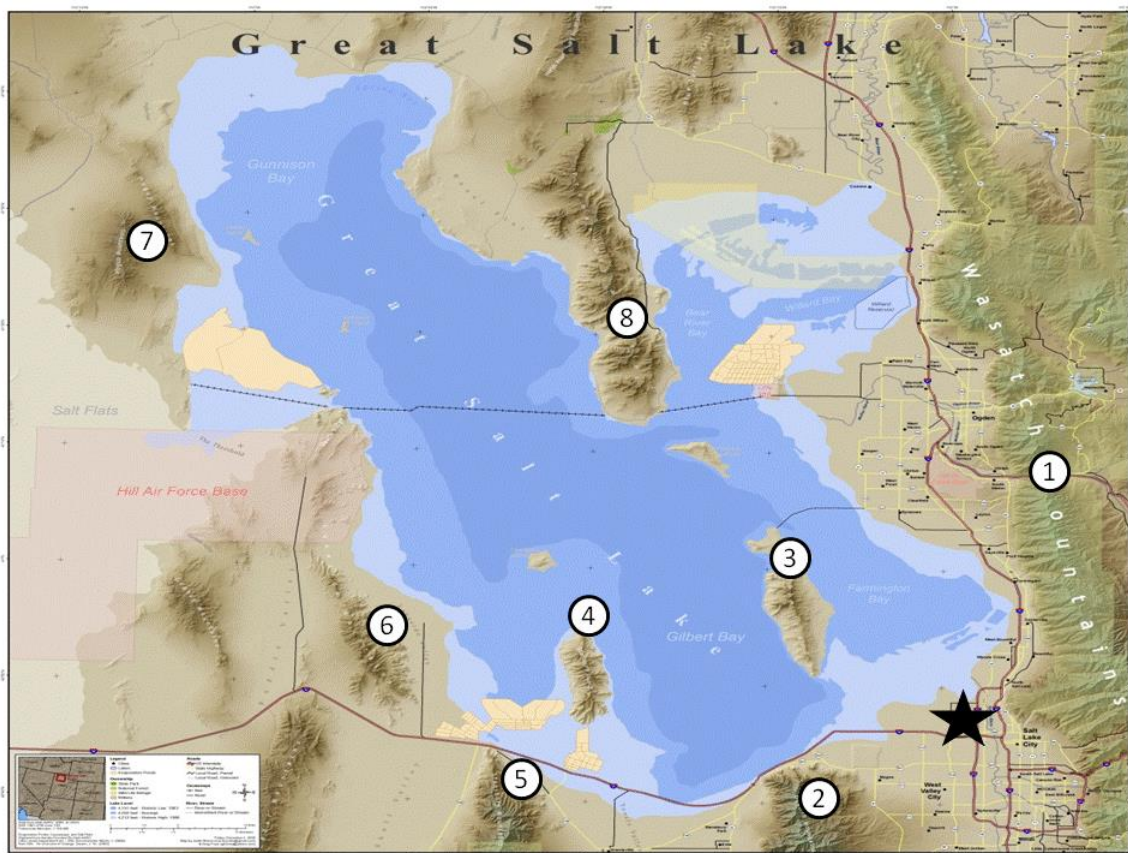


Figure 6. Map of Great Salt Lake with primary terrain features annotated.  
(After Utah Automated Geographic Resource Center, <http://gis.utah.gov/>).

The cumulative effect of these mountains is the creation of a vertical barrier in excess of 2,000 feet around the GSL that impedes interaction with the rest of the Intermountain West. The primarily north to south orientation of these orographic features tends to block zonal flow and channel meridional flow across

the GSL basin. In the fall, spring and winter, large gaps between the north to south oriented features enable the advection of cold air from southern Idaho and warm advection from points southward, while disrupting west to east oriented flows. In the winter as the lake cools, the flow-blocking provided by these mountains helps enable the buildup of a dome of cold air across the GSL basin, which plays a significant role in the lifecycle of mesoscale meteorological phenomena, including the formation of deep stable layers (DSL) as identified by Wolyn and McKee (1988).

Salt Lake City International Airport (KSLC) lies southeast of the GSL (Figure 6, black star) approximately eight miles from boundary of the lake. The airport is located four miles northwest of downtown Salt Lake City. The airfield elevation is 1,288 meters (4,227 feet) which situates KSLC 25 feet higher than the GSL, on average.

## **2. Fog at Salt Lake City International Airport**

Though the general dynamics of fog formation in valley basins is well understood, analysis of fog formation in the GSL basin is not widely available. Published papers on the subject are limited and include a study on the effect of the size of the GSL on fog formation (Hill 1988) as well as partial examination of fog formation mechanisms in Wolyn and McKee's examination of deep stable layers (Wolyn and McKee 1988). Unpublished materials are more numerous and include a study on dense fog initiation in the Salt Lake Valley by Hogan (1998) and a database of fog events by Alder, which was included in a broader climatological publication on historical weather records in Salt Lake City (Alder et al. 1998).

David Hogan's examination of 30 years' worth of Salt Lake Valley dense fog events identified the critical role that inversions played in the formation of these events. This study identified two key criteria that an inversion should exhibit to allow dense fog formation; the requirement that an inversion be relatively shallow, less than 3,700 feet in height, and an inversion have moderate

strength, exhibiting greater than 1.5°C/1000 feet lapse rate. Without meeting these criteria, the formation of dense fog at KSLC is very unlikely (Hogan 1998).

In 2004, Jonathan Slemmer, a meteorologist with the National Weather Service (NWS) Center Weather Service Unit (CWSU) in Salt Lake City, completed an unpublished study on dense fog at KSLC. The climatological database used for the study was the surface observations taken at KSLC from July 1971 through June 2001. Slemmer sought to investigate the frequency and intensity of dense fog events at the airport and what the impact of the events had on aviation. For this study Slemmer defined “dense fog” as “reported surface visibility equal to or less than one-quarter statute mile (SM) without precipitation other than snow grains”; a definition which will be maintained throughout this paper.

In the study, the author clearly defines the meteorological parameters that are typically observed during dense fog events. Three of the most unique and possibly consequential findings presented by Slemmer indicate that:

- Dense fog is primarily an early-winter event, with 77% of all occurrences observed in December and January. February accounts for 18% of all events while only 2% of events occurred in November or March, with no other months providing statistically significant occurrences. While the author does not speculate on the implication of this information, it indicates a seasonally-driven forcing mechanism that may be related to the interaction between colder winter air masses, increased frequency of frontal systems and a slowly cooling lake. It is likely that the moisture contribution to the near surface levels around the GSL decreases significantly as the lake temperature falls through the winter. In addition to the greater likelihood of ice formation as the temperatures lowers, colder water has lower vapor pressure and contributes less water to the atmosphere, lowering the likelihood of dense fog formation as the winter goes on.
- Winds from the west through northeast (260°- 040° in degrees true) and southeast (130°-190° in degrees true) provide two distinct maxima for the observed wind direction during dense fog events (see Figure 7). While the NE-oriented maximum is to be expected as the GSL can be found across this azimuth range and winds from this direction are expected to be moister, the SE-oriented maximum may be related to cold moist air draining down the Jordan River

Valley from Utah Lake to the southeast. Another possible explanation for the southeasterly maxima, and one believed to be occurring during the event that is the focus of this study, is that the southeasterly flow is related to warm air advection and strengthening or creation of an inversion over KSLC and the persistent cold dome over the GSL.

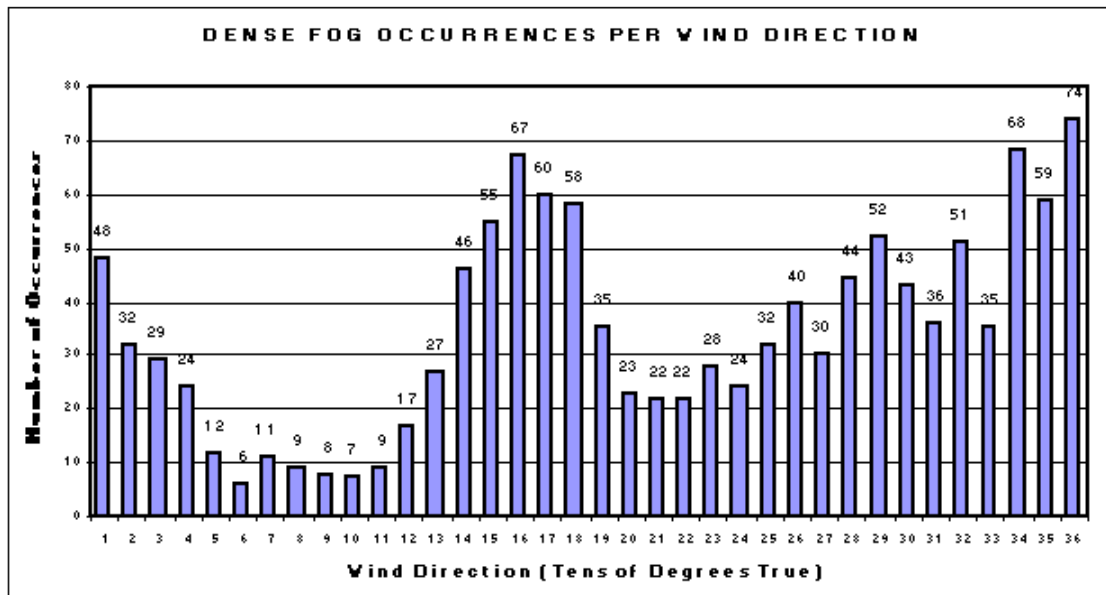


Figure 7. Dense fog occurrences at Salt Lake City International Airport by wind direction. (From Slemmer 2004)

- Less than 6% of all dense fog cases occurred with the temperature above freezing. This is important to note because during the 24 January, 2009 fog event at KSLC the temperature remained above freezing for the duration. This implies that this case is atypical in this regard and should be considered in the future if other dense fog events are to be evaluated through ESA.

In an examination of dense fog events that occurred in December and January during the winter of 2001 and 2002, Slemmer categorized the dense fog events into three distinct event types: a prolonged inversion case; precipitation falling into a weakened inversion and shallow cold pool cases; and shallow cold pool advecting from GSL cases. It is believed that the event that is the focus of this study is defined by the both the second and third event type.



One additional phenomenon described by the author is how shallow cold pools over the GSL may “slosh” back and forth in the valley, leading to possible repeating progression and retreat of cold air masses over KSLC. Though it is not examined in this study, because of the intensity and duration of the dense fog event of 24 January, 2009, it is not believed that this type of phenomenon is impacting the mesoscale circulation of this study.

## **F. ATMOSPHERIC CHARACTERIZATION**

### **1. Synoptic Analysis**

The week leading up to the dense fog event at KSLC was characterized by an “omega” blocking pattern with strong ridging over the western U.S. and an upper-level ridge axis oriented meridionally over the Western Rockies. In the Salt Lake City area, this meant clear cold nights with lows near 20°F and sunny days with highs in the mid-30s°F. Visibility at KSLC remained relatively favorable during this period with haze and mist reducing visibility to between 3 SM and 5 SM at nearly all hours, as might be expected with a stagnant air mass in an intermountain lake basin such as the Great Salt Lake. One period of significantly reduced visibility did occur on the night of 20 January, as visibility at KSLC fluctuated from 1/4 SM to 3 SM in freezing fog and mist, as a shallow fog bank vacillated over the airfield. The shallow and localized nature of this feature can be implied through observations at Hill Air Force Base (ICAO: KHIF) and Ogden-Hinckley Field (ICAO: KOGD). These locations situated 25-30 SM north of KSLC and 200-500 feet higher in elevation, remained unrestricted in visibility throughout the same time period, though both are nearly the same distance from the boundary of the GSL. This event is interesting to note because it serves as the only time period, excepting the later rain and dense fog event which is the focus of this study, when visibility was significantly reduced at KSLC during the seven days that the western U.S. was under the influence of this regime.

Beginning on 20 January and continuing through 23 January, the strong ridging across the Rockies began to slowly weaken as the upper-level wave

pattern over the U.S. transitioned from highly meridional to weakly meridional. As this transition occurred, the ridge over western U.S. maintained its north-south orientation while slowly decreasing in amplitude (see Figure 8).

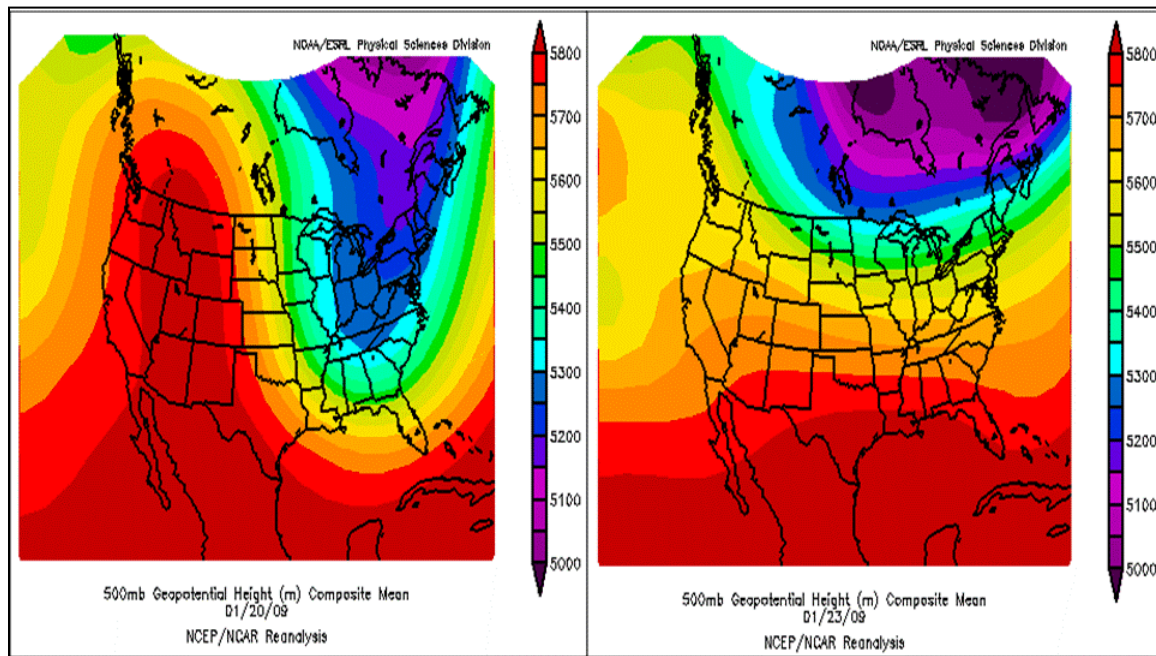


Figure 8. 500 hPa Geopotential Height (m) Composite Mean change from 20 January 2009 to 23 January 2009. (From NOAA/ESRL Physical Sciences Division: <http://www.esrl.noaa.gov/psd/>)

Further evidence of the weakening ridge can be found in the METAR observations across northern Utah from 21-23 January which indicate increasing upper and mid-level cloud cover and lowering altimeters. Soundings launched from KSLC at this time show decreasing static stability aloft and increasing moisture at nearly all vertical levels, though a strong low-level inversion remains present throughout.

By 23 January, the poleward extent of the ridge, and its influence over the western-central U.S., has weakened sufficiently to allow a mid-level system to push across the Northern Rockies. As this system moved eastward, it was led by a surface cold front that pressed down the east side of the Rockies and into the Great Plains early on 23 January. Behind this cold front a strong surface anticyclone amplified into the Great Plains during the day on 23 January, with

1047 hPa central pressure estimated over southern Alberta, and surface pressure values of 1040 hPa reaching into northwest South Dakota (see Figure 9). At the same time that the cold front progressed southward across the northern Great Plains, a surface low with attendant cold front entered the southwest U.S., pushing into southern California. This disturbance was relatively weak (lowest central pressure recorded as 1014 hPa at 1200 UTC on 23 January) and its eastward progression was stopped by ridging still present over the Rockies.

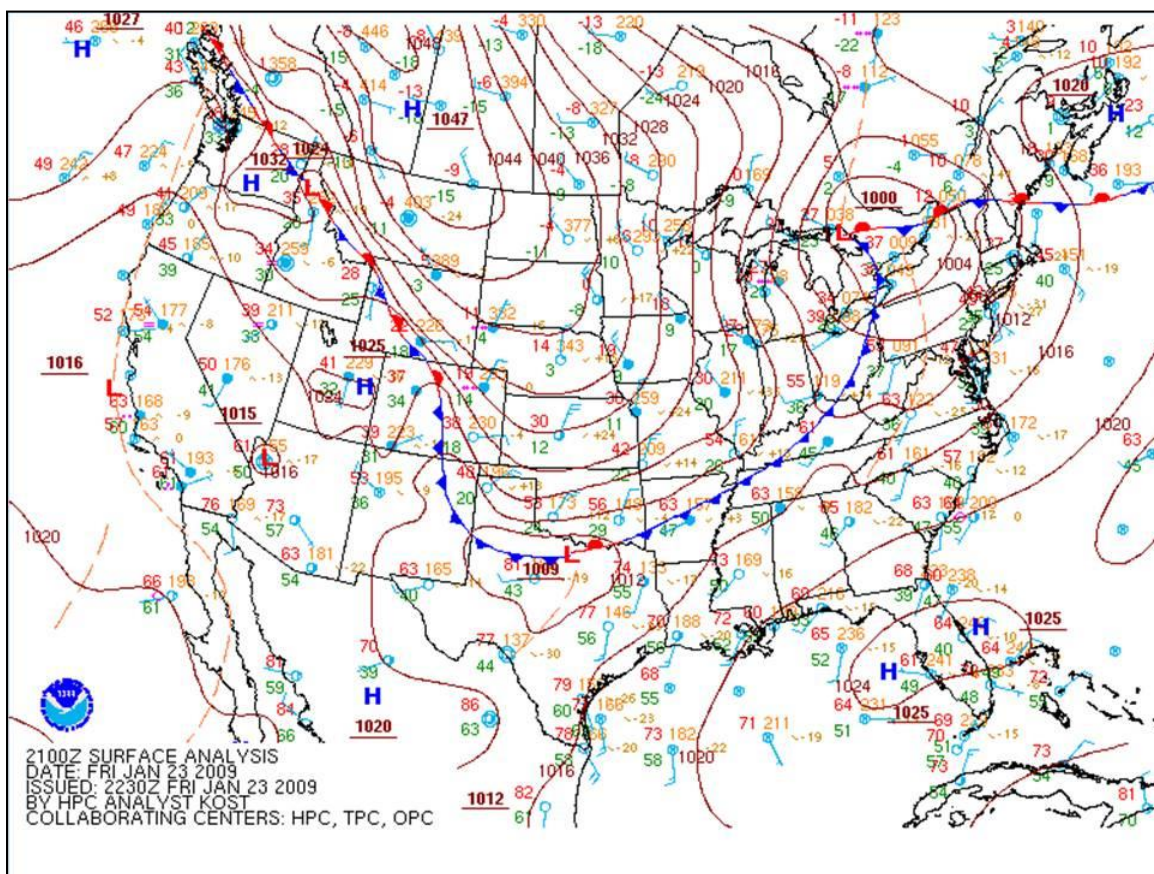


Figure 9. Hydrometeorological Prediction Center Surface Analysis from 2100 UTC on 23 January, 2009.  
(From <http://www.hpc.ncep.noaa.gov/>)

The combined effect of these two features was to force a warm, southerly flow northward across the southern and central Intermountain West during the

afternoon hours of 23 January, 2009. Note in Figure 9, the southerly winds recorded at stations in Arizona, Nevada, and Utah, and the generally warm air in the region with temperature readings of 73°F in Phoenix, 61°F in Las Vegas, and 50°F in southwestern Nevada. This push of warm air over the cold continental air in place in northern Utah was essential in developing conditions ideal for the dense fog event at KSLC early on 24 January.

## **2. Precursor Rain Event**

On 23 January, the atmosphere in northern Utah had become sufficiently destabilized with the passage of the mid-level disturbance (Figure 10) to support vertical motion yielding precipitation in the form of light rain at KSLC, KHIF, KOGD, and as far south as Provo (ICAO: KPVU).

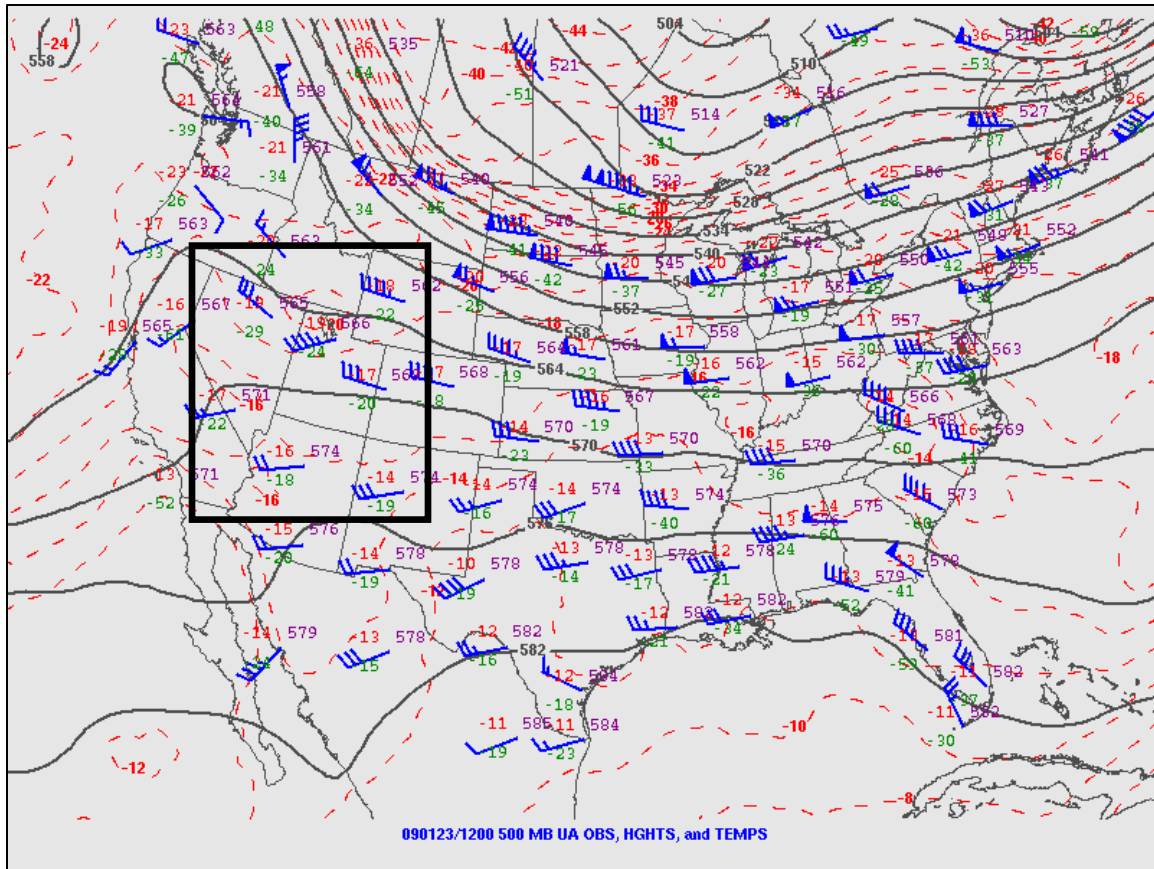


Figure 10. Hydrometeorological Prediction Center 500 hPa upper-air analysis containing observations, heights, and temperatures for 1200 UTC 23 January 2009. The black box indicates the positioning of the weak disturbance moving through northern Utah on 23 January 2009.

On 23 January, Salt Lake City Airport recorded 0.11" of rain from 0600 UTC to 1200 UTC and later recorded 0.10" of rain between 1600 UTC and 2000 UTC. During the initial rainfall period, surface winds at all of the local stations were generally from the north, though winds at KSLC exhibited significant variability, with wind source alternating 90-180 degrees every other hour, while remaining below 10kts. Winds during the second rain event are observed to be predominantly from the south, though significant variability is still observed. Also important to note is the steady increase in temperature on 23 January at KSLC, as temperatures rose from 01°C at 1500 UTC to 08°C at 2300 UTC, while light rain fell frequently. Though some variability in wind direction should be expected in a geographically complex area, the significant rise in temperatures at KSLC



and high variability in wind direction suggest that a warm frontal boundary had formed in the southeast GSL basin. This boundary developed as warm air from southern Utah met the colder air mass over the GSL Basin and the influence of the mid-level disturbance. Where these two air masses met is where vertical motion was initiated as the warm air rose isentropically up and over the colder dense lake air (see Figure 11).

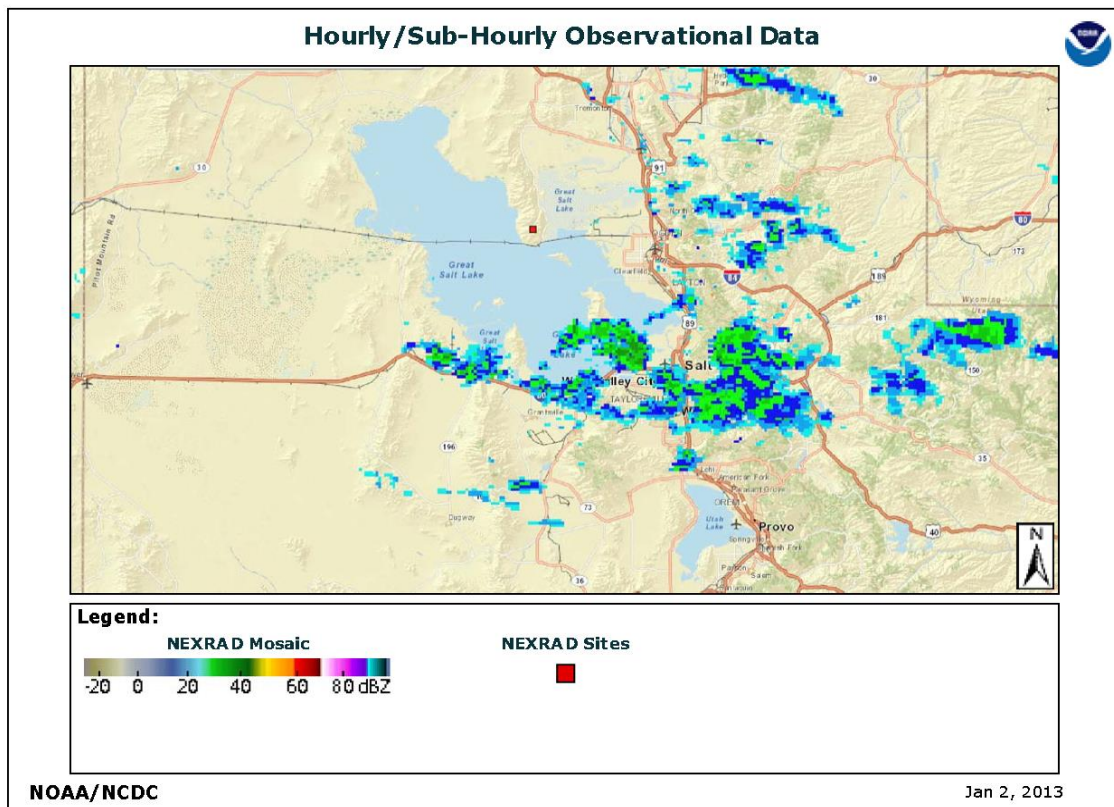


Figure 11. Radar imagery over Salt Lake Basin from 1800 UTC 23 January 2009. (From National Climatic Data Center <http://www.ncdc.noaa.gov/radar-data>)

The variability in the surface observations suggest that these air masses converged over the southern GSL basin for several hours midday on 23 January, before the warm front finally displaced the cold dome over KSLC between 1800 UTC and 1900 UTC. After the warm front moved past KSLC temperatures rose quickly, precipitation ended, and visibility increased to 3 SM. The 1200 UTC 23 January KSLC skew-T (Figure 12) indicates a strong low-level

inversion still present, with southerly winds above the inversion, veering to westerly at 750 hPa. Examination of the 0000 UTC 24 January skew-T (Figure 13) shows that enough destabilization had occurred with the passage of the mid-level disturbance to mix out the low-level inversion that had been in place since 17 January. Note that the low level winds at 0000 UTC have become northerly, which coincides with the onset of the dense fog event.

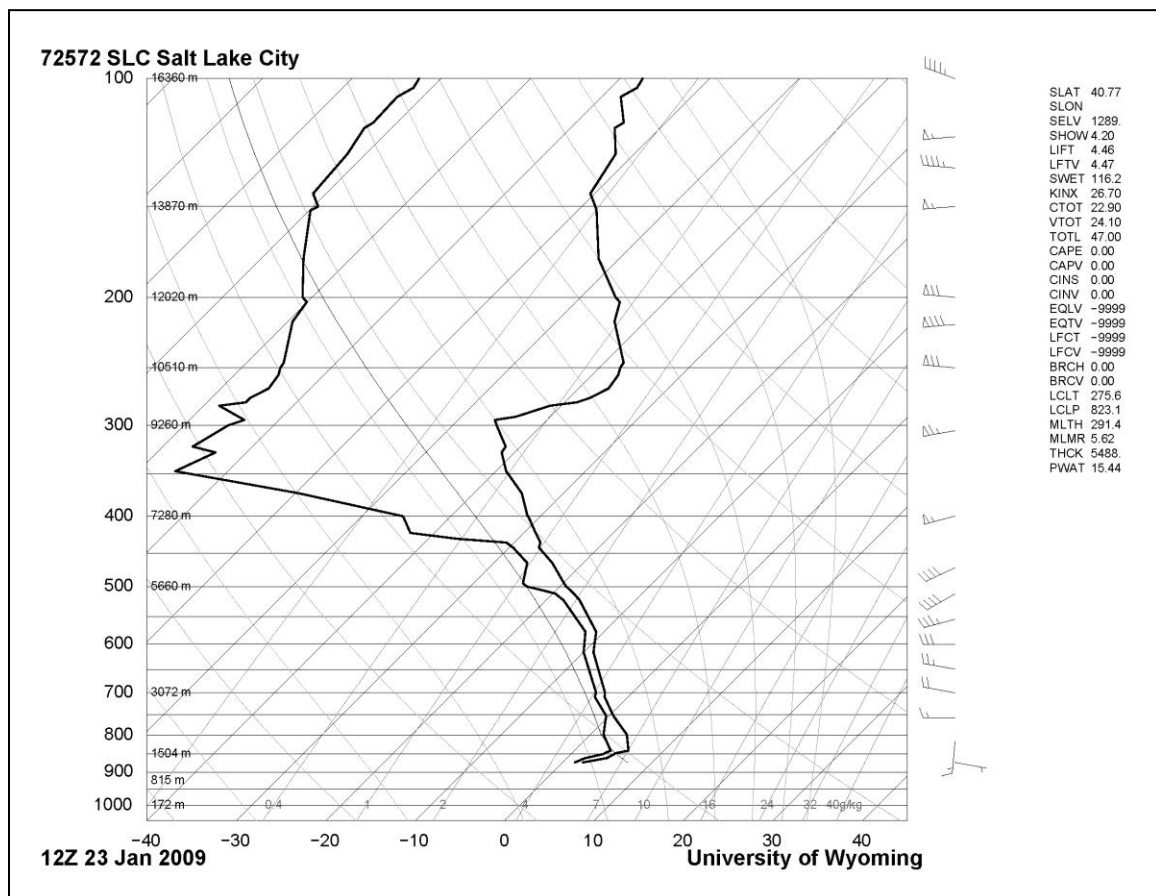


Figure 12. 1200 UTC 23 January 2009 sounding from KSLC indicating presence of strong low-level inversion.(From University of Wyoming, <http://weather.uwyo.edu/upperair/sounding.html>)

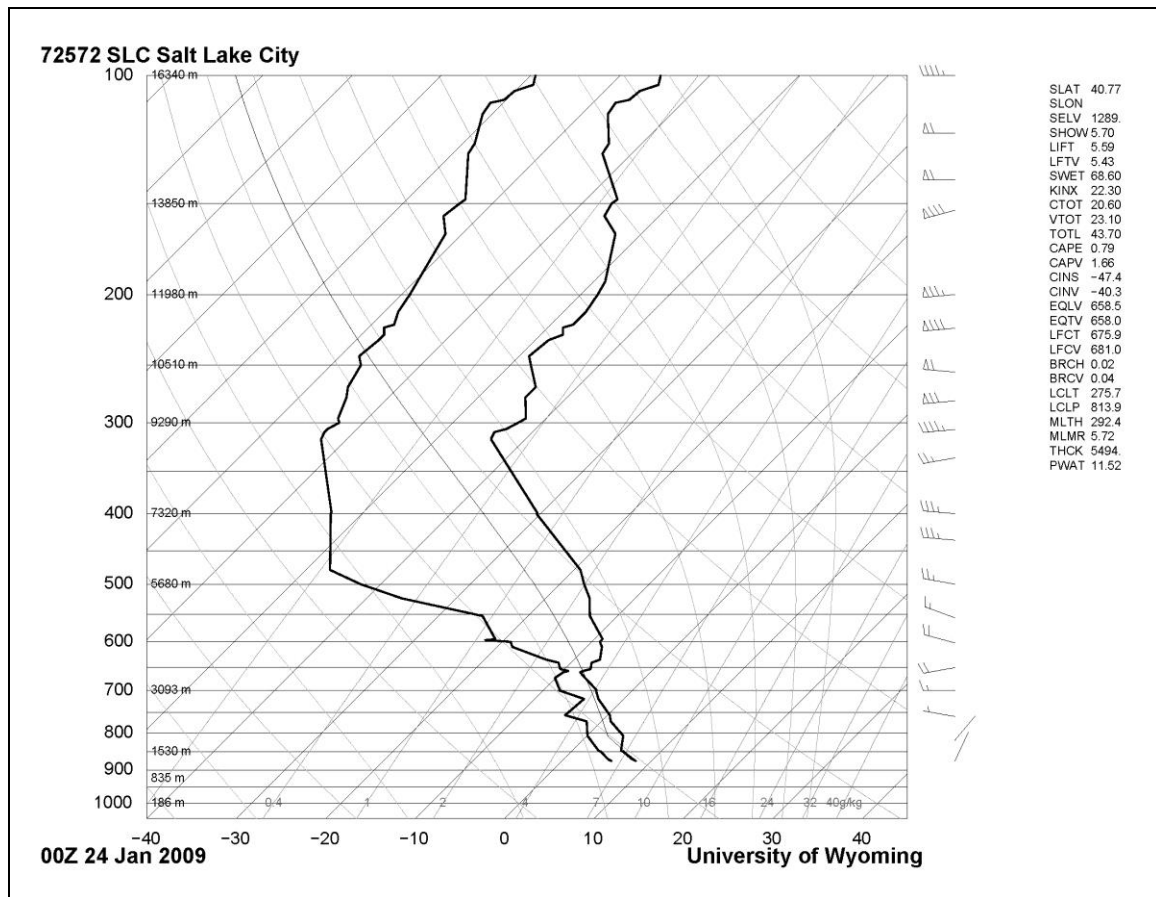


Figure 13. 0000 UTC 24 January 2009 sounding from KSLC indicating that the low-level inversion has been ameliorated. (From University of Wyoming, <http://weather.uwyo.edu/upperair/sounding.html>)

By 1200 UTC on 24 January (Figure 14), the low-level inversion has reformed due primarily to a decrease in temperatures at the near-surface level, as temperatures at the top of the boundary layer remained unchanged. With the inversion reformed, southerly and southeasterly flow returned as the dense fog event concluded.



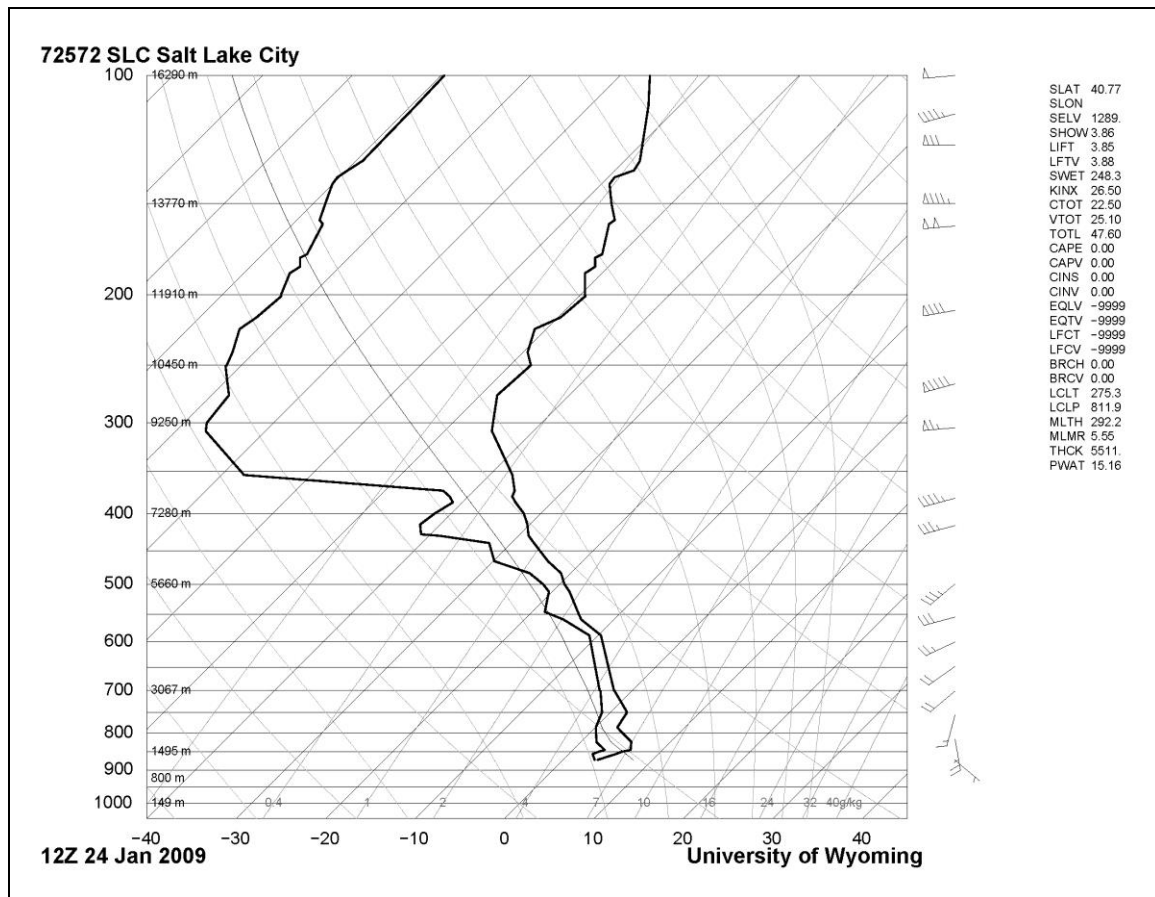


Figure 14. 1200 UTC 24 January 2009 sounding from KSLC indicating the reformation of the low-level inversion.(From University of Wyoming, <http://weather.uwyo.edu/upperair/sounding.html>)

Though no skew-T's are available directly over the lake, it is hypothesized that that an inversion remained in place through the duration of this event with surface water temperatures across the lake in the 30s°F (Adams), and due to the relative weakness of the mid-level disturbance. Though the low-level inversion at KSLC mixed out by 0000 UTC on 24 January, the strength of the inversion over the lake was likely enhanced after the warm southerly winds met the boundary with low-level cold pool over the GSL. The isentropic uplift over the cold dome that ensued strengthened the inversion over the lake and forced air parcels up and over the inversion, inducing precipitation which fell through the inversion toward the lake surface, fully saturating an already moist, cool environment. Adding to the low level moisture across the lake was widespread rainfall that fell across the GSL earlier in the day during the passage of the mid-level disturbance

(not shown). This type of fog formation was identified by Hogan as a rare but definable case when light precipitation falling into an already moist stable layer causes the formation of dense fog (Hogan 1988). As the warm air advection stopped with the weakening low to the southwest, the cold, moist, and dense air over the GSL flows southward enveloping the southern GSL basin in dense fog.

### **3. Dense Fog Event**

At 2243 UTC on 23 January, winds at KSLC were calm, visibility was 3 SM in haze, and the temperature and dew point were 08°C and 05°C respectively. Within one hour, conditions changed considerably as winds became northerly at 06 kts with visibility lowering to 1/16 SM in dense fog and temperature falling to 04°C at 2342 UTC. Sunset locally on 23 January, 2009 was at 0033 UTC (24 January) or 1733 MST (23 January), and occurred 1-2 hours after the onset of the dense fog event. Though diurnal effects may have partially contributed to the development of this event, cloud cover over KSLC remained broken to overcast throughout the day on 23 January limiting insolation, so it is unlikely that the daytime heating played a substantial role in the formation of this event. The average high temperature at KSLC for 23 January is 38°F, while the temperature recorded this date was 48°F, indicating substantial anomalous warming. Dense fog ( $\leq 1/16$  SM or less) and light ( $<06$  kts) west-to-northwesterly or calm winds remained predominant at KSLC for 6 hours following onset of the event, through 05 UTC on 24 January. The temperature at KSLC dropped to 01°C at 0153 UTC on 24 January. At 0553 UTC on 24 January (2253 MST, 23 January), the first sign of a break in the event is observed as winds shifted to southeast while remaining light ( $\leq 5$  kts) and visibility improved slightly to 1/8 SM. These conditions prevailed until 1044 UTC when the southeasterly flow strengthened to 7 kts and visibility improved to 3 SM. Within a few minutes (1053 UTC) the southeasterly winds were measured at 8 kts and visibility rose to 5 SM as the dense fog event rapidly eroded. The total time spent with visibility at or near 1/8 SM is approximately 10 hours.

#### **4. Relation of Physical Interpretation to ESA**

The importance of the cold dome over the GSL in the creation and maintenance of low level inversions is believed to be a primary factor in the development of fog at Salt Lake City International Airport for this event. It is following the breakup and subsequent reforming of the inversion that the cold moist air over the lake is able to flow southward over KSLC. It is believed that the breakup of the inversion is enabled by the vertical forcing associated with of the mid-level trough and the advancing warm front.

The mesoscale system that develops within the synoptic forcing provides an initial predictor as to which meteorological variables, and which locations, may be important in the formation of dense fog at KSLC. The physical interpretation described in the atmospheric characterization identify the potential role that the surface and planetary boundary layer (PBL) temperature, wind, and relative humidity may offer as useful variables in the development of a complete ESA for this region.

#### **G. PARAMETERS**

Previous work by Chilcoat (2012) identified the need for careful selection of both analysis state ( $x$ ) and forecast ( $J$ ) parameter to determine the most responsive and indicative sensitivities. Chilcoat found the  $u$  and  $v$ -wind components on the lowest model layer (~20 meters) to be the most reliable analysis state parameter for predicting robust sensitivities. For forecast parameter, Chilcoat averaged ensemble average water vapor mixing ratio,  $q_v$ , in a 2x2 (8-km x 8-km) square, hereafter referred to as a  $J$ -box, located over KSLC and summed over the first two model levels (~58 meters).

##### **1. Type Selected For Study**

This study instead found the most robust sensitivities with temperature as the analysis state parameter. While  $u$  and  $v$  component winds did exhibit sensitivity in our forecast system, the magnitude was ~25% of that found with

temperature. Other state parameters were also considered, including  $q_v$  and total dry air mass in the column ( $\mu$ ). Neither parameter provided a reliable, robust, or coherent sensitivity relationship in our forecast system.

## **2. Configuration of Parameters**

Alterations were also necessary to the size of the  $J$ -box centered over the airport, though  $q_v$  was remained the forecast parameter. Due to the implementation of the linearity filtering described in section 3.B., the 2x2  $J$ -box summed over the lowest two model levels used by Chilcoat no longer provided a reliable sensitivity response. Sensitivities using Chilcoat's configuration continued to provide a reliable sensitivity response at the 6-hour forecast time, however, 12-hour forecasts using this configuration failed the Gaussianity testing. This failure was determined by Lilliefors test results indicating that the ensemble distribution of forecasted  $q_v$  values in the area enclosed by the  $J$ -box was non-Gaussian.

In order to ensure Gaussianity of forecast parameter and continuity between forecast lead times, it was necessary to alter the size and position of the  $J$ -box. Multiple combinations of  $J$ -box sizing were attempted, including reduction of the  $J$ -box to a single point closest to KSLC, as well as expansion to horizontal grid spacing of 3x3 and 4x4, with variations of model levels between level 1, level 2, and the summation of these levels. It was also theorized that expansion of the  $J$ -box toward the expected  $q_v$  source (the GSL) would provide a more reliable response. Due to the nearly equal proximity of the GSL to the north and west, and also the variation of the low level winds leading up to the dense fog event, it was speculated that expansion of the  $J$ -box outward in all directions would provide the most representative data field for low level  $q_v$  around the airport. . After trial and error, the smallest, yet still Gaussian,  $J$ -box that could be determined to be valid at the 6-hour and 12-hour forecast was a 3x3 box (12 km x 12 km) centered nearly directly over KSLC, and summed over the first two model levels. The selection of a larger  $J$ -box than was previously used by

Chilcoat is should improve ESA findings as the area-averaging of  $J$  provides more robust results by averaging out some of the sample error and noise associated with the distributions (G. J. Hakim 2013, personal communication).

Though the specific dimensions of Chilcoat's  $J$ -box were not retained for this study, this does not invalidate the results of the previous work. Linearity testing conducted by Chilcoat (2012, section 4.D.) determined that the sensitivity results he achieved were linear. This allows the conclusion to be drawn that the ensemble distribution of  $x$  and  $J$  he selected were approximately Gaussian. The Gaussianity testing in this study provides an a priori means of ensuring that observed and forecast parameters are drawn from normal distributions, which enables implementation of ESA with greater certainty.

To ensure that  $x$  was also drawn from a normal distribution, Lilliefors testing was also applied to the ensemble distribution of temperature at the most sensitive grid point ( $Y = 52$ ,  $X = 121$ ) in the innermost domain. These results (not shown) indicated that analysis values for the 1800 UTC 23 January 2009 ensemble system (6-hour forecast) were Gaussian. The results of testing for the 1200 UTC 23 January ensemble system (12-hour forecast) were mixed. While Gaussianity tests at the most sensitive point were weakly non-Gaussian, tests at several adjacent sensitive grid points ( $Y=51$ ,  $X=121$  and  $Y=53$ ,  $X=120$ ) with similar levels of sensitivity indicated entirely Gaussian distributions of temperature (see figure 15). This finding implies that ensemble distribution of temperature at the concentrated area of greatest sensitivity is effectively normal.

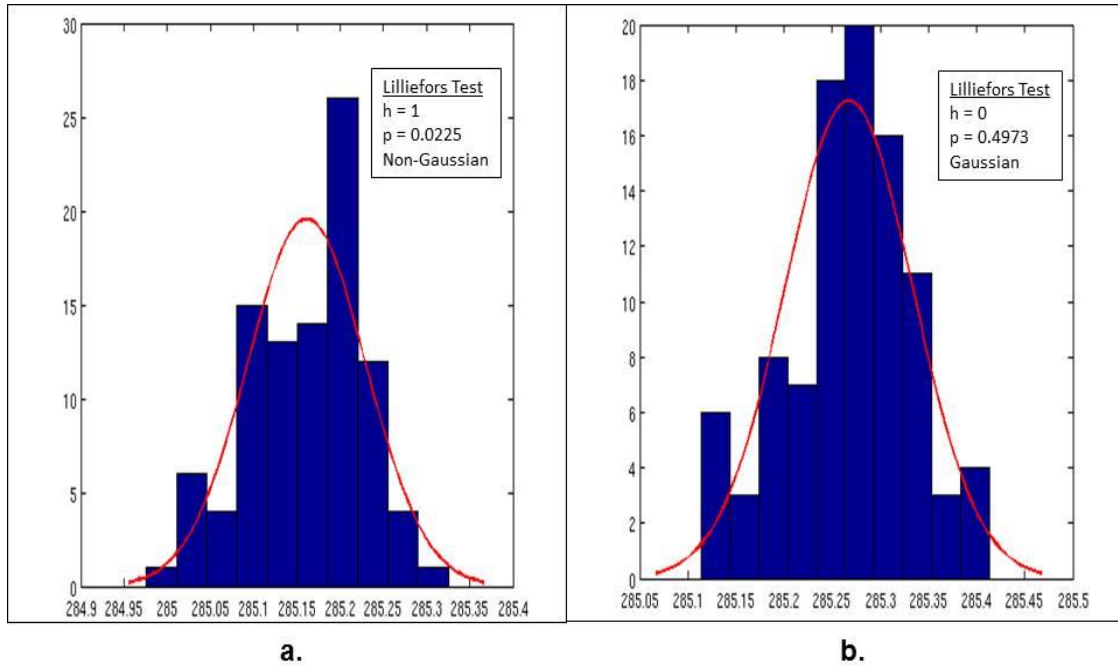


Figure 15. Histograms of ensemble analysis potential temperature ( $\theta$ ) for the lowest model level at 1200 UTC 23 January 2009 for (a.) the most sensitive grid point in the innermost domain, ( $Y=52, X=121$ ) and (b.) an adjacent grid point ( $Y=51, X=121$ ). The red line indicates the normal distribution while the blue bars indicate the probability density function of  $\theta$  at each grid point.

The conclusion that can be drawn from these tests is that ensemble distribution of the forecast parameter ( $q_v$ ) at KSLC is Gaussian, while the analysis state variable ( $T$ ) at the most sensitive grid point, is Gaussian, or that it represents the normal distribution with sufficient closeness to meet the required assumptions necessary to perform the linear regression that forms the basis of ESA.

## IV. RESULTS

### A. WRF ENSEMBLE PREDICTIONS

Though the purpose of this ensemble study was not to quantify accuracy of the WRF mesoscale ensemble system, the qualitative performance of the system is of great relevance. To accurately identify the statistical and dynamic relationships of this system, it is necessary for the ensemble system used to define the system to have skill. This section will discuss the performance of the 96-member WRF-ARW model used for this experiment.

#### 1. Moisture in GSL Basin

Accuracy of the forecast system was estimated using predictions for a grid point representing KSLC ( $X=137$ ,  $Y=88$ ). This grid point lies approximately 0.6 miles (1.0 kilometer) northeast of the airport and is most representative of conditions at KSLC.

Figure 16 shows EM  $q_v$  (in  $\text{kg kg}^{-1}$ ) at  $\eta_{-1}$  (the lowest model level) in 3-hour intervals, clockwise from top left, from 1800 UTC 23 January to 0600 UTC 24 January. This figure represents the 96-member ensemble initialized at 1800 UTC 23 January. The image shows the strong concentration of water vapor in the lowest model level, represented by warmer colors, over KSLC at 1800 UTC 23 January. It appears also at this time that stronger concentrations of water vapor extend beyond the boundary of the GSL, nearly overcoming KSLC. At 2100 UTC, the higher water vapor concentrations have expanded further from GSL, clearly encompassing KSLC. The densest water vapor concentrations push outward from the GSL, filling the valleys south of lake 10-20 kilometers inland. Expansion of the higher water vapor concentrations continues through 0000 UTC on 24 January.

Between 0000 UTC and 0300 UTC 24 January, the horizontal extent of the strongest concentrations of water vapor begins to recede, indicating drying across GSL basin. The amelioration of the dense water vapor values intensifies

between 0300 UTC and 0600 UTC 24 January. It appears that KSLC is surrounded by a significant dry slot by 0600 UTC 24 January, indicating that the dense fog event has ended.

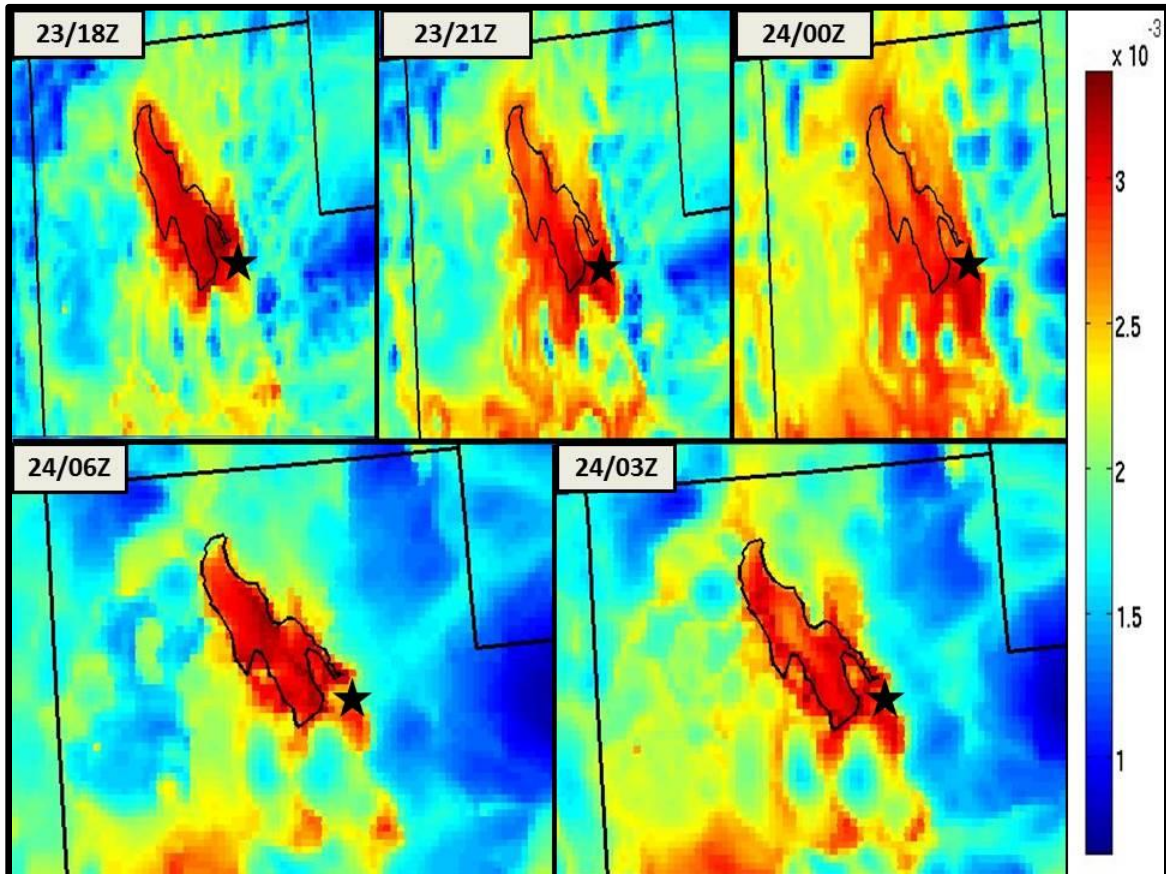


Figure 16. Ensemble mean  $q_v$  (in  $\text{kg kg}^{-1}$ ) at  $\eta_{-1}$  in 3-hour intervals, clockwise from top left, from 1800 UTC 23 January to 0600 UTC 24 January. UTC annotated as Z. 96-member ensemble initialized at 1800 UTC 23 January. Approximate position of KSLC is represented by black star. Warm colors represent stronger concentration of water vapor.

## 2. Moisture at KSLC

Moisture at KSLC is measured using an Automated Surface Observing System (ASOS) at a height of approximately 2 meters. To compare the actual observed amount of water vapor at KSLC versus the model forecast value, calculations were made to convert the observed measurements of temperature,



dew point and pressure into water vapor mixing ratio, in units of  $\text{kg kg}^{-1}$ . Water vapor mixing ratio is one of the five primary output fields produced by WRF-ARW used to track the different state parameters of water.

Figure 17 shows the forecasted 20-meter and 2-meter  $q_v$  at KSLC versus observed  $q_v$  at KSLC. The forecast values represent the 12-hour ensemble mean (EM) forecast values from the ensemble that was initialized at 1800 UTC 23 January. Forecasts from this system end at 0600 UTC on 24 January 2009. Both 20-meter and 2-meter forecast  $q_v$  were plotted to show low-level moisture continuity at near-surface levels. The figure indicates that at 1800 UTC 23 January, the ensemble system is already nearing its 12-hour maximum in water vapor mixing ratio concentration. Both the 2-meter and 20-meter water vapor levels increase until 2100 UTC 23 January, when both reach maximum levels. These maximum values are maintained until 0300 UTC on 24 January when the water vapor levels begin to decrease.

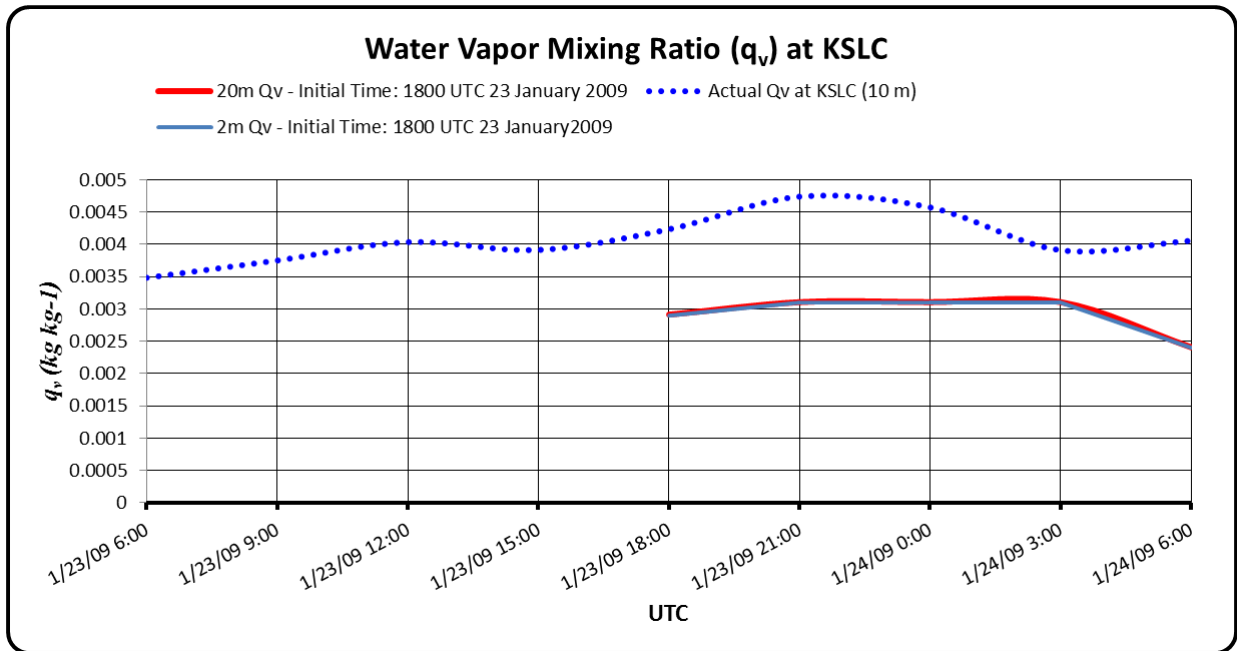


Figure 17. Ensemble mean forecast 20-meter and 2-meter  $q_v$  at KSLC versus observed  $q_v$  at KSLC. The red solid line represents 20-meter  $q_v$  for the forecast initialized at 1800 UTC 23 January while blue solid line represents 2-meter  $q_v$  from the same initialization. The  $q_v$  recorded at the airport is represented by the blue dashed line. Both forecasts end at 0600 UTC 24 January.

The values presented in Figure 17 show a marked difference in both magnitude and timing between the ensemble forecast and the observed values. Though it would be preferable to have the magnitude of the forecast values more closely represent the actual observations, the general agreement between the two (both indicating high levels of water vapor) is encouraging. Observed water vapor mixing ratios during the event fluctuated significantly from  $3.91 \times 10^{-3} \text{ kg kg}^{-1}$  to  $4.74 \times 10^{-3} \text{ kg kg}^{-1}$ . Water vapor remained high even as the dense fog lifted. Interestingly, water vapor mixing ratios remained high at  $4.42 \times 10^{-3} \text{ kg kg}^{-1}$  at 1200 UTC 24 January, even as surface visibility had increased to 7 SM. In addition, light some rain was reported as the fog lifted.

More important than the magnitude difference in the water vapor mixing ratio is the timing of the increases and decreases. The trend represented in Figure 17 shows a notable decrease in forecast value of  $q_v$  between 0300 UTC

and 0600 UTC 24 January. This can be interpreted as the end of the dense fog event at KSLC. Observations show that the dense fog did not lift until 0900 UTC 24 January, which means that the forecast is 3-6 hours early in its dissipation.

Though forecast concentration of  $q_v$ , and exact timing of its dissipation are not entirely well-represented, Figures 16 and 17 do show agreement in meso- and local-scale of the process of early dissipation of the dense fog. Chilcoat (2012) found similar results in his study and his conclusion that the timing of the event was not critical to the effectiveness of the ESA will be echoed here. The important characteristics of the forecast system are that it adequately predicts the presence of high levels of moisture across the GSL Basin and at KSLC, and that it faithfully represents the dissipation of the fog event, both of which are evident in this study.

## **B. QUANTITATIVE RESULTS**

ESA was conducted using the methodologies outlined in section III. The linearity (Lilliefors) testing, ESA calculation and statistical sampling error corrections were performed in order, with results defined below. Temperature was chosen as the initial state variable ( $x_i$ ) and water vapor mixing ratio,  $q_v$ , selected as the forecast parameter ( $J$ ). In this analysis, temperature,  $T$  (K) is determined at the analysis lowest eta-level (approximately 25 m AGL) while water vapor mixing ratio,  $q_v$  ( $\text{kg kg}^{-1}$ ) is a summation of the lowest two model levels (approximately 60 m AGL) in the area of the 12-km x 12-km  $J$ -box surrounding KSLC defined in section III.G.

Sensitivity results ( $dJ/dx_i$ ) quantify, in  $\text{kg kg}^{-1} \text{K}^{-1}$ , how changes in  $J$  relate to changes in  $x_i$ . Positive  $dJ/dx_i$  means that  $J$  increases with an increase in  $x_i$ , and  $J$  decreases with a decrease in  $x_i$ . Negative  $dJ/dx_i$  means that  $J$  increases with a decrease in  $x_i$  and vice versa. In this study we will focus on positive change in  $dJ/dx_i$ , as this study seeks to understand how state variable temperature relates to dense fog formation at a later time.

The results described in this section are based on a 96-member ensemble system, though experiments involving varying sizes of ensemble configurations were performed and will be discussed later. Experiments were conducted using both 6-hour forecast systems (initialized 1800 UTC, 23 January 2009) and 12-hour forecast systems (initialized 1200 UTC, 23 January 2009). White space in Figures 18 and 21 indicate where data has been masked at the 95% confidence interval. The star next to J indicates the approximate location of the Salt Lake City International Airport.

### **1. ESA (6 hour)**

Results from the 6-hour ESA are displayed in Figure 18. Region 1, which lies approximately 150km south/southwest of the GSL, indicates the most positive sensitivity region within the innermost domain. Sensitivity in this area ranges from  $4.433 \times 10^{-4} \text{ kg kg}^{-1} \text{ K}^{-1}$  to  $6.615 \times 10^{-4} \text{ kg kg}^{-1} \text{ K}^{-1}$ . At the most sensitive grid point (39.5072N 112.9197W) a  $\pm 0.0516 \text{ K}$  ( $1\sigma_T$ ) change in temperature at the lowest model level will lead to an equivalent  $\pm 1.015 \times 10^{-4} \text{ kg kg}^{-1}$  ( $1\sigma_{q_v}$ ) change in the 6-hour  $q_v$  at KSLC. For comparison, it is noted that this value approximates the 2m and 20m ensemble mean forecast variation in  $q_v$  over the same time period (see Figure 17).

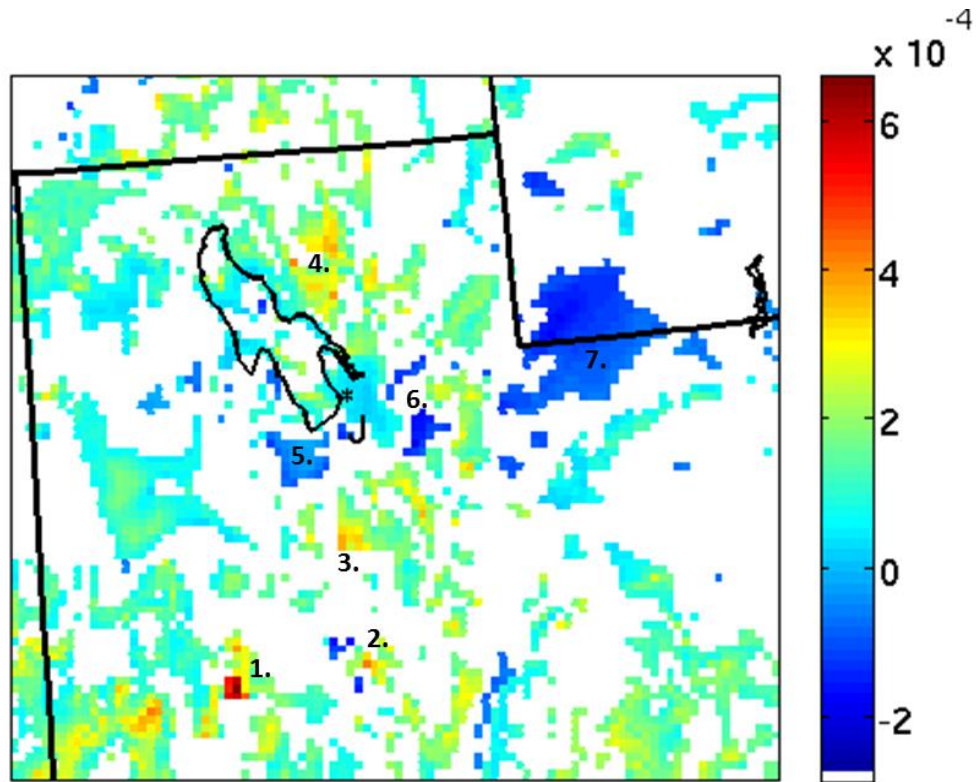


Figure 18. Sensitivities ( $dJ/dx_i$ ) using 1800 UTC 23 January analysis potential temperature (in K) as  $x_i$ , and forecasted  $q_v$  (in  $\text{kg kg}^{-1}$ ) as  $J$ , valid at 0000 UTC 24 January. Units are  $\text{kg kg}^{-1} \text{K}^{-1}$

Other strong positive sensitivity responses appear in Figure 18 across the Central Utah Desert Ranges, indicated at Region 2 and Region 3. The geographical commonality between these three regions is that they each are located near elevated terrain features that have, at least partially, an east-to-west orientation (Figure 19). In addition, these features are positioned where a strong plume of warm air pushes northward through the Central Utah Desert on 23 January (see Figure 20).

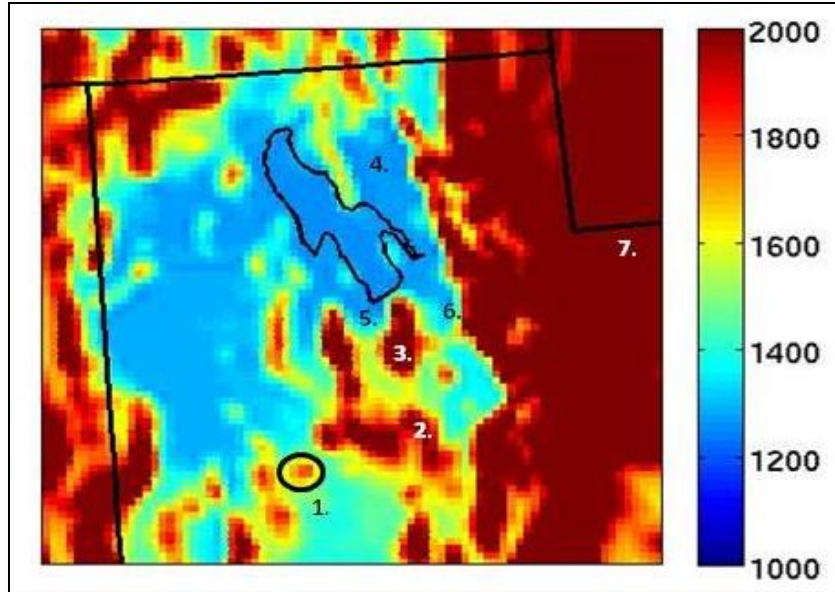


Figure 19. WRF terrain map indicating elevations between 1000m and 2000m. The black circle (#1) identifies the elevated terrain near the grid point where the strongest 6-hour ESA sensitivity response is located. Other numbers (#2-7) indicate other regions important to the sensitivity response.

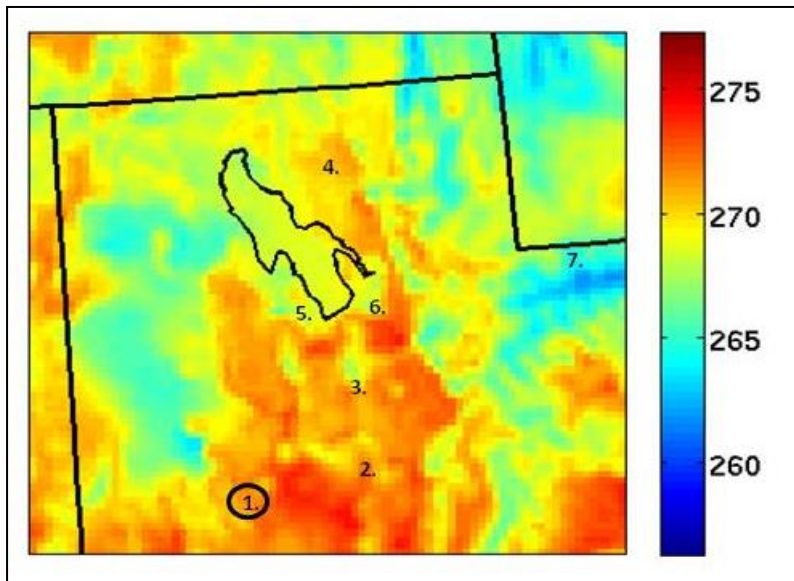


Figure 20. Ensemble mean  $\theta$  (K) at  $\eta_{-1}$  at 1800 UTC 23 January. The most sensitive 6-hour ESA grid point is marked in the black circle (#1), near the strongest concentration of warm air, south of the GSL. Other numbers (#2-7) indicate other regions of sensitivity importance.

These ranges stand in contrast to the largely north-to-south orientation of much of the terrain across northern Utah, as discussed in section III.E. The alignment of these features is important because, in contrast to terrain oriented from north-to-south, these topographic features may block or divert southerly flow. As southerly flow in this region is likely to be correlated with warm-air advection, these east-to-west terrain features are the locations where warm-air advection across the domain is indicated.

A different sensitivity response is evident in Region 4, northeast of the GSL. This region indicates a low-lying plain between the GSL and the Wasatch Range. The sensitivity evident here is created as southerly warm-air advection is forced between the higher terrain of the Wasatch and the cold dome over the GSL. Warm air spills into this plain northeast of the lake, creating a layer of positive sensitivities.

Several areas of strong negative sensitivity are also present in Figure 18, though their magnitude is less than the positive regions, with no values exceeding  $-2.5 \times 10^{-4} \text{ kg kg}^{-1} \text{ K}^{-1}$ . The negative regions indicated on the map, Region 5 (Tooele Valley), Region 6 (southeast Salt Lake Valley), and region, Region 7 (lee side of the Uinta Mountains), represent low lying areas with blocked flow where cold dense air is likely to pool during stable regimes.

Analyzed together these regions of positive and negative sensitivity reinforce the conceptual model defined in Section III. This model identifies the significance of the warm-air advection prior to the event, as well as the importance of the low level stability profile that supported the genesis of the dense fog event.

## **2. ESA (12 hour)**

The results from the 12-hour ESA in Figure 21 show a somewhat less clearly defined sensitivity relationship than the 6-hour ESA. This ESA used initial condition temperature from 1200 UTC 23 January, and forecast  $q_v$  at 0000 UTC 24 January.

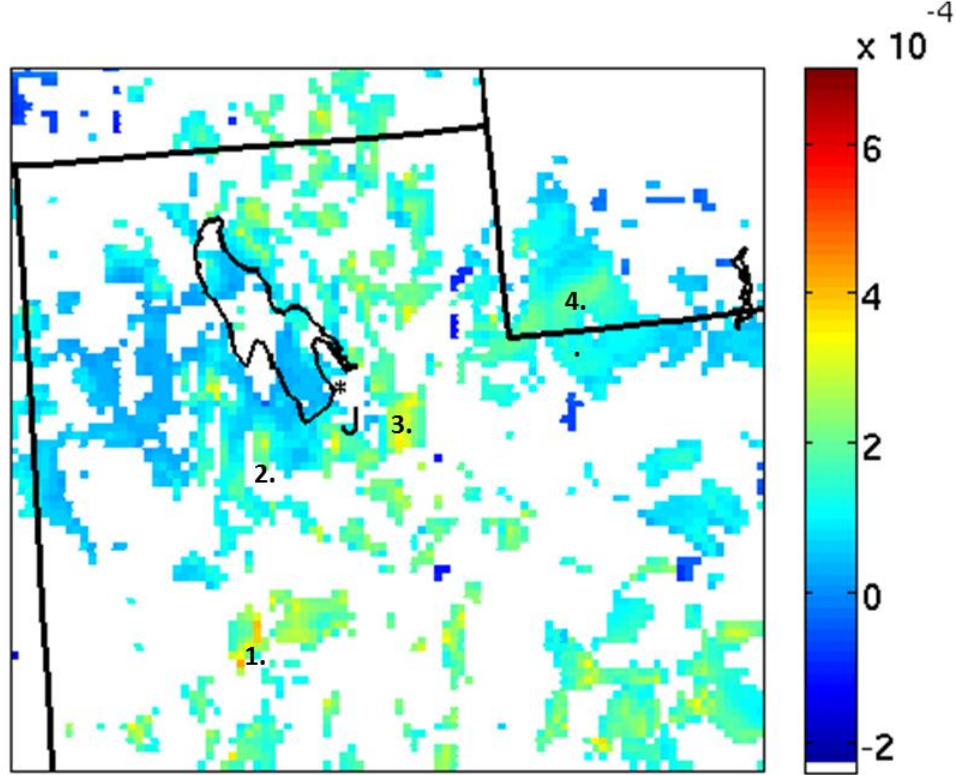


Figure 21. Sensitivities ( $dJ/dx_i$ ) using 1200 UTC 23 January analysis potential temperature (in K) as  $x_i$ , and forecasted  $q_v$  (in  $\text{kg kg}^{-1}$ ) as  $J$ , valid at 0000 UTC 24 January. Units are  $\text{kg kg}^{-1} \text{K}^{-1}$ .

The strongest positive sensitivity is located once again in the Central Utah Desert Range, as identified by Region 1 in Figure 21. This region exhibits a sensitivity range from  $3.82 \times 10^{-4}$  to  $4.193 \times 10^{-4} \text{ kg kg}^{-1} \text{K}^{-1}$ , which is weaker in magnitude, but still geographically close to the strong positive sensitivity region evident for the 6-hour ESA. Analysis at the same grid point examined for the 6-hour ESA (39.5072N 112.9197W) indicates a  $\pm 0.0684 \text{ K}$  ( $1\sigma_T$ ) change in temperature at the lowest model level will lead to  $\pm 1.787 \times 10^{-4} \text{ kg kg}^{-1}$  change in the 12-hour  $q_v$  at KSLC. We note that this value is an increase ( $+ 0.772 \times 10^{-4} \text{ kg kg}^{-1}$ ) in predicted  $q_v$  from the 6-hour ESA. This result is important because it shows a continued strong sensitivity relationship across a specific 12-hour interval which Chilcoat (2012) identified as a limitation to his ESA because of the nonlinear dynamics that were introduced by a wind shift.



The other strong sensitivity regions in the Central Utah Desert Range previously evident in the 6-hour ESA (Figure 19, Regions 2 and 3) fail the confidence interval testing. This change suggests that the warm air advection predominant in this region during the 6-hour ESA is a weaker predictor of  $J$  over the 12-hour interval. The continued presence of this strong positive sensitivity region identifies it as the most important region of sensitivity in the inner grid.

Also notable in the 12-hour ESA are the positive sensitivities at Region 2, 3, and 4, evident in Figure 21. Region 2 is centered over the Stansbury Mountain Range, which rises over 11,000 feet. This positive sensitivity over an elevated terrain region indicates an increase in vertical propagation of warm-air advection from the 6-hour ESA. This difference in vertical distribution of positive sensitivity indicates the influence of warm air at higher levels, likely enabled by the destabilizing effects of the mid-level disturbance which allows for the warm air to rise further in the atmosphere. Region 3 is very close to a 6-hour ESA negative sensitivity point in the south Salt Lake Valley (Figure 18 – Region 6). This region exhibits a sensitivity sign change from 6-hour to 12-hour forecast on a very short spatial scale (~20km across the Salt Lake Valley) and emphasizes this area as important to the understanding of the dynamic profile of this event. Region 3 is unique in that it is blocked on three sides by mountains (Oquirrh Mountains to the west, Traverse Range to the south, and Wasatch Range to the east), yet it also appears to serve as a primary corridor for warm-air advection. Region 4 represents the Green River Valley and warm sensitivities here can be attributed to the destabilizing influence of the mid level-disturbance which helped to mix out the inversion and the cold dense air trapped underneath.

Also in Figure 21 are weak negative sensitivities west of the GSL and over the south end of the GSL. These sensitivity responses may indicate the influence of the cold dense air of the lake as it expands outward from the GSL during the dense fog event.

### 3. Linear Correlation

To further examine the relationship between  $x_i$  and  $J$ , scatterplots were created for from 6-hour and 12-hour forecast data sets. These plots allow simple examination of the data with the potential to identify linear (or non-linear) relationships, clustering of variables, outliers, and changes in spread of each variable as a function of the other (Wilks 2006). Also computed was correlation coefficient between  $x_i$  and  $J$ , labeled as  $r$  on the scatterplots. This coefficient provides a measure of the strength and magnitude of the linear relationship between two variables. The ESA computed sensitivity value ( $dJ/dx$ ) also appears on each scatterplot.

Figures 22 and 23 represent the 6-hour and 12-hour 96-member ensemble scatterplots for analysis potential temperature at 1800 UTC (6-hour, Figure 22) and 1200 UTC (12-hour, Figure 23) 23 January at the most sensitive grid point (39.5072N 112.9197W) versus the forecast for  $q_v$  at KSLC at 0000 UTC 24 January. The most sensitive grid point lies approximately 170 km southwest of KSLC and was identified as Point 1 in Figure 18.

The scatterplot of the 6-hour forecast data suggest good linear agreement between the two parameters with some spread evident and a minimal number outliers. The correlation coefficient associated with this data is 0.55 and indicates a moderate linear correlation between  $x_i$  and  $J$ .

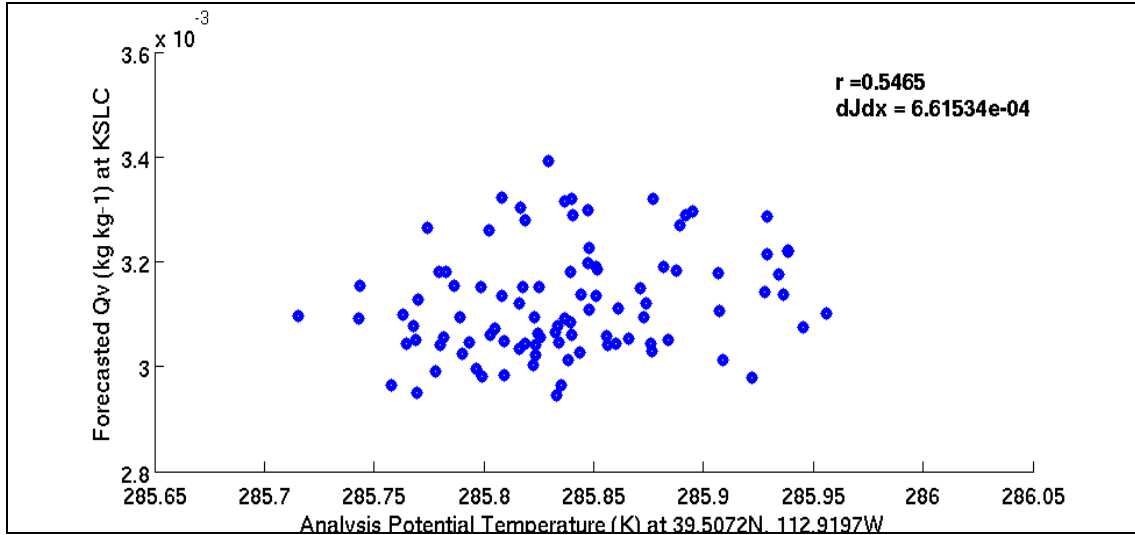


Figure 22. Scatterplot of 1800 UTC 23 January analysis  $\theta$  at the most sensitive grid point and forecasted  $q_v$  at KSLC at 0000 UTC 24 January.

Figure 23 represents the 12-hour forecast for the same parameters and indicates a significant breakdown in the linearity present in the 6-hour forecast. The associated  $r$ -value of this scatterplot is  $r = 0.023$ . Analysis of the scatterplot shows increased spread between parameters, suggesting the relationship between these variables is significantly less linear than the 6-hour forecast. A closer inspection indicates a small grouping of members predicting a higher value of  $q_v$  ( $3.15 \times 10^{-4} \text{ kg kg}^{-1}$  to  $3.45 \times 10^{-4} \text{ kg kg}^{-1}$ ) than the majority of the ensemble field. This grouping of 10 members is the likely cause for the low  $r$ -value and suggests that there is another predictor for  $J$  at this same initial time (1200 UTC 23 January). This alternate predictor could be  $\theta$  at another vertical at the same sensitivity spot,  $\theta$  at a separate grid point and/or  $\eta$ -level, or an entirely different  $x_i$  variable.

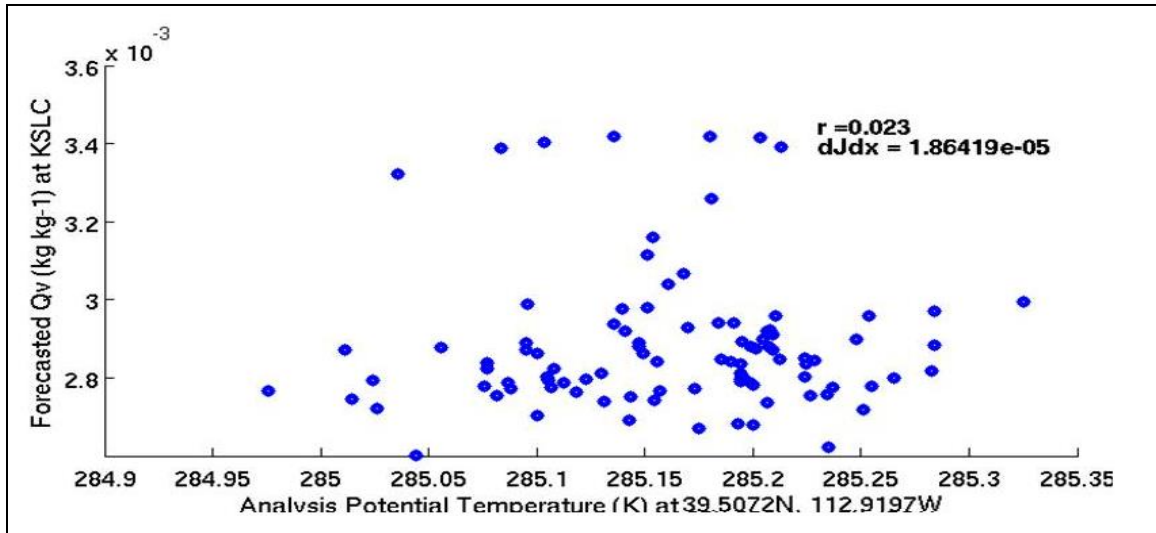


Figure 23. Scatterplot of 1200 UTC 23 January analysis potential temperature at the 6-hour ESA most sensitive grid point and forecasted  $q_v$  at KSLC at 0000 UTC 24 January.

The significant breakdown in linearity between 6-hour and 12-hour scatterplots indicates the limitation of a single fixed location to predict sensitivities over longer (>6-hour) time intervals. Examination of the sensitivity plots at both 6-hour (Figure 18, Point 1) and 12-hour times (Figure 21, Point 1) indicates that the most sensitive grid point moved 9 kilometers to the northeast from the 6-hour forecast to the 12-hour forecast. In addition, the clustering of positive sensitivity points around the maximum sensitivity grid point moved notably to the northeast and formed in a more dispersed geographic distribution. This indicates that the most sensitive grid point for one forecast time scale is not likely to be the most sensitive grid point at a different time scale.

To justify placement of future sensors using the results of an ESA, it will be necessary to create an observing network with accurate sensitivity beyond the 6-hour time frame. However, the limited forecast improvement at short time scales for one sensor location forces the consideration of a network of sensors at multiple locations. To investigate this scenario, sensitivities and linearity were also calculated at the most sensitive and second most sensitive grid point, from data provided by the 12-hour ESA.

Figure 24 shows scatterplots of 1200 UTC 23 January analysis potential temperature at the most sensitive (a.) and second most sensitive (b.) grid points as calculated during the 12-hour ESA. Both analysis potential temperature distributions are plotted against forecast  $q_v$  at KSLC at 0000 UTC 24 January. These results indicate a significant increase in linearity when compared to the distribution of data at the 6-hour ESA-indicated most sensitive grid point. Neither  $r$ -value in Figure 24 indicates strong or even moderate linearity, though an order of magnitude increase is evident in both correlation coefficient and sensitivity value. Also visible in Figure 24 is the contribution from an alternate predictor that was evident in Figure 23. The continued presence of this grouping of high  $q_v$  members at several alternate points supports the proposition that the influence of another predictor is inducing non-linear responses over this 12-hour interval.

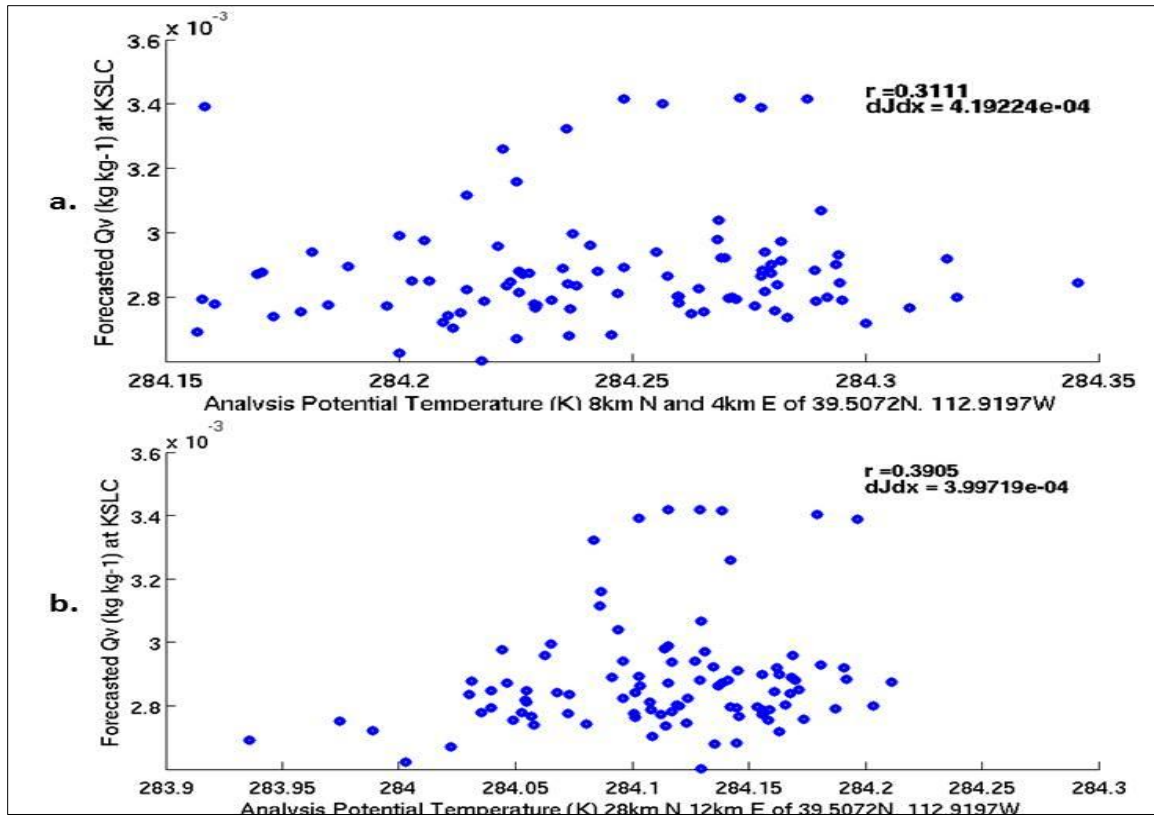


Figure 24. Scatterplot of 1200 UTC 23 January analysis potential temperature at (a.) the most sensitive grid point from the 12-hour ESA and (b.) the second most sensitive grid point from the 12-hour ESA. Both are plotted against forecast  $q_v$  at KSLC at 0000 UTC 24 January.

Also indicated along the x-axis in Figure 24 are the distances in kilometers between the 6-hour ESA most sensitive point and the 12-hour ESA first two most sensitive points. Note that the three most sensitive grid points exist across a 30-kilometer distance in varying terrain. These data suggest that a future observing network in complex terrain may need to include the placement of multiple sensors across a relatively broad swath of terrain.

#### 4. Support for Conceptual Model

Evidence supporting the above conclusions is present in the synoptic/mesoscale analysis provided in Section III which identified the role that

the mid-level disturbance played during the day on 23 January. A graphical representation is provided in Figure 25.

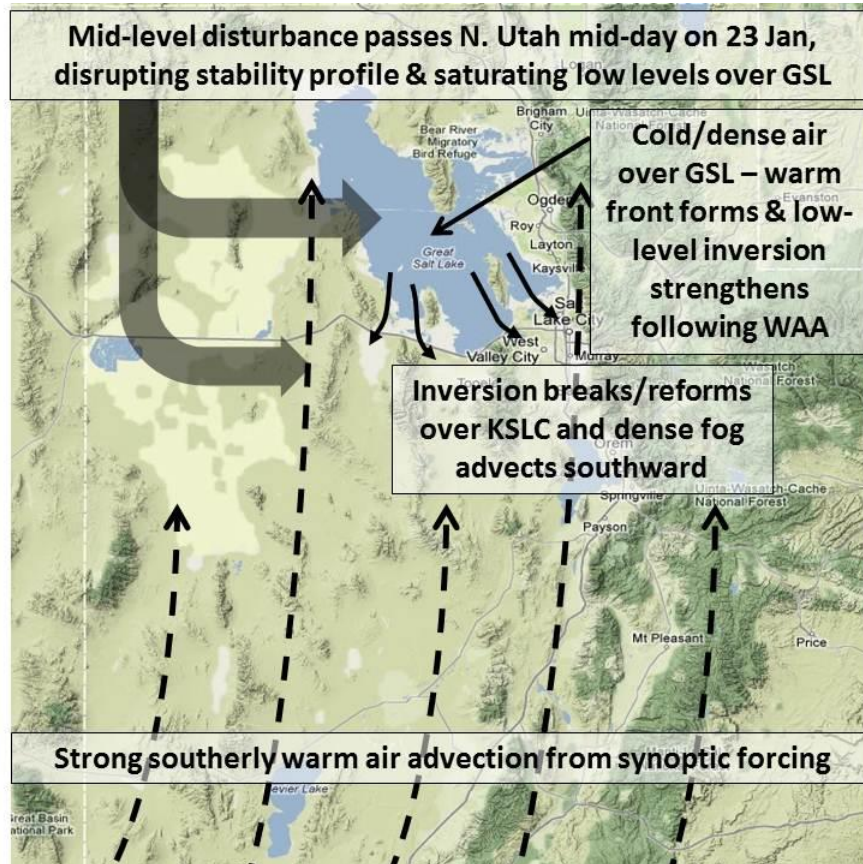


Figure 25. Schematic interpretation of effects of 23 January 2009 mid-level disturbance and synoptically forced warm-air advection that led to a dense fog event at Salt Lake City International Airport on 24 January 2009. (After Google Maps)

A schematic representing the 12-hour ESA profile (Figure 26) indicates the complexity of the forcing across this time interval. The mid-level disturbance that moved through northern Utah exhibited greater influence across the GSL basin, with lesser influence felt in central Utah. This disturbance resulted in vertical mixing of the stable boundary layer over northern Utah, which likely would have increased temperatures in low-lying valleys (positive sensitivities annotated in Regions 3 and 4, Figure 21) that had filled with cold dense air beneath low-level inversions. While the mid-level disturbance moved through



northern Utah, warm-air advection was also ongoing across the region. Warm-air advection that occurred throughout the 12-hour interval period appears at the most positive sensitive region well south of GSL (Region 1, Figure 21), and in the elevated terrain immediately south of GSL (Region 2, Figure 21). Figure 26 shows a schematic of the 12-hour ESA.

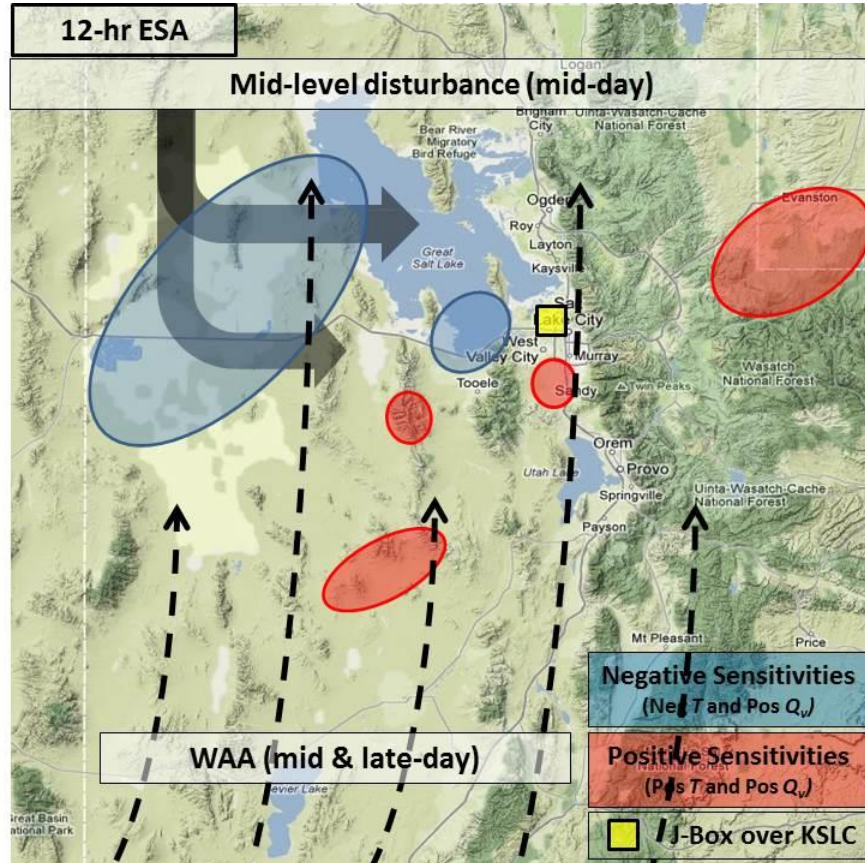


Figure 26. Conceptual sensitivity field using 1200 UTC 23 January 2009 analysis temperature as the analysis state variable ( $x_i$ ) and  $q_v$  at 0000 UTC 24 January 2009 as the forecast metric ( $J$ ) for the box centered over KSLC. (After Google Maps)

By 1800 UTC on 23 January, the influence of the mid-level disturbance had weakened enough that warm air advection began to define different 6-hour sensitivity relationships. Strong positive sensitivities were evident near elevated terrain features with at least some east-to-west aligned orographic profile (Region 1, 2, and 3, Figure 18) and where warm air advection was being



funneled (Region 4, Figure 18). This profile, combined with strong negative sensitivities in low lying areas (Region 5, 6 and 7, Figure 18) provide evidence that this flow was rebuilding stability into northern Utah. The resulting inversion helped support the advection of cold moist air over KSLC which defined the dense fog event. A schematic representing these 6-hour sensitivities appears in Figure 27.

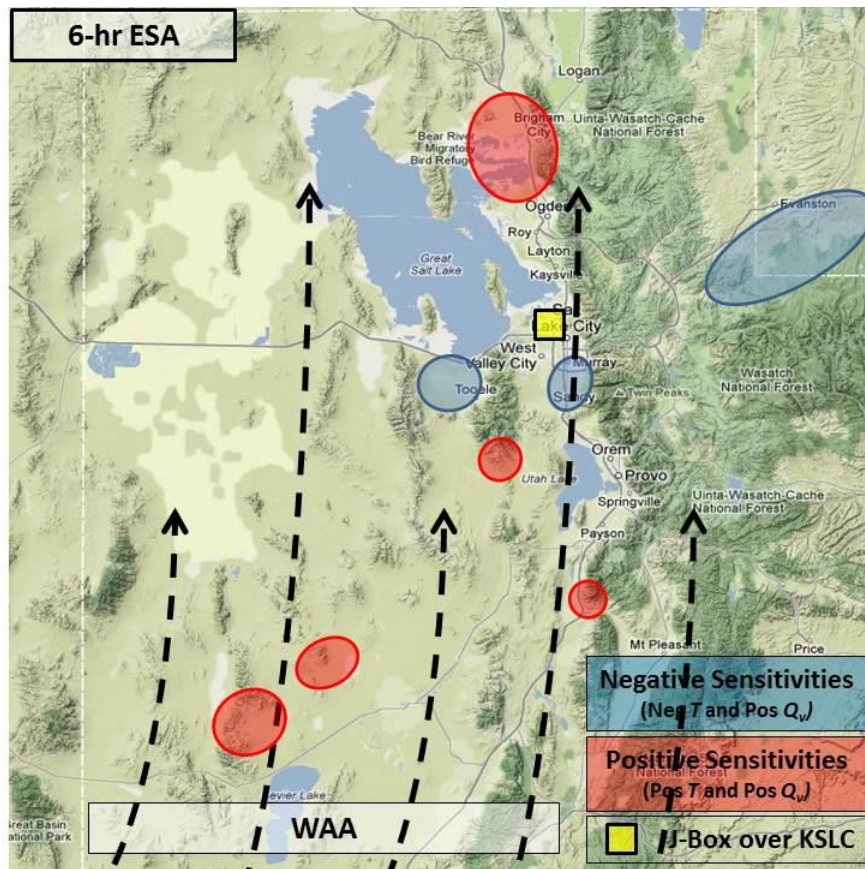


Figure 27. Conceptual sensitivity field using 1800 UTC 23 January 2009 analysis temperature as the analysis state variable ( $x_i$ ) and  $q_v$  at 0000 UTC 24 January 2009 as the forecast metric ( $J$ ) for the box centered over the SLC airport. (After Google Maps)

### C. SENSITIVITY TESTING

While the establishment of clear sensitivity relationships is important for gaining insight into the relevant atmospheric dynamics, this information alone

does not provide sufficient justification for placement of potential atmospheric sensors. In order for an additional observation to be of use, it must not only exist in a region of sensitivity, it must also be shown that the introduction of an observation at this point will improve a forecast. An observation added at a point of maximum sensitivity that does not significantly improve the forecast is of little value.

If we recall the equations that make up the ESA calculations, maximum sensitivity ( $dJ/dx$ ) occurs when correlation coefficient,  $r_{xJ}$ , is strong or when spread (standard deviation) of analysis state variable,  $\sigma_x$ , is small for a fixed  $\sigma_J$ . By adding an observation at a sensitivity point, we expect to more accurately sample conditions found in nature (decreasing  $\sigma_x$ ), thus hopefully improving the analysis that follows from a model. Decreasing  $\sigma_x$  does not inherently mean a forecast will be improved. ESA is defined by both  $r_{xJ}$ , which explains the linearity of the relationship between  $x$  and  $J$ , and the ratio of  $\sigma_J / \sigma_x$ , which quantifies the covariability of  $J$  and  $x$ . The contribution to sensitivity by these variables is not equal. Correlation coefficient can only serve to reinforce sensitivity values when the relation between  $x$  and  $J$  is perfectly linear ( $r = \pm 1$ ). When the relationship is not perfectly linear ( $-1 < r < +1$ ), the correlation coefficient only reduces the overall sensitivity value. To maximize sensitivity, we must first have a large  $\sigma_J / \sigma_x$  ratio, then a strong associated  $r$ -value. Thus in choosing to introduce an observation at a position of max sensitivity defined by ESA, we cannot be certain that an improvement in forecast accuracy will follow.

## 1. Perturbation Tests

Two perturbation tests were conducted to examine whether the introduction of an observation at a point of sensitivity could improve a later forecast for  $q_v$ . The observation is represented by  $x_s$ , an element of a state vector at the 6-hour ESA most sensitive grid point  $X = 121$ ,  $Y = 52$  (39.5N, 112.9W). Analysis ensemble data came from the 1800 UTC 23 January ensemble mean while forecast predictions occur at 0000 UTC 24 January.

**a.  $+1\sigma_T$  Perturbation Test**

The first test introduced a perturbation of  $+1\sigma$  temperature for  $x_s$  at the first  $\eta$ -level. This test simulated the introduction of a real observation. The perturbation was introduced by increasing the ensemble mean temperature value for  $x_s$  by 1 standard deviation of the ensemble mean ( $+1\sigma_T = 0.0516$ ). The effect of this perturbation was spread through to other model variables in the horizontal and vertical through simple linear regression of the analysis error statistics sampled by the analysis ensemble. This linear regression ensured a balanced response to the perturbation and subsequent analysis.

Figure 28 shows the 1800 UTC 23 January analysis change at  $\eta_{-1}$  (in K) that is calculated after the introduction of the  $+1\sigma_T$  perturbation at the most sensitive grid point in the 6-hour ESA. The black dot indicates the location where the perturbation was introduced. This figure shows that temperature has increased across the Salt Lake Valley, and at KSLC. While it may be expected to see the strongest response to the perturbation where the perturbation was introduced ( $x_s$ ), because no covariance localization is applied, the perturbation response depends entirely on the covariance of the background temperature field. It has already been discussed how significant the warm air advection in and around KSLC was in leading to the dense fog at KSLC and these results further support that reasoning. Warmer air at the most sensitive grid point ( $+1\sigma_T$ ) helps induce a stronger inversion over the southeast GSL as the warm air overrides the cold dome, leading to a later dense fog intrusion under the strengthened inversion. Also evident in Figure 28 is a region of strong decrease in temperatures west of the GSL. This area represents the low lying Great Salt Lake Desert. A warm perturbation introduced in the elevated terrain south of the Great Salt Lake Desert would, with southerly flow, likely advect warm air over the PBL in this region, creating or strengthening a low level inversion and inducing colder temperatures than in surrounding areas.

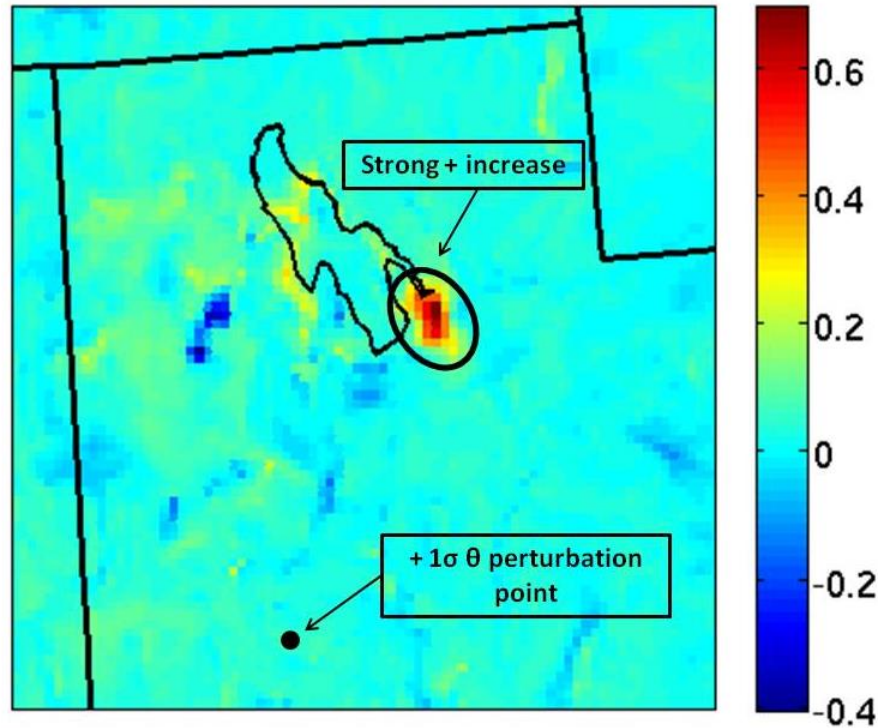


Figure 28. Analysis change (in K) after the addition of  $+1\sigma$   $\theta$  perturbation applied at  $39.51^\circ\text{N}$ ,  $112.97^\circ\text{W}$  at the first  $\eta$ -level. The perturbation point is indicated by the black dot. Positive values indicate an increase in  $\eta_{-1}$  temperatures, while negative values indicate a decrease. Note the strong positive increase in  $\theta$  in the Salt Lake Valley, directly over KSLC.

Next it must be determined what change in forecast is created by the  $+1\sigma_T$  perturbation. This is done by integrating all members of the perturbed ensemble model forward to the valid forecast time, 0000 UTC 24 January, to see if these new forecasts differs from the unperturbed forecasts. The focus of this test is to examine the forecast for  $q_v$  at KSLC ( $J$ -box) to determine what change has occurred. Figure 29 shows the results of this test. The graphic represents the difference in 6-hour forecasted  $q_v$  ( $\text{kg kg}^{-1}$ ) between the forecast created using the 1800 UTC 23 January  $+1\sigma_T$  perturbed analysis and the forecast created using the 1800 UTC 23 January unperturbed analysis. Note that this graphic does not accurately show the forecast difference within the entire  $J$ -box as it only displays  $q_v$  at the lowest model level and the  $J$ -box value includes all points over the first two model levels.

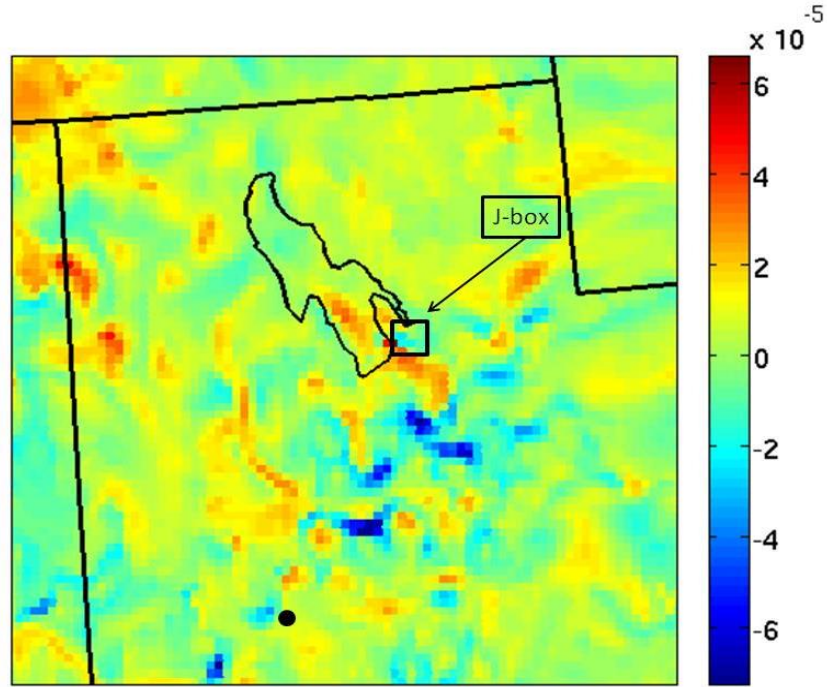


Figure 29. Forecast difference in  $q_v$  (in  $\text{kg kg}^{-1}$ ) at 0000 UTC 24 January at the lowest model level ( $\eta_{-1}$ ) following the introduction of a  $+1\sigma_\theta$  perturbation to the 1800 UTC 23 January ensemble analysis at the most sensitive grid point (black dot).

The total difference within the *J*-box at KSLC between the perturbed and unperturbed forecast is difficult to quantify by visual examination of Figure 29. The *J*-box appears to contain positive and negative areas, while strong positive increases (increased  $q_v$ ) are evident over the south GSL and south of the *J*-box. The exact forecast difference in the *J*-box is a decrease in  $q_v$  ( $-7.3 \times 10^{-6} \text{ kg kg}^{-1}$ ). Though it would be preferred to see an increase in  $q_v$  following the introduction of the  $+1\sigma_T$  perturbation, there is a clear strong positive response across the southern half of the GSL and the exact change at KSLC is only weakly negative. The known forecast timing error within the forecast system (ending the fog event 3-6 hours early) may have contributed to this finding. In addition, the significant difference in and around the *J*-box suggests that a positive forecast change exists within a few grid points. This result may also indicate the presence of weak nonlinearity in the system.

Also evident in Figure 29 are several areas of strong increase in  $q_v$  west and northwest of GSL, along the border of northeast Nevada and southern Idaho. It is speculated that these areas are associated with enhanced vertical motion along significant terrain features with east-to-west orientation in the region. It is believed that the warm perturbation induced an increase in southerly flow, enhancing convergence along the elevated terrain. This change induced stronger vertical motion, enhanced adiabatic cooling and condensation, leading to increases in  $q_v$  concentrations.

**b. “Truth” Perturbation Test**

A different procedure was then completed to measure the introduction of a real world “truth” observation to determine if a more accurate forecast could be created. Following Evensen (1994) regarding EnKF, Anderson (2001) regarding Ensemble Adjustment Kalman Filter (EAKF), and Anderson et al. (2009) regarding DART implementation of EnKF, we define matrix DA for our ensemble as:

$$\bar{\mathbf{x}}_a = \bar{\mathbf{x}}_f + \bar{\mathbf{K}}(\bar{\mathbf{y}}_o - \bar{\mathbf{H}}\bar{\mathbf{x}}_f)$$

where  $\bar{\mathbf{x}}_a$  stands for the analysis background variable,  $\bar{\mathbf{x}}_f$  the forecast background variable,  $\bar{\mathbf{K}}$  Kalman gain,  $\bar{\mathbf{y}}_o$  the assimilated observations, and  $\bar{\mathbf{H}}$  a matrix forward operator.

Matrix DA performed with a single observation becomes

$$\bar{\mathbf{x}}_a = \bar{\mathbf{x}}_f + \bar{\mathbf{K}}(y_o - \bar{\mathbf{H}}\bar{\mathbf{x}}_f)$$

with  $y_o$  representing the single observation and  $\bar{\mathbf{H}}$  a row vector forward operator.  $\bar{\mathbf{K}}$  is now defined as

$$\overline{\overline{K}} = \frac{\overline{\overline{\rho}} \circ \overline{\overline{P}}_f \overline{\overline{H}}^T}{\overline{\overline{H}} \overline{\overline{\rho}} \circ \overline{\overline{P}}_f \overline{\overline{H}}^T + \sigma_o^2}$$

where  $\overline{\overline{\rho}}$  represents the covariance localization matrix,  $\overline{\overline{P}}_f$  the background error variance matrix,  $\circ$  the Hadamard or Schür product between the two arguments, and  $\sigma_o^2$  the observation error covariance matrix. We can then rewrite our DA in scalar form with single scalar additional observation as

$$x_a = x_f + \frac{\rho_{xy} \sigma_{xy}^2}{\rho_{yy} \sigma_{yy}^2 + \sigma_o^2} (y_o - y_f)$$

with  $\sigma_{xy}^2$  representing the covariance between the arguments,  $\sigma_{yy}^2$  the variance between the arguments, and  $y_f$  the forecast value of  $y_o$ , (i.e.  $H^T \overline{x}_f$ ). This equation represents how the additional observation, in the form of the perturbation, is assimilated, allowing the contribution of one single observation to be measured.

DA for this perturbation was done by introducing the single observation representing the truth value of temperature at 1800 UTC 23 January at  $\eta_{-1}$  for  $x_s$ . The single observation was assimilated into the 96-member ensemble as defined previously in this section. After assimilating the observation,  $y_o = x_t$  for truth, the model background  $\sigma_x$  of  $\theta$  at  $x_s$  for the 1800 UTC analysis was reduced from 0.0516 to 0.0421. The effect of this assimilated “truth” observation was to reduce  $\sigma_x$  and thus reduce analysis uncertainty.

Figure 30 shows the difference in 1800 UTC 23 January analysis after the “truth” observation had been assimilated at the most sensitive 6-hour ESA grid point ( $x_s$ ,  $x = 121$ ,  $y = 52$  (39.5N, 112.9W)). This plot is obtained by subtracting the analysis of the unperturbed model run from the analysis of the perturbed model run.



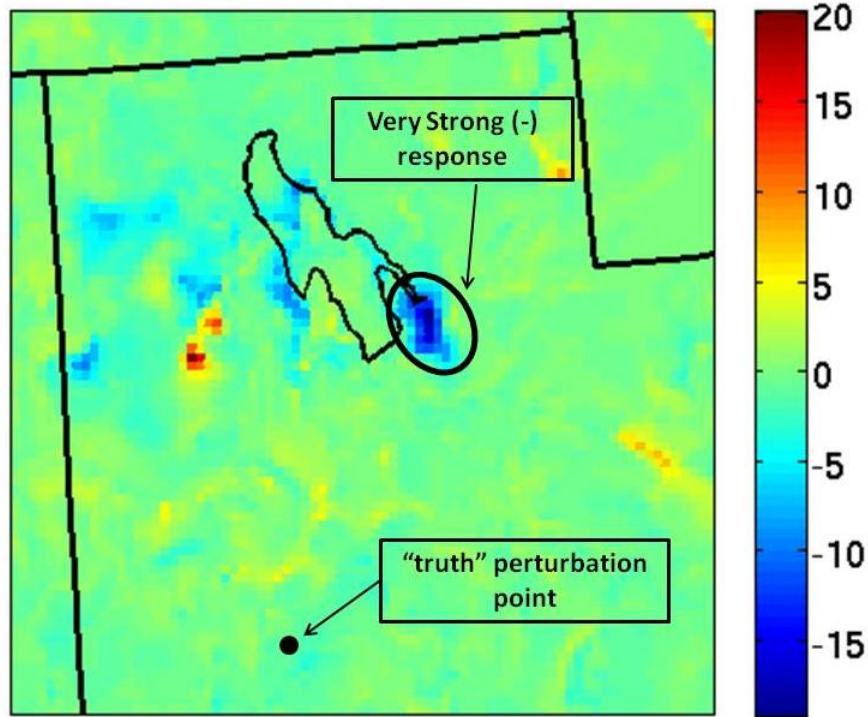


Figure 30. 1800 UTC 23 January analysis change (in K) after the addition of “truth” observation applied at  $39.51^{\circ}\text{N}$ ,  $112.97^{\circ}\text{W}$  at  $\eta_{-1}$ . The observation point is indicated by the black dot. Positive values indicate an increase in  $\eta_{-1}$  temperatures, while negative values indicate a decrease. Note the very strong negative response in  $\theta$  in the Salt Lake Valley, directly over the KSLC J-box.

Figure 30 shows analysis change ranging from  $\pm 20$  K, a notable increase in magnitude from the  $+1\sigma_T$  perturbation which yielded analysis change  $\pm 0.6$  K. Importantly, the location of maximum temperature change again is focused on the Salt Lake Valley, in and around KSLC, though the analysis change in this area is now negative. This sign change is expected, as the assimilation of the truth observation ( $\delta x = -0.0826$  K) lowered the background temperature at  $x_s$  ( $-1.1$  K). The similarity in geographic position of analysis change between  $+1\sigma_T$  perturbation and “truth” observation near KSLC is important to our results and shows that the ensemble filter is a modified direct linear regression.

Notably, the analysis temperature change at KSLC after assimilating the “truth” observation was significantly greater ( $-16.6$  K) than the



analysis change at  $x_s$  (-1.1 K). The significant difference in analysis change between the  $+1\sigma_T$  perturbation and the “truth” perturbation may be explained partially by the difference in assimilation procedures, which provided different means of altering initial conditions. The more significant contribution to the difference in analysis change likely comes from the magnitude of the difference between the  $+1\sigma_T$  perturbation (+0.0516 K) and the “truth” observation (-1.1 K). The significantly larger “truth” observation leads to a comparably large change in analysis.

Also evident is an area of strong positive analysis change west of the GSL. This region represents the Great Salt Lake Desert that was identified with the  $+1\sigma_T$  perturbation (Figure 28). As expected, because the perturbation introduced with the “truth” test was negative, this decreased the amount of warm-air advection west of the GSL, thus weakening or eroding any inversion present in this area. With a weakened or eroded inversion, cold air is no longer trapped at the surface as efficiently as occurred before the perturbation. This change results in an increase in temperature at the surface, as evidenced by the positive analysis temperature change in this area.

As predicted by our ESA, a reduction in  $\theta$  at  $x_s$  at analysis time (1800 UTC 23 January), as occurred during DA of the “truth” observation, should predict a consequent forecast reduction in  $q_v$  at a later time at KSLC (0000 UTC 24 January). Figure 31 shows the forecast difference that occurs between the unperturbed 6-hour forecast and the 6-hour forecast with initial conditions perturbed by the “truth” observation. As with Figure 29, this graphic represents only the lowest model level, and does not show the distribution  $q_v$  difference in the entire  $J$ -box.

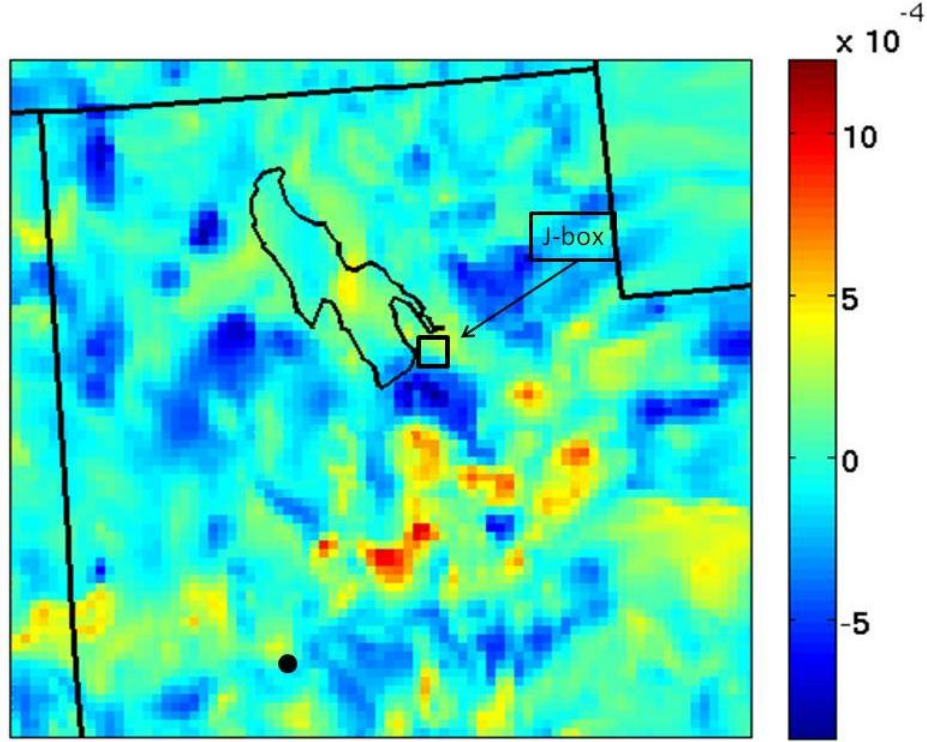


Figure 31. Forecast difference in  $q_v$  (in  $\text{kg kg}^{-1}$ ) at 0000 UTC 24 January at the lowest model level ( $\eta_{-1}$ ) following the introduction of a “truth” perturbation to the 1800 UTC 23 January ensemble analysis at the most sensitive grid point (black dot)

As with the  $+1\sigma_T$  perturbation forecast difference, the distribution of the forecast  $q_v$  differential across the  $J$ -box appears difficult to discern by visual inspection, with both positive and negative values present. Summation of  $q_v$  within the  $J$ -box reveals an overall forecast decrease of  $-4.765 \times 10^{-4} \text{ kg kg}^{-1}$ . As expected, the magnitude of  $q_v$  forecast difference has increased by an order of magnitude from the  $+1\sigma_T$  perturbation, roughly matching the order of magnitude change in analysis  $\theta$  at  $x_s$ . In addition, the concentration of higher  $q_v$  that appeared immediately south of the GSL following the  $+1\sigma_T$  perturbation (Figure 29) has reversed sign.

Within Figure 31, a concentrated area of strong ( $> 8.0 \times 10^{-4} \text{ kg kg}^{-1}$ ) positive forecast change is evident further south ( $\sim 100 \text{ km}$ ) of the GSL. In Figure 16 ( $\eta_{-1}$  ensemble mean  $q_v$ ), this same region appeared as a pooling area for

water vapor between 0300 UTC and 0600 UTC 24 January. It is unclear from Figure 31, and the input provided by the previous analyses and forecast difference plots, what the significance of this region is and how it relates to  $q_v$  at KSLC. It is speculated that a decrease in warm-air advection in this region may decrease low-level drying that would have resulted from the advection of dry continental air, though this is uncertain.

These results are positive indications that the introduction of an observation produces the results that are predicted by the ESA (e.g. increase/decrease  $\theta$  at  $x_s$  at analysis time yields increase/decrease  $q_v$  at later forecast time). The next step is to analyze how these results compare to the theoretical predictions of ESA.

## **2. ESA Predicted Sensitivity Test**

ESA calculations provide an alternate means to test sensitivity predictions. We previously defined ESA sensitivity as  $dJ/dx$ , which predicts change in  $J$  ( $\delta J$ ) for a given change in  $x$  ( $\delta x$ ). Procedures for calculating a value for  $\delta x$  differs based upon the assimilation methodology used which is defined by experiment purpose. Once the procedure for  $\delta x$  has been defined, the specific value of  $\delta x$  may be multiplied by sensitivity ( $\delta J / \delta x$ ), the product of which is an expected change in  $J$  ( $\delta J$ ), our sensitivity prediction. Figure 32 is a schematic representing the two different means of calculating expected  $\delta J$  for this experiment.

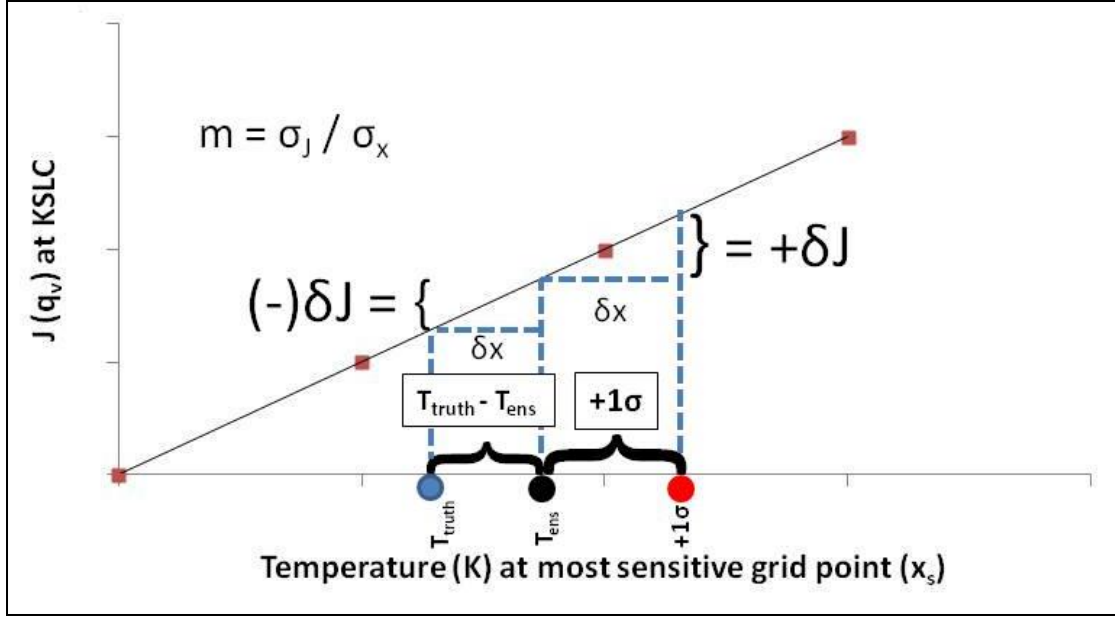


Figure 32. Schematic representing how expected change in  $J$  ( $\delta J$ ) is calculated for (1)  $+1\sigma$  perturbation and (2) “truth” perturbation. The x-axis shows temperature (in K) at the most sensitive grid point in the domain. The y-axis shows the corresponding forecast  $q_v$  at KSLC at a later time. The correlation shown is idealized as perfectly linear.

**a.  $+1\sigma_T$  Perturbation Test**

To simulate an observation,  $\delta x$  is arbitrarily defined as  $+1\sigma$  temperature perturbation, as shown in Figure 32. This perturbation moves the ensemble mean  $\theta$  at the most sensitive grid point by  $+1\sigma$ . Linear regression as previously defined was performed to ensure balanced introduction of the perturbation. With  $\delta x$  now defined as  $+1\sigma_T$ , we then multiplied this value (0.0564 K) by the 6-hour ESA calculated sensitivity ( $6.6153 \times 10^{-4} \text{ kg kg}^{-1} \text{ K}^{-1}$ ), to obtain our expected  $\delta J$  as  $3.3731 \times 10^{-5} \text{ kg kg}^{-1}$ .

**b. “Truth” Observation Test**

As previously described, our matrix DA is performed as

$$\bar{x}^a = \bar{x}^f + \bar{K}(y^0 - \bar{H}\bar{x}^f)$$

and in scalar form as

$$x^a = x^f + K(y^0 - x^f).$$

This can be then rewritten as:

$$x^a - x^f = K(y^0 - x^f)$$

where  $K(y^0 - x^f)$  represents our analysis increment. We then recognize

$x^a - x^f$  as  $\frac{\partial x^a}{\partial y}$ . Multiplying  $\frac{\partial x^a}{\partial y}$  times our previously defined sensitivity value

function,  $\frac{\partial J}{\partial x^a}$ , we return

$$\frac{\partial x^a}{\partial y} \cdot \frac{\partial J}{\partial x^a} = \frac{\partial J}{\partial y}$$

which provides,  $\frac{\partial J}{\partial y}$ , an expected change in forecast variable ( $J$ ), given a change

in observation ( $y$ ). The input for  $x^a - x^f$ , or  $\delta x$ , is provided as the  $\theta$ -difference at  $\eta_{-1}$  between the 1800 UTC 23 January “truth” temperature (Figure 32 -  $T_{\text{truth}}$ ), and the 1800 UTC 23 January analysis mean background field (Figure 32 -  $T_{\text{ens}}$ ) at

the most sensitive grid point. This value ( $\frac{\partial x^a}{\partial y} = -1.0528$  K) is then multiplied by

the sensitivity value at the 6-hour ESA most sensitive grid point ( $\frac{\partial J}{\partial x^a} =$

$6.6153 \times 10^{-4}$  kg kg<sup>-1</sup> K<sup>-1</sup>). The resulting value ( $\frac{\partial J}{\partial y} = -6.9646 \times 10^{-4}$  kg kg<sup>-1</sup>) is the

expected change in  $\delta J(q_v)$  at KSLC at 0000 UTC 24 January.

### 3. Actual Versus Expected Forecast Change

If we consider the simulations performed through perturbation testing (section III.C.1. and III.C.2.) as the actual change in forecast and then consider the ESA predicted test as the expected change in forecast, we can compare these results to determine the validity of the ESA.

|  | +1 $\sigma$ Perturbation<br>(K)           | "Truth"<br>Observation (K)                |
|--|---|---|
| Perturbation Test<br>(Actual Change)     | $-7.30 \times 10^{-6} \text{ kg kg}^{-1}$ | $-4.77 \times 10^{-4} \text{ kg kg}^{-1}$ |
| ESA Prediction Test<br>(Expected Change) | $3.73 \times 10^{-5} \text{ kg kg}^{-1}$  | $-6.97 \times 10^{-4} \text{ kg kg}^{-1}$ |

Table 3. Comparison of Actual versus Expected  $q_v$  changes in  $\text{kg kg}^{-1}$  at KSLC at 0000 UTC 24 January with (1) +1 $\sigma$  Perturbation (K) and with (2) "Truth" Observation (K) at 6-hour ESA most sensitive grid point at 1800 UTC 23 January.

Table 3 shows the results of each test. First looking at the +1 $\sigma$  perturbation, it is evident that the actual change ( $-7.30 \times 10^{-6} \text{ kg kg}^{-1}$ ) and the expected change ( $3.73 \times 10^{-5} \text{ kg kg}^{-1}$ ) differ in both sign and magnitude. It is speculated that poorly correlated values presented by the actual perturbation test can be attributed to deficiencies in how the observation is assimilated. As described earlier, the perturbation is introduced by increasing the ensemble mean  $\theta$  value +1 $\sigma$ , followed by linear regression to distribute the new value. This process may not fully capture the impact of the perturbation, thus introducing errors in the system which contributes to error in forecast values.

Assimilating the "truth" observation using DA yields amore encouraging results with agreement in sign (negative) and magnitude ( $\times 10^{-4} \text{ kg kg}^{-1}$ ). Because our "truth" observation had reduced our ensemble mean  $\theta$  for  $x_s$ , a subsequent decrease in  $q_v$  at KSLC at a later time is expected, and is shown to be true in Table 3. This agreement is significant and informs us that our ESA can successfully predict changes in fog at KSLC.

#### D. ENSEMBLE SIZE TESTING

The establishment of the size of the ensemble system (member of ensemble members) needed to perform a reliable ESA is one of the primary focuses of this study. Identifying this information helps to establish the computational requirements necessary to implement a reliable ESA. This factor

is important when determining whether or not an NWP computing center can operationally implement such measures into their DA process. Even if not used operationally, the need to use the appropriate number of ensemble members is critical to building an accurate sensitivity study for placement of future observations.

Chilcoat (2012) identified the requirement for an ensemble system to consist of 30-40 members to skillfully determine sensitivity of forecast fog at KSLC. In addition to the use of a different initial condition parameter, Chilcoat's research did not implement the stringent requirement for Gaussianity that was implemented for this research; therefore different results are to be expected.

Ensemble sub-selection procedures were detailed in section III. Results were obtained using ensemble sizes of 96, 80, 64, and 48 members for both 6-hour and 12-hour sensitivity analyses. Sensitivities ( $dJ/dx_i$ ) were calculated using initial condition  $T$  (K) as  $x_i$  and forecast  $q_v$  ( $\text{kg kg}^{-1}$ ) for  $J$  the 12km x 12 km  $J$ -box surrounding KSLC. Comparison of sensitivity results between ensemble systems occurred through a visual analysis of sensitivity plots and numerical analysis of sensitivity values. Continuity between ensemble systems was established by identifying similar geographical positioning and magnitude of +/- sensitivities across the domain. The 10 strongest sensitivities were identified, by grid point, for each size ensemble system at both 6-hour and 12-hour times. The three strongest sensitivity points are identified in Figures 33 and 34. All sensitivities failing the 95% confidence interval test are masked.

## **1. 6-hour ESA**

Figure 33 shows the result of the ESA for all four 6-hour ensemble systems. The 96-member ensemble system served as the standard which the other systems were compared against. Features of the 96-member system were defined in section IV.B. The most sensitive point in the 96-member ensemble exists at (39.5072N, 112.9197W) and is identified at Point 1, 96-member plot, Figure 18. Notable in the 96-member ensemble is strong agreement within the model system of the location of greatest sensitivity, with seven of the top ten sensitivities existing in and around the most sensitive grid point.

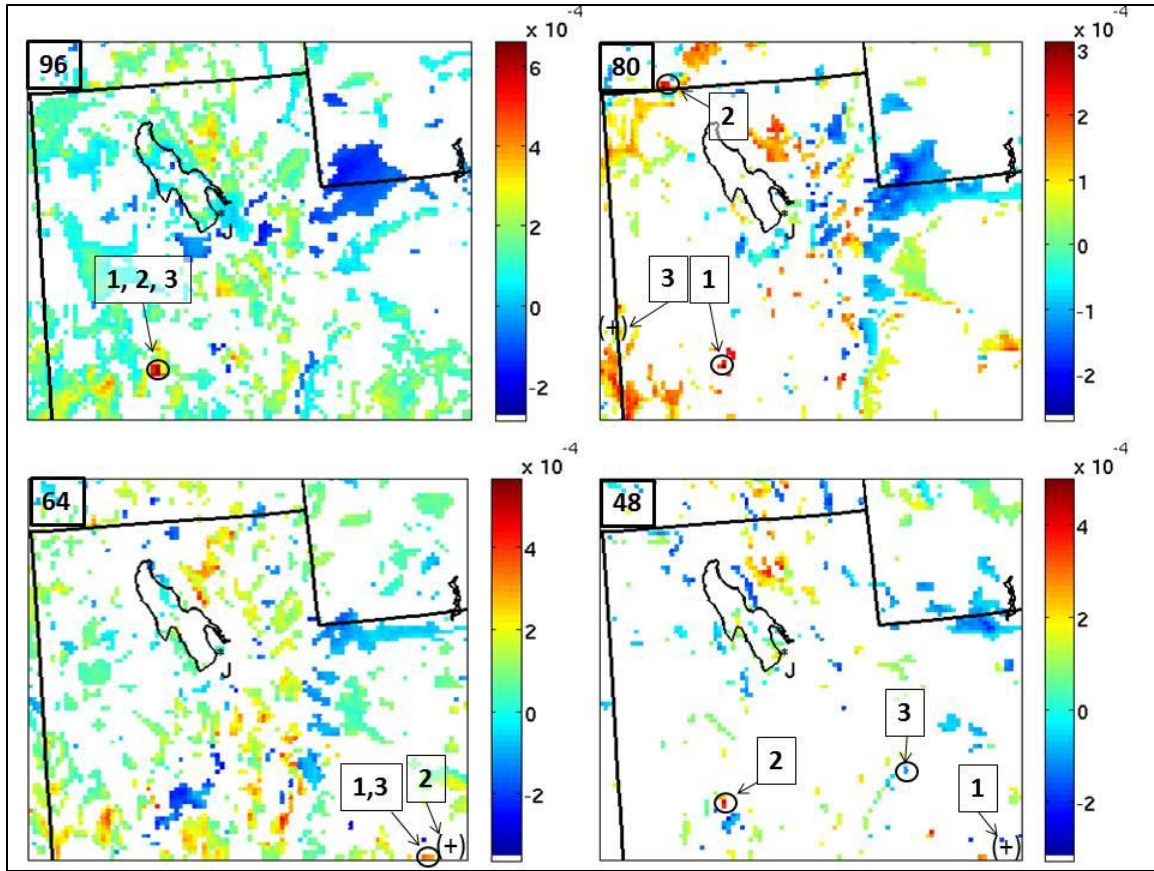


Figure 33. Plot of 6-hour sensitivity ( $dJ/dx_i$ ) for 96, 80, 64, and 48-member ensemble systems using initial condition  $T$  (K) from 1800 UTC 23 January 2009 and forecast  $q_v$  ( $\text{kg kg}^{-1}$ ) at KSLC at 0000 UTC 24 January 2009. Units are  $\text{kg kg}^{-1} \text{K}^{-1}$ . Number boxes identify grid points of the strongest three sensitivities in each plot. Markers indicating (+) or (-) represents a positive or negative sensitivity that exists outside the graphic. Top left number represents number of ensemble members used to perform ESA. Note: scales are not normalized.

The 80-member system agreed relatively well with positioning of 96-hour features. Areas of +/- sensitivity retain similar geographical arrangement which suggest good agreement between the ensembles. Magnitude of the features does not match as well, with only the strongest sensitivity grid point retaining its position, and overall reduction in sensitivity values with the most sensitive grid point reducing in strength from  $6.615 \times 10^{-4} \text{ kg kg}^{-1} \text{K}^{-1}$  to  $3.021 \times 10^{-4} \text{ kg kg}^{-1} \text{K}^{-1}$ . Note also the reduction in scale between 96- and 80-member ensemble systems.



In addition, the next two strongest grid points existed in different areas of the map, indicating a breakdown in the agreement of the most sensitive region that existed in the 96-member system.

The 64-member ensemble also retained a similar geographic arrangement as the 96-hour member with the most salient features still present. This system begins to experience more magnitude displacement as the three most sensitive grid points are well southeast of the GSL, though they occur in relative proximity to each other. The location of maximum sensitivity in the 96-member system now ranks ninth in magnitude with sensitivity of  $4.114 \times 10^{-4} \text{ kg kg}^{-1} \text{ K}^{-1}$ . In addition some different +/- groupings begin to emerge that differ from those in the 96- and 80-member systems. Because of the deterioration in magnitude and position of sensitivities, this is likely below the minimum size ensemble needed to successfully implement a 6-hour ESA.

The 48-member ensemble also retains the most salient sensitivities from the 96-hour member, though most of the sensitivities fail the CI test. Interestingly, the response at the 96-member region of maximum sensitivity improves from the 64-member ensemble, as the second and ninth most sensitive grid points emerge in this area. The system has lost little sensitivity magnitude, as the sensitivity at Point 2 (Figure 33 - bottom right) is  $4.239 \times 10^{-4} \text{ kg kg}^{-1} \text{ K}^{-1}$ , which is second in magnitude to the 96-member ensemble responses at this point. This seemingly counterintuitive increase in sensitivity can be attributed to sampling error. As ensemble size decreases covariances can become overestimated, while variances can become underestimated. This occurs as the increasingly smaller ensemble samples a smaller portion of the true population, drawing a less accurate representation of the system parameters and increasing sampling error.

## **2. 12-hour ESA**

The overall response of the 12-hour ensemble sub-systems (Figure 34) varied significantly from the 6-hour. The 96-member ensemble again served as

the control “best-response” for comparison. Explanation of the 12-hour 96-member ensemble sensitivity is found in section IV.B. The primary features of the 96-member 12-hour system indicate strong positive sensitivities in the Central Utah Desert Range and in lower lying valleys south and east of the GSL. The point of maximum sensitivity exists in the same general area as the 6-hour system (identified as points 1, 2, and 3, Figure 34 - top left), with maximum sensitivity of  $4.192 \times 10^{-4} \text{ kg kg}^{-1} \text{ K}^{-1}$ .

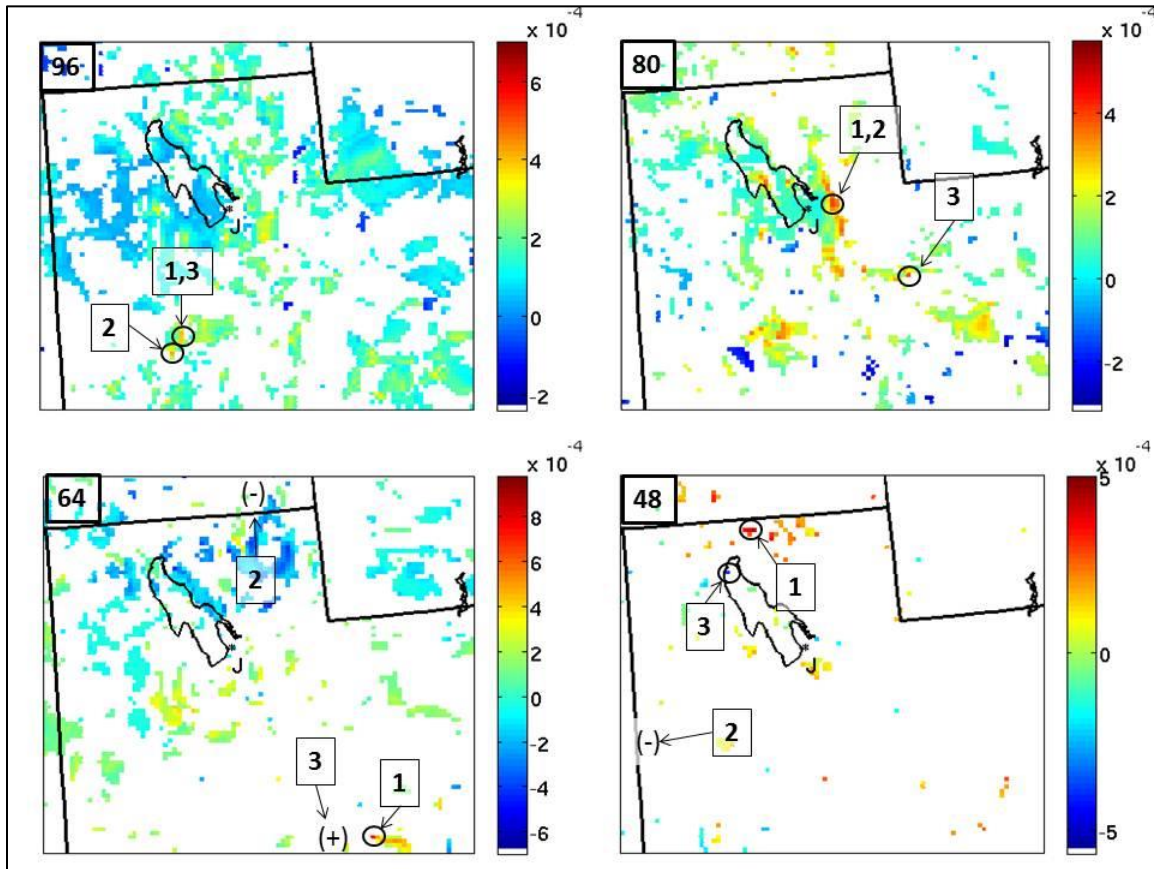


Figure 34. Plot of 12-hour sensitivity ( $dJ/dx_i$ ) for 96, 80, 64, and 48-member ensemble systems using initial condition  $T$  (K) from 1800 UTC 23 January 2009 and forecast  $q_v$  ( $\text{kg kg}^{-1}$ ) at KSLC at 0000 UTC 24 January 2009. Units are  $\text{kg kg}^{-1} \text{ K}^{-1}$ . Number boxes identify grid points of the strongest three sensitivities in each plot. Markers indicating (+) or (-) represent a positive or negative sensitivity that exists outside the graphic. Top left number represents number of ensemble members used to perform ESA. Note: scales are not normalized.

The 80-member ensemble system exhibited notable difference from the 96-member system. While the region of positive sensitivities in the Central Utah Desert Ranges was evident, this region produced only the sixth strongest sensitivity in the domain. The strongest sensitivities emerged on the Front Range of the Wasatch Mountains, immediately east of KSLC. Values here exhibited maximum sensitivity of  $3.964 \times 10^{-4} \text{ kg kg}^{-1} \text{ K}^{-1}$ . This system also produced a number of seemingly spurious +/- sensitivity regions, when compared against the 96-member system. This result is to be expected, when considering the mesoscale conditions that existed over the 12-hour period. While warm air advection was predominant across central and southern Utah, northern Utah experienced greater variability in forcing as the effect of the mid-level disturbance was replaced by southerly flow.

The sensitivity profile of the 64-member ensemble did not resemble the 96-member system in geographical area or magnitude. No previously recognized sensitivity features were evident with the 64-member system. Of significance was the magnitude that did exist with the system. The most sensitive point, well southeast of GSL and identified as Point 1, Figure 34 (bottom left), had sensitivity of  $7.276 \times 10^{-4} \text{ kg kg}^{-1} \text{ K}^{-1}$ , which was the strongest value exhibited at any point during this study. The lack of coherent sensitivity in this system indicates a significant discontinuity with the 96- and 80-member systems.

The 48-member ensemble system exhibited even less coherence in sensitivity response, with most points on the domain failing the CI test. Though the strongest sensitivity value is comparable to other systems at  $4.344 \times 10^{-4} \text{ kg kg}^{-1} \text{ K}^{-1}$ , this system, like the 64-member system, is not likely useful as an accurate ESA system. Further examination will explore this proposal.

### **3. Linearity of the 6-hour Positive Sensitivities**

Figure 35 is the scatterplots for the 6-hour ESA created with 96-, 80-, 64-, and 48-member ensemble systems. The x-axis in each scatterplot in Figure 35

represents the ensemble mean analysis potential temperature (in K) at 1800 UTC 23 January 2009 at the lowest model level at the most sensitive grid point (39.5072N, 112.9197W) in the 6-hour ESA. The y-axis in each scatterplot represents the forecasted  $q_v$  (in kg kg<sup>-1</sup>) in the  $J$ -box surrounding KSLC at 0000 UTC 23 January 2009.

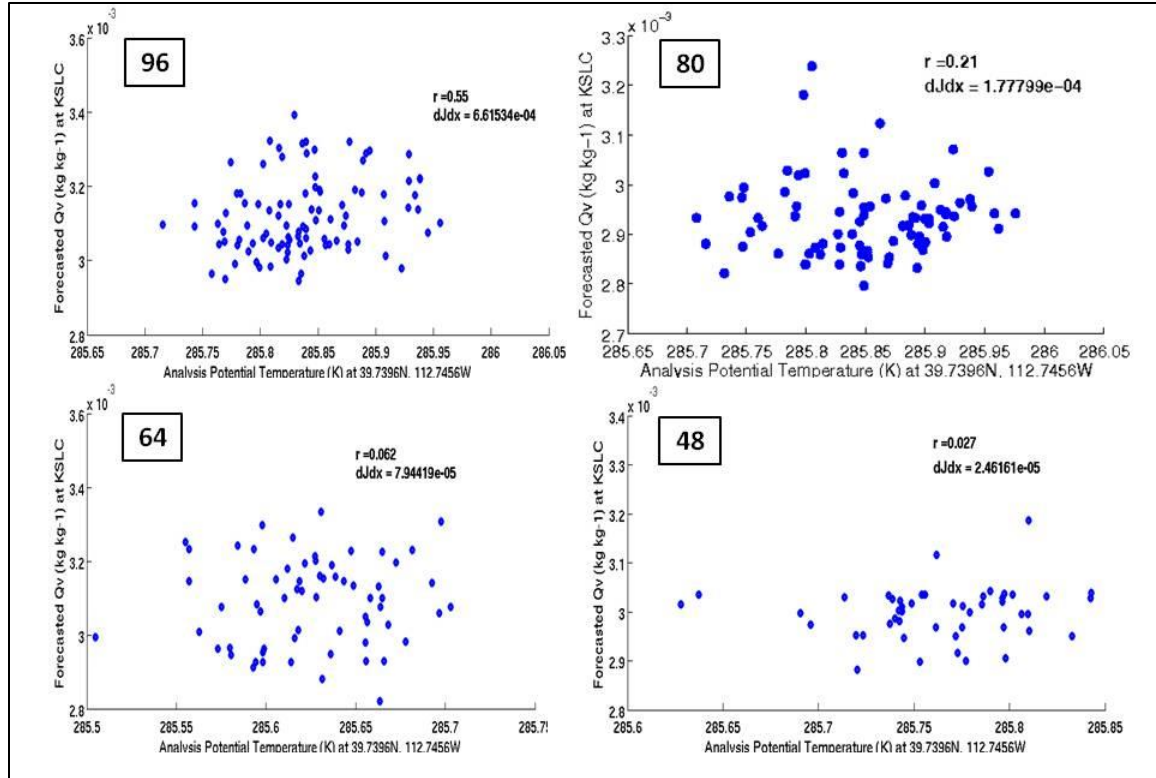


Figure 35. Scatterplots of analysis  $\eta_{-1}$  temperature and forecasted  $q_v$  used in the ESA as ensemble size is reduced from 96 to 48 members. The x-axis represents the 1800 UTC 23 January analysis temperature (in K) at the most sensitive grid point (39.5°N, 112.9°W). The y-axis represents the forecasted  $q_v$  value (in kg kg<sup>-1</sup>) six hours later, valid 0000 UTC 24 January. Also plotted are correlation coefficient ( $r$ ) and sensitivity ( $dJ/dx$ ).

The top left panel in Figure 35 represents the 96-member 6-hour scatterplot which was discussed in section IV.3.B. The top right panel in Figure 35 is the scatterplot for the 80-member ensemble. This panel indicates that the 80-member ensemble has weaker sensitivity than the 96-member ensemble (a

reduction from  $6.6153 \times 10^{-4} \text{ kg kg}^{-1} \text{ K}^{-1}$  to  $1.7780 \times 10^{-4} \text{ kg kg}^{-1} \text{ K}^{-1}$ ). The 80 member ensemble also exhibits less linearity than the 96-member ensemble (a reduction in correlation from  $r = 0.55$  to  $r = 0.22$ ). The bottom two panels in Figure 35 represent the 64 and 48-member ensemble, respectively. Each of these scatterplots shows a significant reduction in sensitivity (an order of magnitude reduction) and very poor linear correlation between  $\theta$  and  $q_v$  ( $r$ -values  $< 0.1$ ). This significant reduction in sensitivity and linearity between 80 and 64 ensemble members appears to define the lower limit of ensemble size that is needed to perform a 6-hour ESA for this case.

Figure 36 provides a depiction of both correlation and sensitivity for the 6-hour ESA for each ensemble member. In addition, the green bars in Figure 36 indicate the upper and lower boundaries of the 95% confidence interval for the correlation coefficient of each member. These boundaries represent the sampling error associated with each ensemble member. Reduction in ensemble size is known to correspond with increasing sampling error.

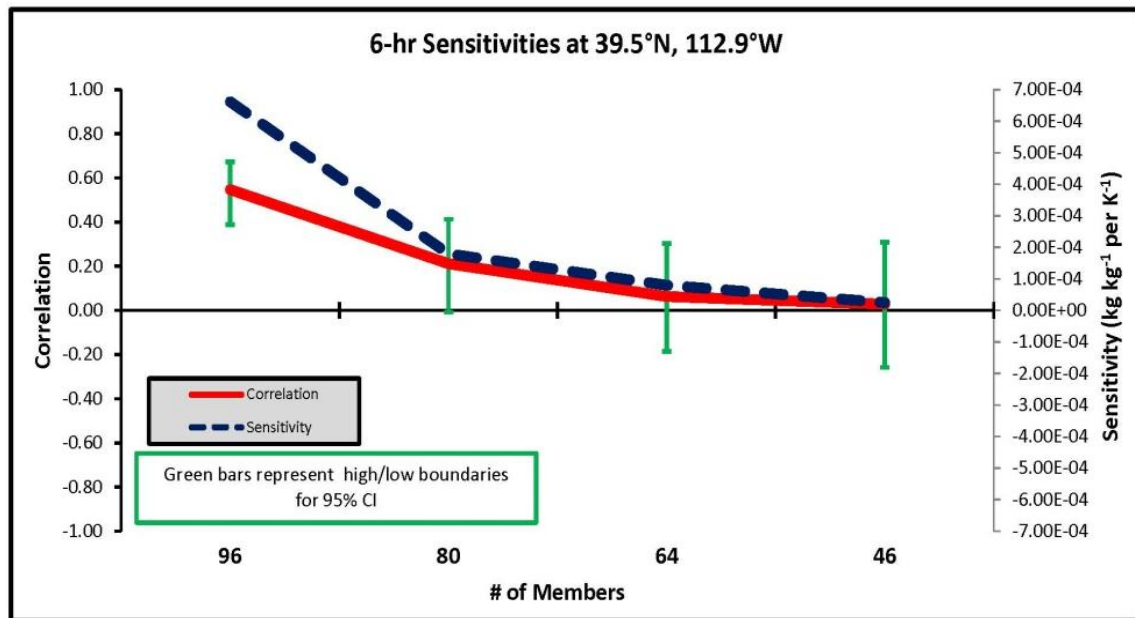


Figure 36. 6-hour ESA chart of correlation in red and sensitivity in blue versus the number of ensemble members for a single point of positive sensitivities at 39.5°N, 112.9°W. Green bars indicate the high and low boundaries of the 95% confidence interval and represent the associated sampling error.

Figure 36 confirms the results shown in Figure 35. As expected, ensembles smaller than 80 members exhibit significant reduction in sensitivity and linearity. In addition, sampling error associated with the r-value of each ensemble member increases, also as expected. Of importance is the error associated with the 80-member ensemble. The green error bars indicate significant variability ( $r = \pm 0.20$ ) in the correlation coefficients associated with this ensemble. This result means there is high variability in the linearity that accompanies the 80 member ensemble and that caution should be taken when implementing an ESA with fewer than 96-members. To achieve the most robust and reliable results for the 6-hour ESA, a 96-member ensemble is preferred.

#### **4. Linearity of the 12-hour Positive Sensitivities**

Previous results presented in section IV.3.B. showed the significant reduction in linearity that occurred when assessing the sensitivity of the 12-hour ESA at the most sensitive 6-hour ESA grid point. Figure 37 contains the scatterplots that accompany ensemble sub-selection of this grid point. Linear associations range from weak and positive ( $r = 0.10$ , 64 members) to lacking linearity ( $r = 0.023$ , 96 members;  $r = 0.025$ , 48 members), to moderate and negative ( $r = -0.3176$ , 80 members). This data further emphasizes the significant variability that accompanies the sensitivity and the linearity between 6 and 12-hour time frames. Though this data point was masked for the 12-hour ESA for failing the 95% CI test ( $P\text{-value} = 0.8218$ ), this variability indicates the limitations of sensitivity data from a single grid point, especially when ESA is performed with less than 96 members.

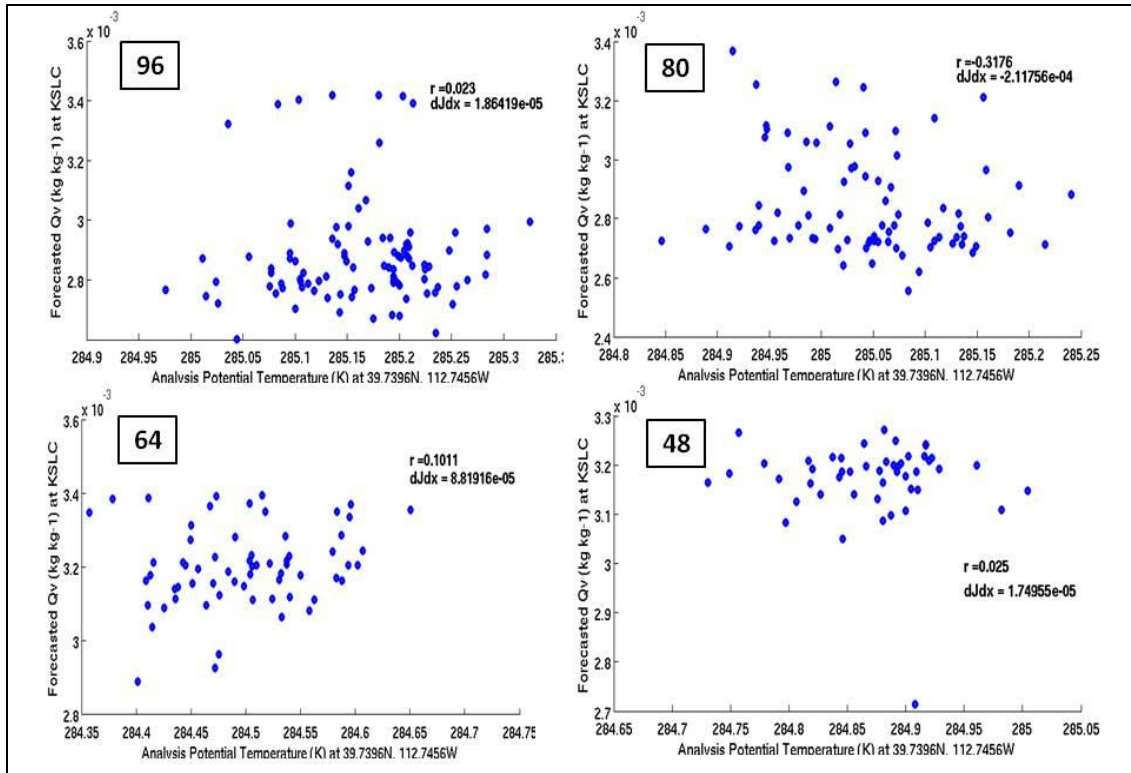


Figure 37. Scatterplots of analysis  $\eta_{-1}$  temperature and forecasted  $q_v$  used in the ESA as ensemble size is reduced from 96 to 48 members. The x-axis represents the 1800 UTC 23 January analysis temperature (in K) at the 12-hour ESA indicated most sensitive grid point (39.5°N, 112.9°W). The y-axis represents the forecasted  $q_v$  value (in kg kg<sup>-1</sup>) 12 hours later, valid 0000 UTC 24 January. Also plotted are correlation coefficient ( $r$ ) and sensitivity ( $dJ/dx$ ).

Also discussed in IV.3.B. was the successful increase in the 12-hour linearity that occurred following a change from the 6-hour ESA most sensitive grid point to the 12-hour ESA most sensitive, and second most sensitive grid points. Figures 38-41 show the accompanying changes in sensitivity and linearity that occur during ensemble sub-selection. Figure 38 provides scatterplots for all ensemble four ensemble systems comparing 1200 UTC 23 January analysis potential temperature at the 12-hour ESA most sensitive grid point and 0000 UTC 24 January  $q_v$  at KSLC. Figure 39 presents the  $r$ -values (with associated sampling error) and sensitivities for this same data set. Figure



40 and Figure 41 provide equivalent graphs for the 12-hour ESA second most sensitive grid point.

These figures indicate that sub-selection of ensembles results in less linearity with decreasing ensemble size, and less overall linearity when compared with equivalent 6-hour ESA sub-systems. R-values for 80-member ensembles fluctuate from lacking linear relationships ( $r = 0.087$ , most sensitive 12-hour ESA grid point) to weakly linear ( $r = 0.253$ , second most sensitive 12-hour ESA grid point). 64 and 48-member ensembles for both top 12-hour sensitivity points lack linear relationships or are weakly negatively linear.

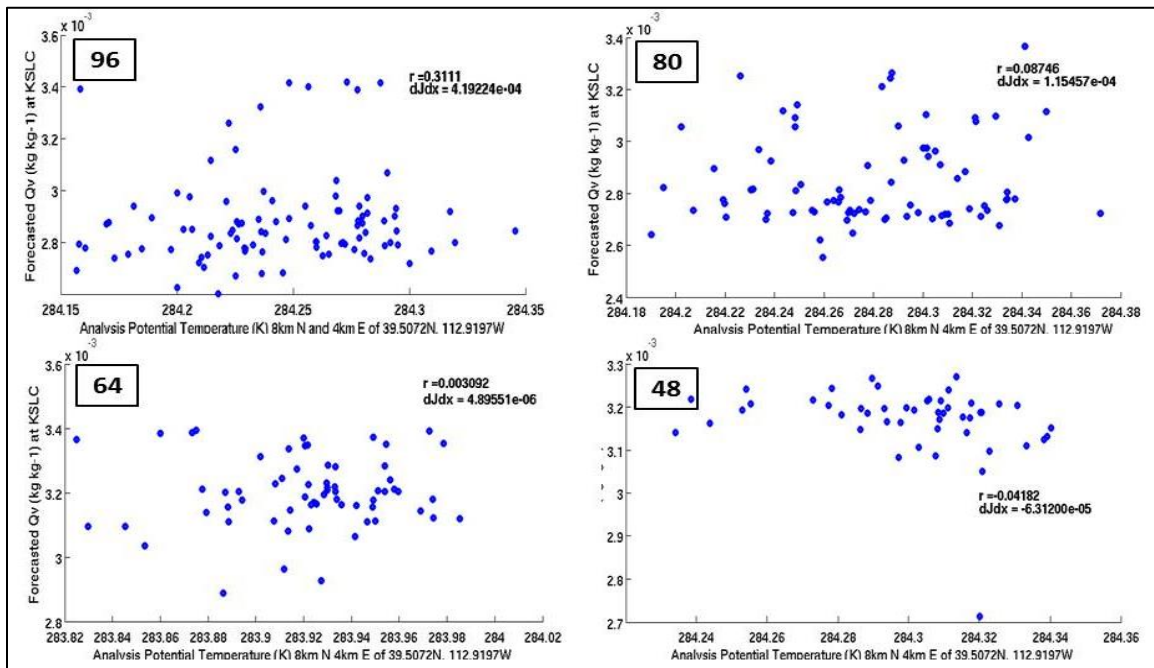


Figure 38. Scatterplots of analysis  $\eta_{-1}$  temperature and forecasted  $q_v$  used in the ESA as ensemble size is reduced from 96 to 48 members. The x-axis represents the 1200 UTC 23 January analysis temperature (in K) at the 12-hour ESA indicated most sensitive grid point (8km N and 4 km E of 39.5°N, 112.9°W). The y-axis represents the forecasted  $q_v$  value (in kg kg<sup>-1</sup>) twelve hours later, valid 0000 UTC 24 January. Also plotted are correlation coefficient ( $r$ ) and sensitivity ( $dJ/dx$ ).



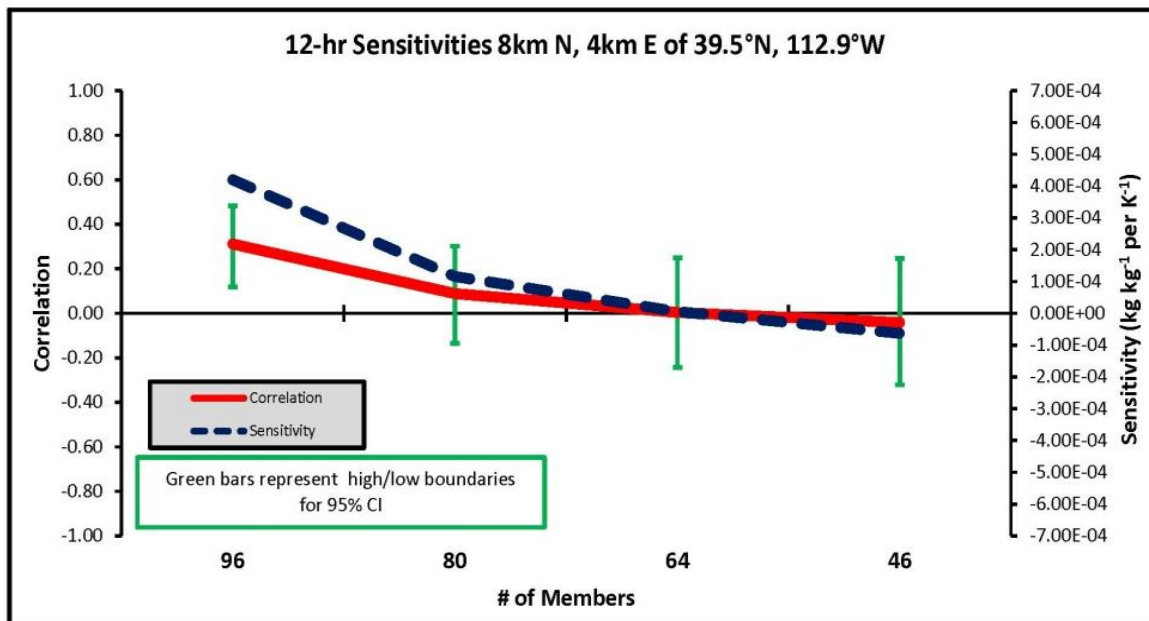


Figure 39. 12-hour ESA chart of correlation in red and sensitivity in blue versus the number of ensemble members for a single point of positive sensitivities at the most sensitive grid point for the 12-hour ESA, 8km N and 4km E of 39.5°N, 112.9°W. Green bars indicate the high and low boundaries of the 95% confidence interval and represent the associated sampling error.

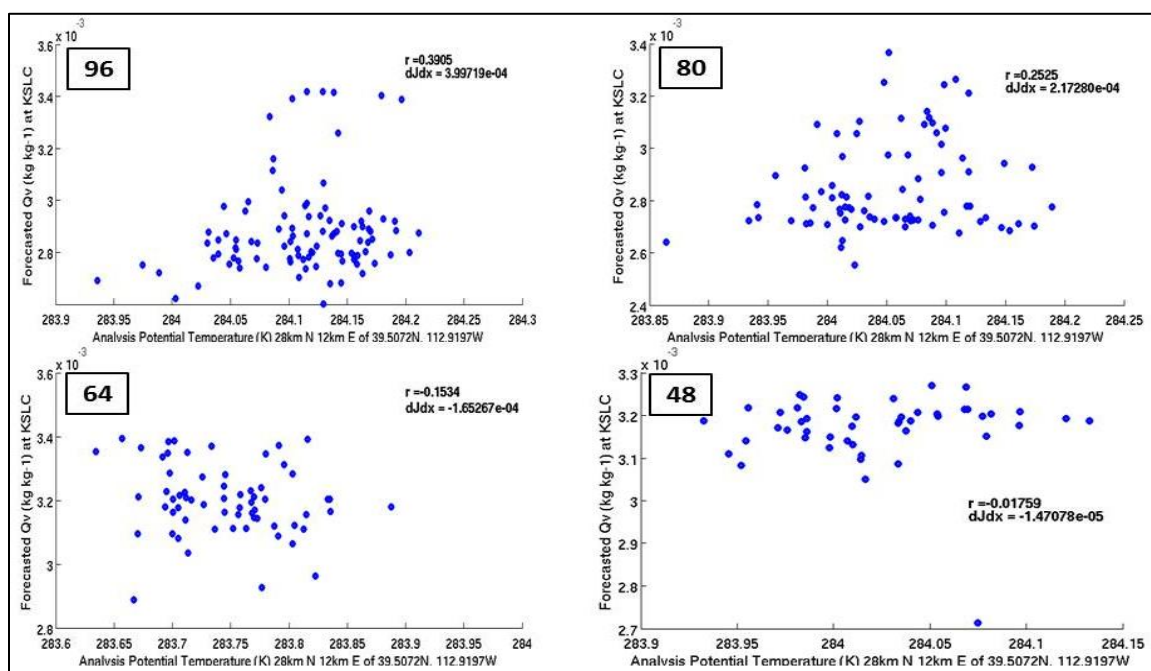


Figure 40. Same as Figure 38, with 12-hour ESA indicated second most sensitive grid point (28km N and 12 km E of 39.5°N, 112.9°W)

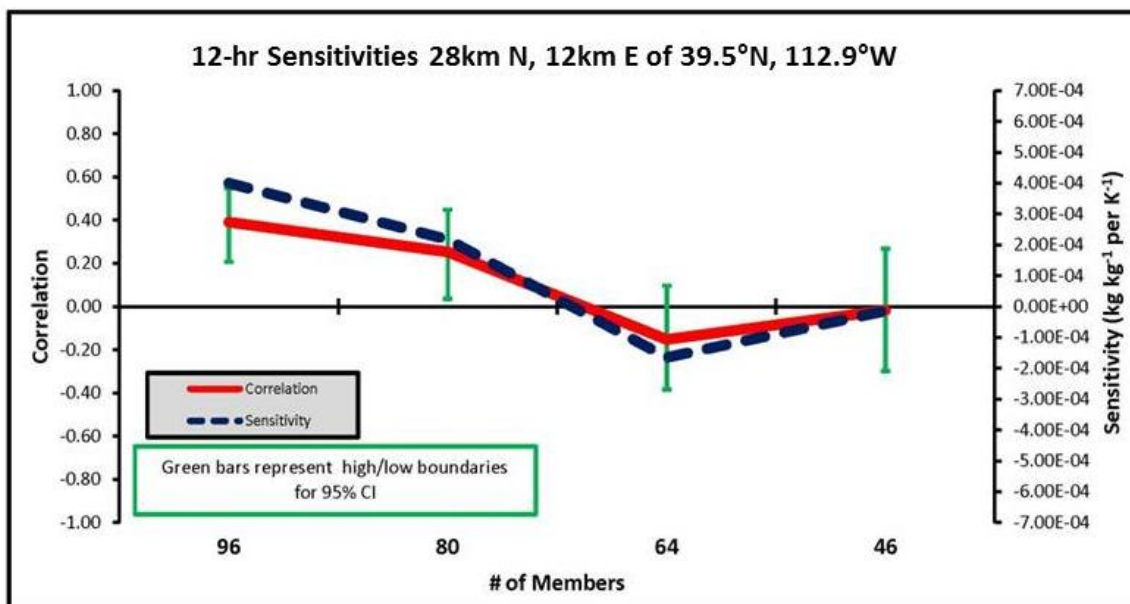


Figure 41. Same as Figure 39, for a grid point 28 km N and 12 km E of 39.5°N, 112.9°W. This grid point is the second most sensitive grid point in the 12-hour ESA.

## 5. Ensemble Size Conclusions

The results of the 6-hour and 12-hour ESA ensemble sub-selection testing indicate the need for a 96-member ensemble in order to produce the most statistically significant and linear sensitivities. The 64-member and 48-member ensembles provided sensitivity results too weak to utilize or with insufficient linearity to prove useful for ESA. The 80-member ensembles exhibited weak linear correlations, but also with weaker overall sensitivity response and with greater error associated with the correlation. The variability exhibited between grid points for 80-member ensembles indicates that correlation derived from an ensemble of this size is subject to significant error variation (12-hour  $r$ -value error =  $\pm 0.21$ -0.22). Though not significantly greater in magnitude than the 96-member ensemble (12-hour  $r$ -value error =  $\pm 0.17$ -0.19), this error becomes more critical with 80-ensemble members due to the low correlation values returned. This variation at low correlation values means that the ESA calculation returned with an 80-member ensemble (12-hour ESA  $r$ -value = 0.09-0.25) may be

moderately linear or may not contain linearity. 96-member ensemble sensitivities by contrast, which show greater linearity (12-hour ESA r-value = 0.31-0.39) and less correlation error, provide a more accurate and reliable sensitivity response. If an 80-member ensemble is to be used to perform ESA, care must be taken to ensure that non-linearities are not an issue.

The significant variation in sensitivity and linearity over 6-hour and 12-hour time frames for the all ensemble systems considered provides further support for the need for a spatially expansive network when considering the placement of additional observational sensors. The single source of failure potential that accompanies the data from a single grid point is evident with these results and underscores the complexity of the statistical and dynamic relationships in this mesoscale complex terrain.

## V. CONCLUSIONS AND FUTURE WORK

This study provided a second investigation of the efficacy of ESA in complex terrain, at high model resolution, and in the mesoscale. The terrain involved the Great Salt Lake Basin, a region of dynamic changes in elevation and hydrologic composition in northern Utah. The high resolution model used in this study was the WRF-ARW, implemented at 4-km grid spacing on the innermost domain of a nested grid. A 96-member ensemble of this model was then created. ESA was performed for a single dense fog event that occurred at Salt Lake City International Airport (KSLC) in the overnight hours of 23-24 January 2009. Our analysis of the ESA indicated a strong and dynamically relevant connection between observed low level temperatures and forecasted fog at the airport.

Sensitivity testing began by performing an ESA using multiple different initial condition parameters at 1800 UTC 23 January and forecast parameters at 0000 UTC 24 January. Initial results indicated that temperature, specifically potential temperature ( $\theta$ ) at the lowest model level ( $\eta_{-1}$ ), provided the clearest and strongest 6-hour sensitivities to forecast fog ( $q_v$ ) at KSLC. Other forecast parameters, including  $q_v$ , total dry air mass in a column, and u- and v- wind components, failed to provide results as robust as  $\theta$ . The ESA temporal scale was then increased to 12 hours to determine the applicability of these results for longer time periods. Using 1200 UTC 23 January  $\theta$  and 0000 UTC 24 January  $q_v$ , it was evident in the 12-hour ESA that  $\theta$  continued to provide a generally spatially consistent, yet weaker sensitivity response than during the initial 6-hour test. Following these tests, it was concluded that  $\theta$  would be the most reliable predictor variable to use in performing this ESA.

To meet the Gaussian distribution requirements inherent in ESA as a system based on linear regression, we then tested our data sets to ensure they were normally distributed. An element of a state vector at a shared single most sensitive grid point ( $x_s$ ) was identified from 6-hour and 12-hour ESA results, and

distribution of  $\eta_{-1}$  initial condition  $\theta(x_i)$  for each 96-member ensemble was analyzed for Gaussianity. A Lilliefors test was implemented to perform Gaussianity testing and results indicated that the 6-hour ESA  $x_i$  ensemble distribution was Gaussian. The 12-hour Lilliefors test indicated that the  $x_i$  ensemble distribution at this same point was non-Gaussian, though several nearby grid points showed valid Gaussianity. It was concluded that positive 6-hour Gaussianity results, combined with positive 12-hour Gaussianity at close-proximity grid points, was sufficient to justify our input parameter distribution as normal. The same test was then performed for the forecast parameter ( $J$ ) at KSLC. Rather than measuring Gaussianity at a single grid point as was done for  $x_i$ , it was necessary to measure  $J$  in a 12-km x 12-km box (4x4 grid spacing) over the lowest two model levels, in order to find a normal distribution of  $J$ . This area-averaged  $J$  provided more robust results by averaging out sampling error and noise.

Once Gaussianity testing confirmed our forecast distributions were Gaussian, we moved forward with conducting the 6 and 12-hour ESA tests under these new conditions. In order to account for statistical sampling error, this data was subjected to a confidence interval test at the 95% level. Sensitivities failing the confidence interval test ( $p \geq 0.05$ ) were removed from the analysis. The results of the 6-hour ESA indicated a response closely related to warm air advection. Strong positive and negative sensitivities to temperature were found at geographic areas likely to see significant influence of warm air advection. It was believed this suggested a relation to strengthening of a low level inversion which induced fog at KSLC at a later time. Results of the 12-hour ESA showed an overall weaker sensitivity response, but one still influenced by warm air advection. These results showed additional influence from the mid-level disturbance that passed through northern Utah on 23 January. This disturbance noticeably alters the distribution of sensitivities, though the dynamic signal of both forcing mechanisms, warm air advection and mid-level disturbance, can be distinguished. The non-linearities in  $u$ - and  $v$ - component wind introduced by the mid-level disturbance had prompted Chilcoat (2012) to move the focus of his

study 6 hours later, to avoid complication. This study did not make such changes, as  $\theta$  provided a sufficiently robust result.

Examination of the linearity of the data sets revealed that 6-hour correlation between  $x_i$  and  $J$  existed at a moderate level ( $r = 0.55$ ). The 12-hour ESA indicated that the linearity broke down when the 6-hour ESA  $x_s$  was used, but could be restored to weak or moderate linearity ( $r = 0.33 - 0.39$ ) by moving  $x_s$  to 12-hour ESA most sensitive grid points. This finding shows that under influence of complex mesoscale forcing over varying temporal scales, sensitivity locations exhibit dynamic spatial variation. This implies that a future observing network must include a mobile observing platform, or be distributed with sufficient density at known sensitivity regions as to adequately observe changes in initial conditions known to relate to changes in forecast model output.

Tests were then conducted to determine whether the addition of an observation  $y_o$  could accurately predict a change in  $J$  at a later time. Tests were performed with a  $+1\sigma$  perturbation, to simulate an observation, and with a “truth” perturbation to represent the effects of assimilating an observation. ESA also allows for sensitivity testing using ensemble statistics and “truth” data to create “expected” forecast changes, done without actually introducing a perturbation. Comparison of “truth” sensitivity testing indicates the introduction of a  $\theta$  observation at  $\eta_{-1}$  for  $x_s$  will accurately predict change in  $q_v$  6-hours later at KSLC. This result is significant in that it shows potential for ESA to be used to place an observation(s) which can then improve forecasts for parameters of specific interests.

The final assessment performed was to analyze how ensemble subsampling affected sampling error, the results of which could identify the minimum size ensemble needed to perform ESA. Both 6 and 12-hour ESA subsampling was conducted and both indicated a strong preference for an ensemble of 96-members for best results. While 80-member ensembles could potentially be used to achieve similar results, the weakness of the sensitivity and the amount of increased error associated with the correlations are significant shortcomings for an ensemble of this size.

## A. COMPARISON TO CHILCOAT (2012) RESULTS

Qualitative comparison between this study and Chilcoat (2012) indicates a general agreement in the evolution of the dense fog event at KSLC. Both studies showed similar forecasting accuracy for the density of  $q_v$  at KSLC and both indicated a tendency to begin and end the dense fog event 3-6 hours prematurely. Differences in conclusions between the two studies primarily arise because of the difference in ESA forecast time frames. Because of the time shift to a later hour, Chilcoat's  $u$ - and  $v$ -wind ESA results and resulting conceptual model identify the locations and dynamic features most responsible for advecting the fog into KSLC. This study, in contrast, identified the initial conditions most responsible for the atmospheric profile that made the creation of the dense fog event possible. Together, these studies provide a thorough conceptual understanding of the variables and forces which lead to the initiation and consequent advection of the dense fog over KSLC.

Direct quantitative comparison between these studies is more difficult for several reasons. The first is due to the difference in the  $J$ -box used in each study. Chilcoat used an 8-km x 8-km grid box summed over the first two  $\eta$ -levels. In order to meet Gaussianity requirements, this study implemented a 12-km x 12-km  $J$ -box summed over the first two  $\eta$ -levels. The larger  $J$ -box used in this study means the response variable includes contributions from 32 horizontal and vertical model grid points, rather than the 18 used by Chilcoat. This increase in  $J$ -box size naturally means the quantified sensitivity response in this study will have greater magnitude.

The second reason comparison is difficult is the change in DA procedures that was undertaken between studies. Assimilation of observations in this study was completed through ingest of observed "truth" rawinsonde soundings at the same time interval and at the same grid spacing as naturally occurred. Chilcoat's DA process assimilated "truth" rawinsonde observations in columns meant to mimic a sparse data network, contributing 100 rawinsonde ascents every three hours. Chilcoat's observations were randomly located throughout the domain,

but fixed in time. This variation inevitably caused changes in model analyses that would have resulted in altered forecasts and thus altered ESA results. The specific difference between the two systems was not examined in this study, though its existence further complicates comparison between the two studies.

In addition to the reasons noted above, Chilcoat's ESA was performed over a different time frame. Due to non-linearities in results encountered over his original 12-hour ESA using 1200 UTC 23 January analysis and 0000 UTC 24 January forecast, Chilcoat shifted his 12-hour ESA 6-hours later in time. The ESA results presented by Chilcoat involved 1800 UTC 23 January analysis and 0600 UTC 24 January forecast. This time frame shift allowed for the avoidance of the non-linearities introduced in the  $u$ - and  $v$ - wind components by the mid-level disturbance. This in turn allowed for more linear sensitivity responses than those presented in this study.

## **B. POTENTIAL NETWORK DESIGN**

The ESA conducted for this thesis identified several regions of sensitivity importance. These locations, identified in Figure 42, represent locations of maximum sensitivity or locations that exhibit dynamic sensitivity over the 12-hour time frame leading up to the dense fog event. It is believed that additional observations placed in these locations would provide improved accuracy in the prediction of dense fog events at KSLC. Region 1 in Figure 42 represents the region of strongest sensitivity and sensors placed here would be critical to observing any warm air advection being channeled northward through the Central Utah Desert Range. Region 2 in Figure 42 annotates a dynamic area where southerly warm air advection meets the influence of the GSL cold dome. Additional observations placed in this region, the southeast Salt Lake Valley, or along the Traverse Mountains to the south would help to define the warm air advection as well as the PBL profile in the southeast GSL Basin, critical for forecasting dense fog at KSLC. Region 3 in Figure 42 represents a low lying area northeast of the GSL which exhibits strong sensitivity when significant



warm-air advection is present across the GSL basin. Though a single observation exists on the northeast boundary of this region at Brigham City Airport (ICAO: KBMC), additional observations across this plain would allow more thorough observation of warm air channeling between the Wasatch Range and a cold dome over the GSL. Combined, observations at these areas would help to characterize the PBL conditions in the GSL known to lead to dense fog events at KSLC.

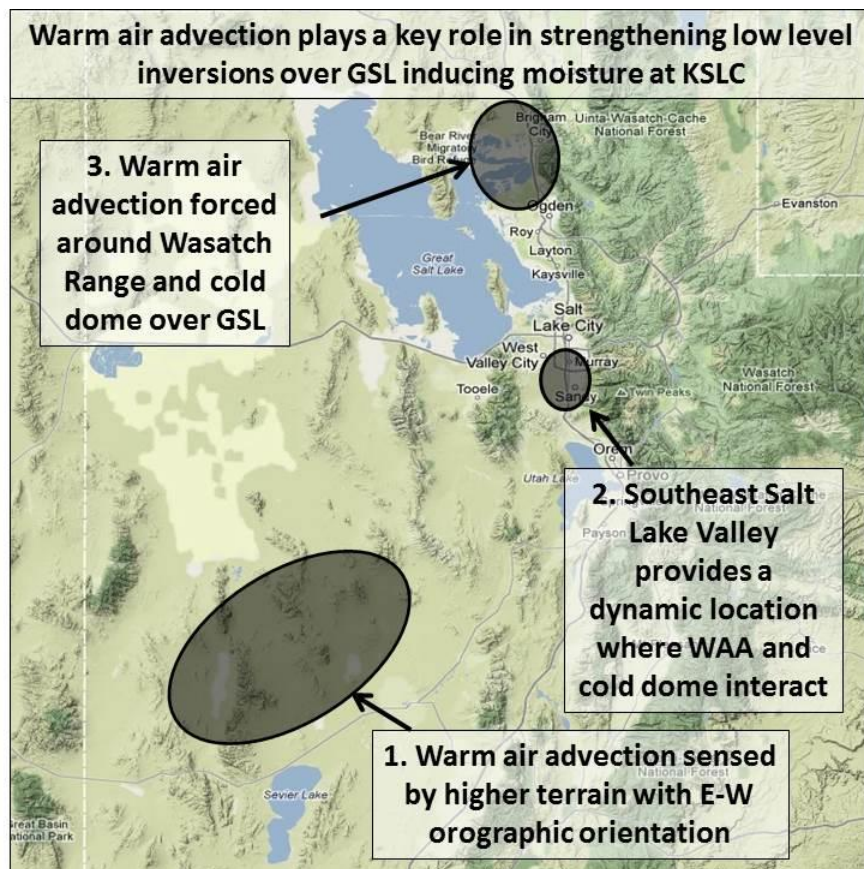


Figure 42. Locations of strong and/or reliable temperature sensitivity regions that are considered important in forecasting  $q_v$  at Salt Lake City International Airport (After Google Maps).

Chilcoat (2012) used  $u$ - and  $v$ - wind components to identify two regions of sensitivity he believed were most influential to forecasting fog at KSLC (Figure 43). As discussed, Chilcoat's results represent conclusions from an ESA focused 6 hours later than this study. Because of this disparity his results likely

represent locations where dense fog advection forcing mechanisms are observed, and not locations where PBL conditions leading to dense fog creation are focused.

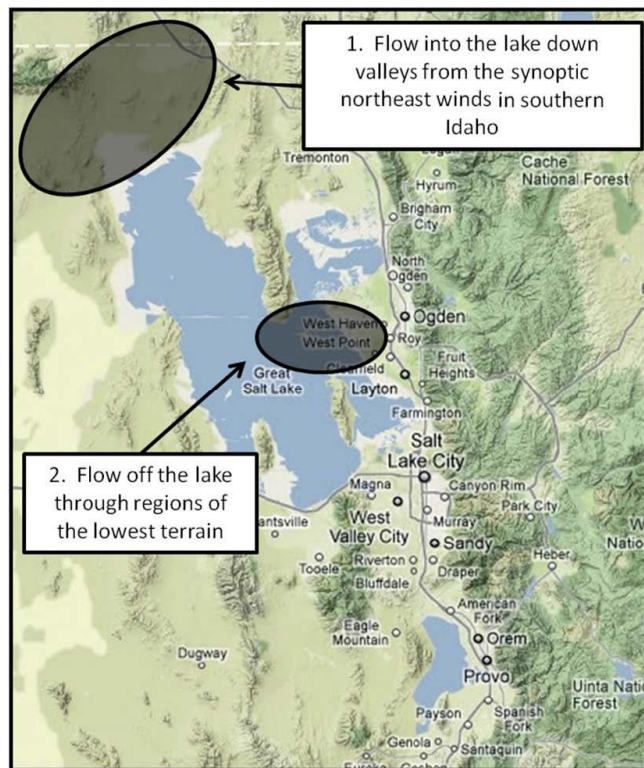


Figure 43. Chilcoat's map of locations of the strong sensitivities that are considered important in forecasting the amount of moisture received at the SLC International Airport. (From Chilcoat 2012)

Validation and confirmation of these potential network observation placement regions would be a primary focus of future work involving other dense fog events. We believe temperature as ESA initial condition provides a more resilient response to non-linear influence over longer time scales, though  $u$ - and  $v$ -component wind-based ESA should also provide a response helpful for complete understanding of dense fog event evolution.

### **C. APPLICABILITY TO U.S. MILITARY**

As technology continues to move forward providing greater diversity and deployability in weather sensor technology, it is important that attention be paid to sensor placement which maximizes impact to forecaster and operator. While garrison fixed-base observing equipment will always be a requirement, the potential benefit of the introduction of additional sensors outside the base proper holds great promise. ESA provides a means by which the impact of additional observations can be determined a priori, at merely the cost in time and resources to conduct the study. As budgetary constraints will always limit the amount and type of observing capability available to weather personnel, this system provides a means of intelligently placing the limited resources that are made available. The difficulty may arise when an ESA-determined sensor placement location is identified that provides critical input to an NWP system, while adding limited additional information to the forecaster on the ground. The decision on where and when to place a sensor must be weighed between the potential enhancement of situational awareness provided by placing a sensor(s) in a known data void region, versus the potential gain in forecast accuracy achieved through placement of a sensor(s) that primarily benefits the NWP system. While NWP will never provide a sole source of informing forecasters in providing decision-quality information, improving the data that it does provide should be a primary concern to the Air Force weather community.

The computing resources necessary to perform this ensemble analysis are significant and prohibit the implementation of ESA for data-thinning during data assimilation or real-time updates to forecast metrics. The ensemble computations completed at ERDC took several days to complete and multiple delays and issues were encountered. As computing efficiency increases and ensemble systems become more capable over time, operational use of ESA for these functions may prove possible. Implementation of ESA at this time is limited to preconceived sensitivity studies as of the type examined in this study.

## D. FUTURE WORK

This study showed the efficacy of using temperature as a predictor variable when  $q_v$  is the associated predictand forecast variable. These results are unique to this mesoscale environment and model grid scale. Several ideas are presented below which identify means of further validating the conclusions presented in this paper with the goal of expanding the implications of this research to future and operational environments.

1. Expand the research to include results for multiple dense fog events at KSLC and across the GSL. More definitive conclusions regarding the use of ESA to design future observational networks can be achieved through examination of more than one dense fog event. Specific consideration should be given to events that meet known climatological norms for dense fog events. It was discovered during this study that temperature at KSLC was  $> 0^{\circ}\text{C}$  during the dense fog event of 23-24 January. This anomaly occurs in  $< 6\%$  of all known dense fog events at KSLC over the past 30 years. The selection of dense fog events that fall within climatological norms will help to ensure the results are representative of typical mesoscale forcing in and around GSL. Study of other dense fog events should focus on initial condition PBL temperature and  $u$  and  $v$ -wind parameters, while also examining the potential sensitivity response from initial condition  $q_v$  and  $\mu$ .

2. Evaluate the impact of multiple additional observations at the locations identified as the most sensitive grid points. This study examined the model analysis and forecast change attributable to the addition of a single additional observation. By theoretically adding multiple sensors and determining individual and collective grouping response, we can determine a more complete understanding of what an observational network design should resemble. This evaluation can be done through assimilating observations at proposed sites following ESA testing procedures for “truth” observations outlined in section IV.C.2. of this paper. Following DA, the analysis difference created ( $\delta x$ ) is multiplied times the calculated sensitivity ( $dJ/dx$ ) at that point to provide an

expected forecast change in  $q_v$ . It is not necessary to rerun the ensemble to create a new expected forecast. This process is then repeated at multiple sites to test the design of a potential observational network.

3. Place observing sensors in the identified sensitivity locations for a full winter season. Perform data denial experiments to confirm theoretical findings identified in this study. This study utilized synthetic perfect (no error) observations to test the results of the ESA. Assimilation of real-world observations introduces additional observation error which may affect sensitivity testing outcomes. A field test of these sensitivity findings could help confirm or deny the results found in this study.

4. Examine the impact of alternate observing platforms at the most sensitive grid point. This study examined how temperature measured at near-surface level at points around the GSL contributed to formation of fog at KSLC at a later time. The conclusion from this study is that several fixed sensors or a single mobile sensor would need to be implemented to realize the forecast accuracy improvement suggested by this ESA. However, it is unknown exactly what platform could provide the data necessary to achieve these results. Does a fixed sensor that provides only surface observations provide enough data to sufficiently inform the model to improve the forecast? If the fixed observation is tower-mounted, what level must it reach to gather necessary data? Alternately, could the same or better results be obtained through the use of a UAS or aerostat-like system? These systems could be deployed temporarily based upon known synoptic or mesoscale precursors that suggest development of certain forecast conditions is likely.

5. Investigate other potential dense fog parameters for  $J$  to ensure PBL moisture budget is being properly accounted for and to maximize the accuracy of the fog forecast. A notable difference ( $\sim 1.0 \times 10^{-4} \text{ kg kg}^{-1} - 1.5 \text{ kg kg}^{-1}$ ) was found between observed  $q_v$  at KSLC and the ensemble mean forecast value at between 1800 UTC 23 January and 0600 UTC 24 January. This discrepancy represents  $\sim 25\%$  difference between forecast and observed  $q_v$  and may represent the cause for the differential between actual and observed values

obtained during ESA testing. Accurate representation of the PBL energy and moisture budget is important to understanding the creation and dissolution of dense fog in the GSL.

## LIST OF REFERENCES

- Adams, T. C., International Association of Hydrological Sciences, cited 2013: Temperature of Great Salt Lake in Utah and Comparative Data. [Available online at [http://iahs.info/redbooks/a025/Limno\\_Q1\\_R2.pdf](http://iahs.info/redbooks/a025/Limno_Q1_R2.pdf).]
- Alder W. J., L. S. Nierenberg, S. T. Buchanan, W. Cope, J. A. Cisco, C. C. Schmidt, A. R. Smith, and W. E. Figgins, 1998: Climate of Salt Lake City, Utah. NOAA Tech. Memo. NRS WR-152, 89 pp.
- Ancell, B. and G.J. Hakim, 2007: Comparing adjoint- and ensemble-sensitivity analysis with applications to observation targeting. *Mon. Wea. Rev.*, **135**, 4117–4134.
- Anderson, J. L., 2001: An ensemble adjustment Kalman filter for data assimilation. *Mon. Wea. Rev.*, **129**, 2884–2903.
- Anderson, J., T. Hoar, K. Raeder, H. Liu, N. Collins, R. Torn, and A. Avellano, 2009: The data assimilation research testbed. *BAMS*, **Sep**, 1283–1296.
- Berliner, L. M., Z. Q. Lu, and C. Snyder, 1999: Statistical design for adaptive weather observations. *J. Atmos. Sci.*, **56**, 2536–2552.
- Burgers, G., van Leeuwen, P.J. and Evensen, G. 1998: Analysis scheme in the ensemble Kalman filter. *Mon. Weather Rev.*, **126**, 1719–1724.
- Chilcoat, K.H., 2012: The Potential Observation Network Design with Mesoscale Ensemble Sensitivities in Complex Terrain. M.S. thesis, Dept. of Meteorology, Naval Postgraduate School, 83 pp.
- Dudhia, J., 1989: Numerical study of convection observed during the winter monsoon experiment using a mesoscale two-dimensional model. *J. Atmos. Sci.*, **46**, 3077–3107.
- Ek, M. B., K. E. Mitchell, Y. Lin, E. Rodgers, P. Grunmann, V. Koren, G. Gayno, and J.D. Tarpley, 2003: Implementation of Noah land surface model advances in the National Centers for Environmental Prediction operational mesoscale H Model. *J. Geophys. Res.*, **108**, 8851–8867.
- Errico, R. M., 1997: What is an adjoint model? *Amer. Meteor. Soc.*, **78**, 2577–2591.
- Evensen, G., 1994: Sequential data assimilation with a nonlinear quasi-geostrophic model using Monte Carlo methods to forecast error statistics. *J. Geophys. Res.*, **99**, 10143–10162.

- Gombos, D., and J. A. Hansen, 2008: Potential vorticity regression and its relationship to dynamical piecewise inversion. *Mon. Wea. Rev.*, **136**, 2668–2682.
- Grande, W. E., U.S. Air Force, cited 2013: Braving the weather. [Available online at <http://www.afweather.af.mil/news/photos/mediagallery.asp?page=5>.]
- Hakim, G. J., and R. D. Torn, 2008: Ensemble synoptic analysis. *Synoptic–Dynamic Meteorology and Weather Analysis and Forecasting: A Tribute to Fred Sanders, Meteor. Monogr.*, **55**, Amer. Meteor. Soc., 147–162.
- Hamill, T. M., cited 2013: Review of “Covariance Localization” in Ensemble Filters. [Available online at [www.esrl.noaa.gov/psd/people/.../CovLocal\\_BuenosAires\\_Hamill.ppt](http://www.esrl.noaa.gov/psd/people/.../CovLocal_BuenosAires_Hamill.ppt).]
- Hamill, T. M., and C. Snyder, 2002: Using improved background-error covariances from an ensemble Kalman filter for adaptive observations. *Mon. Wea. Rev.*, **130**, 1552–1572.
- Hill, G. E., 1987: Fog Effect of the Great Salt Lake. *J. Appl. Meteor.*, **27**, 778–783.
- Hogan, D., cited 2013: Salt Lake Valley dense fog initiation study. [Available online at <http://www.wrh.noaa.gov/slc/projects/fogstud/fogstudy.htm>.]
- Hong, S.-Y., Y. Noh, and J. Dudhia, 2006: A new vertical diffusion package with an explicit treatment of entrainment processes. *Mon. Wea. Rev.*, **134**, 2318–2341.
- Kain, J. S., 2004: The Kain–Fritsch Convective Parameterization: an update. *J. Appl. Meteor.*, **43**, 170–181.
- Kalnay, E., 2003: *Atmospheric Modeling, Data Assimilation and Predictability*. 3rd ed. Cambridge University Press, 341 pp.
- Langland, R. H., 2005: Issues in targeted observing. *Quart. J. Roy. Meteor. Soc.*, **131**, 3409–3425.
- Lewis, J. and S. Lakshmivarahan, 2008: Sasaki’s pivotal contribution: Calculus of variations applied to weather map analysis. *Mon. Wea. Rev.*, **136**, 3553–3567.
- Lorenz, E. N., 1963: Deterministic nonperiodic flow. *J. Atmos. Sci.*, **20**, 130–141.
- MATLAB. 2012: version 7.14.0.739 (R2012a). The MathWorks Inc. [Available online at <http://www.mathworks.com/help/techdoc/>.]



- Mlawer, E. J., S. J. Taubman, P. D. Brown, and M. J. Iacono, 1997: Radiative transfer for inhomogeneous atmospheres: RRTM, a validated correlated-k Model for the longwave. *J. Geophys. Res.*, **102**, 16663-16682.
- Saltelli, A., S. Tarantola, F. Campolongo, and M. Ratto, 2004: *Sensitivity Analysis in Practice: A Guide to Assessing Scientific Models*. John Wiley and Sons, 232 pp.
- Skamarock, W.C., J. B. Klemp, J. Dudhia, D. O. Gill, D. M. Barker, M. G. Duda, X. Huang, W. Wang, and J. G. Powers, 2008: A description of the advanced research WRF version 3. NCAR Tech. Note, NCAR/TN-475+STR, 113 pp.
- Slemmer, J., 2004: Study of dense fog at the Salt Lake City International Airport and its impacts to aviation. Western Region Tech. Attachment, 04–01. [Available online at <http://www.wrh.noaa.gov/wrh/04TAs/0401/SLCFog.htm>.]
- Torn, R. D., 2010: Ensemble-based sensitivity analysis applied to African easterly waves. *Wea. Forecasting*, **25**, 61–78.
- Torn, R. D., G. J. Hakim and C. Snyder, 2006: Boundary conditions for limited-area ensemble Kalman filters. *Mon. Wea. Rev.*, **134**, 2490–2502.
- Torn, R. D., and G. J. Hakim, 2008: Ensemble-based sensitivity analysis. *Mon. Wea. Rev.*, **136**, 663-677.
- Torn, R. D., and G. J. Hakim, 2009: Initial condition sensitivity of Western-Pacific extratropical transitions determined using ensemble-based sensitivity analysis. *Mon. Wea. Rev.*, **137**, 3388-3406.
- The Weather Research and Forecasting Model (WRF), cited 2012: WRF Model Users Page. [Available online at <http://wrf-model.org/users/users.php>.]
- Wilks, D. S., 2006: *Statistical methods in the atmospheric sciences*. 2nd ed. Academic Press, 627 pp.
- Wolyn, P. G., and T. B. McKee, 1989: Deep Stable Layers in the Intermountain Western United States. *Mon. Wea. Rev.*, **117**, 461–472

THIS PAGE INTENTIONALLY LEFT BLANK

## INITIAL DISTRIBUTION LIST

1. Defense Technical Information Center  
Ft. Belvoir, Virginia
2. Dudley Knox Library  
Naval Postgraduate School  
Monterey, California
3. Air Force Weather Technical Library (AFWTL)  
14th Weather Squadron  
Asheville, North Carolina